Novel Radiation Sensors Based On Bio/Nanomaterials

by

Morteza Ahmadi

A thesis
presented to the University of Waterloo
in fulfillment of the
thesis requirement for the degree of
Doctor of Philosophy
in
Systems Design Engineering

Waterloo, Ontario, Canada, 2013

AUTHOR'S DECLARATION

I hereby declare that I am the sole author of this thesis. This is a true copy of the thesis, including any required final revisions, as accepted by my examiners.

I understand that my thesis may be made electronically available to the public.

Abstract

X-ray sensors are essential to many applications which are not limited to diagnostics and imaging technologies. Such sensors are extensively used in industry, medicine, research and space technology for applications such as safety, security, quality control, imaging and treatment. Depending on the effect of the radiation on the matter employed in the sensor, different types of X-ray sensors are fabricated. However, available techniques of X-ray detection have been under development due to specific shortcomings such as finite life time, low sensitivity, and post-processing requirements. This thesis is focused on design, fabrication and characterization of novel radiation sensors based on bio/nanomaterials.

Bacteriorhodopsin (BR), a proton pump protein in the cell membrane of *Halobacterium Salinarum*, has been used to fabricate a sensor to measure dose and dose rate of X-ray beam in the kilovoltage and megavoltage energy range. The mass attenuation coefficients, effective atomic numbers and electron densities of BR and its comprising amino acids have been calculated for 1 keV-100 GeV photons to better understand the interaction of BR with X-ray photons.

A theoretical formulation for calculating the change in the conductivity of nanoparticles under radiation is also provided. In particular, the dependence of radiation induced conductivity to irradiated particle size is given. In addition to that, an X-ray sensor based on thin film of bismuth sulfide has been fabricated using laser micromachining and chemical deposition techniques. This sensor has been characterized under a diagnostic X-ray machine with kilovoltage energy beam.

Acknowledgements

I would like to express my deepest gratitude to my PhD advisors Professor John Yeow and Professor Ernest Osei. This work would have been impossible without their generous support and guidance.

I am also thankful to my committee members Professor Maud Gorbet, Professor Frank Gu and Professor Zoya Leonenko for valuable discussions and suggestions during my PhD.

I would like to thank Professor George Knopf for accepting to be the external examiner and Professor Marc Aucoin for accepting to be the delegate for Professor Gu.

I am thankful to Vicky Lawrence and administrative staff of Department of Systems Design Engineering for their assistance during my PhD.

I acknowledge financial support from Natural Sciences and Engineering Research Council (NSERC), Kidney Research Scientist Core Education and National Training Program (KRESCENT), Waterloo Institute for Nanotechnology, University of Waterloo President's Graduate Scholarship, and University of Waterloo Graduate Scholarship.

I would like to thank my friends in Advanced Micro/Nano Devices Lab who have made the graduate life enjoyable: Mehdi Shahini, Mohsen Shahini, Albert Chen, Lawrence Wong and many others.

And finally, thank you Elham for your support, kindness and love!

Dedication

This thesis is dedicated to “Ehsan” who was fighting Hodgkin’s Lymphoma for 26 months, and who has been an inspiration to me. You will be fondly remembered and greatly missed.

Table of Contents

AUTHOR'S DECLARATION ii

Abstract iii

Acknowledgements iv

Dedication v

Table of Contents vi

List of Figures x

List of Tables xiii

Chapter 1 Introduction 1

- 1.1 General background: 1
- 1.2 Units of measurement in radiation sensing: 1
    - 1.2.1 Unit of measuring radiation energy 1
    - 1.2.2 Units of measuring radiation dose 2
    - 1.2.3 Unit of measuring equivalent dose and effective dose 2
    - 1.2.4 Unit of measuring radiation exposure 3
    - 1.2.5 Unit of measuring the machine output 3
- 1.3 X-ray generation mechanisms 3
    - 1.3.1 Bremsstrahlung (braking radiation) 4
    - 1.3.2 Characteristic emission 5
- 1.4 Interaction of X-ray photons with matter 6
    - 1.4.1 Coherent scattering 7
    - 1.4.2 Photoelectric effect 8
    - 1.4.3 Compton scattering 9
    - 1.4.4 Pair production 10
- 1.5 Radiation measurement devices for medical applications 10
    - 1.5.1 Ionization Chamber 10
    - 1.5.2 Thermoluminescence dosimeter 12
    - 1.5.3 Radiochromic film 12
    - 1.5.4 MOSFET dosimeters 13
- 1.6 Research objectives 14
- 1.7 Thesis scope 15

Chapter 2 17
Bacteriorhodopsin 17
  2.1 Synthesis of PM 18
  2.2 Properties of PM and BR 18
  2.3 Methods of coating surfaces with BR for device fabrication 19
    2.3.1 Layer by layer electrostatic deposition (LBL-ESD) 19
    2.3.2 Langmuir-Blodgett (LB) 19
    2.3.3 Electrophoretic sedimentation (EPS) 20
  2.4 Photocycle of BR 21
  2.5 Electron transport in BR 22
  2.6 Applications of BR 23
    2.6.1 Optical data storage 23
    2.6.2 Solar cell 24
    2.6.3 Image detector 24
  2.7 Fabrication of BR sensor 26
Chapter 3 Interaction of X-ray photons with bacteriorhodopsin 29
  3.1 Mass attenuation coefficient, effective atomic number and effective electron density 29
  3.2 Method of Computation 30
  3.3 Results and Discussion 33
    3.3.1 Mass attenuation coefficients 33
    3.3.2 Effective atomic number 35
    3.3.3 Effective electron density 37
  3.4 Radiation oncology applications 37
  3.5 Discussion 42
Chapter 4 Use of bacteriorhodopsin as an X-ray sensor 43
  4.1 Megavoltage (MeV) X-rays beam energy range 43
    4.1.1 Linear accelerator 43
    4.1.2 Measurement set up for experiments with LINAC 43
    4.1.3 Variation with dose rate and beam energy 44
    4.1.4 Variation with field size 48
    4.1.5 Variation with absorbed dose 50

4.1.6 Repeatability test 50
4.1.7 Sensing mechanism 51
4.1.8 Discussion 52
4.2 Kilovoltage (keV) X-rays beam energy range 55
4.2.1 Superficial X-ray machine 55
4.2.2 Measurement set up for experiments with superficial X-ray machine 57
4.2.3 Results 58
4.2.4 Discussion 64
Chapter 5 An X-ray sensor for diagnostic radiology based on thin film of bismuth sulfide 66
5.1 Materials and Methods 67
5.1.1 Bismuth sulfide 67
5.1.2 Diagnostic X-ray imaging machine 72
5.1.3 Measurement set up for experiments with diagnostic X-ray machine 74
5.2 Results 74
5.3 Discussion 82
Chapter 6 Radiation sensors based on nanomaterials 85
6.1 Conductivity 85
6.2 Radiation induced conductivity (RIC) 86
6.3 RIC for radiation sensing 88
6.4 Dependence of band gap on particle size 89
6.5 Radiation induced conductivity in nanomaterials 89
6.6 Carbon nanotube radiation sensor 90
6.6.1 Fabrication 90
6.6.2 Set up 90
6.6.3 Results 91
6.7 Zinc oxide nanoparticle radiation sensor 93
6.7.1 Results 94
6.8 Discussion 94
Chapter 7 Conclusion 96
7.1 Conclusions and contributions 96
7.2 Recommendation for future studies 98

Appendix A 100
Appendix B Calculated data for bacteriorhodopsin and its comprising amino acids 101
Bibliography ……………………………………..…………………………………………… 110

List of Figures

Figure 1.1: Bremsstrahlung (braking radiation) 4
Figure 1.2: electron transitions in lower energy levels of atoms and generated characteristic X-ray photons 5
Figure 1.3 Measured X-ray spectrum of Cu. The characteristic Cu K_α and Cu K_β radiation peaks in the photon energy range from 7.5 to 9.5 keV are shown in B [2]. 6
Figure 1.4: coherent scattering 7
Figure 1.5: photoelectric effect 8
Figure 1.6: Compton scattering 9
Figure 1.7: pair production 10
Figure 2.1: EPS method of coating BR on conductive substrates [39]. 20
Figure 2.2: Photocycle of BR [40]. K, L, M, N, O are the intermediate states of the photocycle of BR. bR is the initial state. The absorption peaks for intermediate states are shown as subscripts in nanometers. The life times at room temperature are also shown for each transition. 21
Figure 2.3: The all-*trans* (before photoisomerization) and 13-*cis* (after photoisomerization) configurations of BR [40]. 22
Figure 2.4: (A) 1 transparent SnO_2 conductive layer, 2 BR film, 3 aqueous electrolyte gel layer 4 Au layer, 5 Teflon ring spacer, 6 glass substrate (B) An 8×8 array of BR photocells [51]. 25
Figure 2.5: Fabrication of BR sensor. (A) BR suspension on ITO-PET; (B) electrophoretic sedimentation; (C) placing the insulation (Kapton film) between ITO layers and completing the BR sensor; (D) Control sensor is the same as BR sensor without the BR deposition. 27
Figure 2.6: Schematic diagram of the radiation sensor based on BR and the measurement set up. 28
Figure 3.1: Snapshot of WinXCom program. 32
Figure 3.2: Mass attenuation coefficients of amino acids of bacteriorhodopsin. Inset shows the mass attenuation coefficient of bacteriorhodopsin for different interactions. 34
Figure 3.3: Effective atomic number of bacteriorhodopsin for partial and total interactions. 36
Figure 4.1 Varian linear accelerator in Grand River Cancer Centre, Kitchener, Ontario. This machine has been used as an X-ray source for characterization of the fabricated sensors. 44
Figure 4.2: Electrical current induced in the flexible BR sensor under 0.2 minute of 6 MV X-ray radiation. Different dose rates are applied (100 MU/min – 600 MU/min) and the field size is 10 cm × 10 cm. (A): Response of the control sample (substrate only). (B): The sensor (substrate + BR) shows an up and down in the beginning and then the current becomes stable. (C): The current generated by BR molecules only. 46
Figure 4.3: Increasing the energy from 6 MV to 15 MV causes a rise in the induced current for different dose rates. (A): control sample (substrate); (B): sensor (substrate + BR); (C): BR only. (field size = 10 cm × 10 cm). 47
Figure 4.4:(A): Effect of choosing different X-ray radiation field sizes on the induced current. The sensor (substrate + BR) is irradiated with 100 MU of 15 MV X-ray radiation and under the dose rate of 600 MU/min. (B) The sensor (substrate + BR) is irradiated with different doses of 6 MV X-ray radiation (100 MU-600 MU) under constant dose rate of 600 MU/min. The radiation induced charge

is calculated by integrating the current over radiation time. Sensor shows an excellent linear response to the dose increase (field size = 10 cm × 10 cm). 49
Figure 4.5: Repeatability test result of real time current induced in the BR sensor (substrate + BR) under 15 MV X-ray radiation with dose rate of 600 MU/min (field size = 7.5 cm × 7.5 cm). 51
Figure 4.6 Superficial X-ray source used for characterization of radiation sensors under kilovoltage X-ray beam 57
Figure 4.7: Response of BR sensor under dose rates of 50 cGy/min (blue), 100 cGy/min (red) and 150 cGy/min (black) for tube potential energies of 100 kVp , 120 kVp and 150 kVp. For each energy, response of control sample (sensor without BR) for three dose rates are also presented, which have lower values comparing with BR sensor. X-ray machine is on at point A, however it does not reach its set values before point B. X-ray is off at point C. For each tube potential energy, the moving average is calculated based on sets of 10 data points and shown on right. 59
Figure 4.8: BR sensor for radiation dose measurement. Sensor is placed under 80 kVp X-ray radiations for 0.5, 1, 1.5, 2 and 2.5 minutes. 61
Figure 4.9: Response of BR sensor under different field sizes for 80 kVp X-ray radiation with dose rate of 291.6 cGy/min (SSD= 15 cm). Values shown on horizontal axis are diameters of the radiation field. The field size is changed by replacing the cones with different diameters at the head of the X-ray machine. 62
Figure 4.10: The sensor is irradiated by 80 kVp X-ray with dose rate of 291.6 cGy/min (SSD= 15 cm) for 12 s followed by 12 s of relaxation time and this process is repeated for 5 times. 64
Figure 5.1: Transferring the PDMS layer to the PET ITO sheet using uncured PDMS to bond the two. 68
Figure 5.2: PET-ITO sheets mounted to microscope slides, sitting in the bath solution. 68
Figure 5.3: Laser etch cutting through surface layers to fabricate the sensing area, preventing electrical connections across etch. 69
Figure 5.4: Top electrode: cold solder is used to bridge the gap from the etch to connect the gold layer to the ITO. Bottom electrode: ITO. 70
Figure 5.5: Summary of fabrication process of bismuth sulfide sensor. 71
Figure 5.6: Etch design for an array of 3 × 3 sensors on a 50 mm×70 mm sheet and the fabricated array of sensors. 72
Figure 5.7: Diagnostic X-raymachine used for characterization of radiation sensors under kilovoltage 73
Figure 5.8: (a) Fabricated sensor is comprised of 4 layers: a flexible PET substrate, ITO, a thin film of bismuth sulfide and a layer of gold; (b) SEM image of thin film of Bi_2S_3. The scale bar is 200 nm; (c) This sensor is mechanically flexible. Photon mass attenuation coefficients of each layer are calculated for photons energies in the range 10-150 keV (d) Au; (e) bismuth sulfide; (f) ITO; (g) PET; 75
Figure 5.9: Formation of bismuth sulfide thin film on ITO surface is confirmed by energy-dispersive X-ray spectroscopy. 76
Figure 5.10: Reading was taken by Au- (Bi_2S_3)-ITO-PET sensor for X-ray radiation.This was repeated 4.5 s later. Machine was set for typical exposure parameters for a new born child chest X-ray

image, thus: 0.5 mAs, 20 ms, 40 kV_p tube potential, 12 cm × 20 cm field. The applied bias voltage was 1µV. 77
Figure 5.11: Changing mAs from 40 to 160 and measuring current per sensor area by Au- (Bi_2S_3) -ITO-PET sensor (black). Result is compared with the control sensor (red) which does not have the bismuth sulfide layer. The setting on the X-ray machine was as following: 500 ms, 40 kV_p tube potential, 5 cm × 3 cm field. The applied bias voltage was 1mV. Inset shows reading of a Farmer ion chamber under the same experiment conditions. 78
Figure 5.12: Changing tube current from 400 mA to 560 mA on X-ray machine and measuring current with Au- (Bi_2S_3) -ITO-PET sensor. The setting on the X-ray machine was as following: 200 mAs, 40 kV_p tube potential, 20 cm × 12 cm field. Inset shows reading of an ion chamber under the same experiment conditions. 79
Figure 5.13: Changing tube potential from 40 kVp to 150 kVp on X-ray machine and measuring current with Au- (Bi_2S_3) -ITO-PET sensor. The setting on the X-ray machine was as following: 100 mAs, 500 ms, 40 kV_p tube potential, 20 cm × 12 cm field. No bias voltage was applied for current measurement. Inset shows reading of an ion chamber under the same experiment conditions. 80
Figure 5.14: Changing bias voltage and measuring current with Au- (Bi_2S_3) -ITO-PET sensor. The current is increased under radiation (pink). An asymmetry is observed due to the difference in charge to mass ratio of negative and positive charges and ions. The setting on the X-ray machine was as following: 100 mAs, 500 ms, 40 kV_p tube potential, 5 cm × 3 cm field. Inset shows reading of an ion chamber under irradiation for the same setting on X-ray machine. 81
Figure 5.15: Effective atomic number of bismuth sulfide from 10-150 keV photon energies. 82
Figure 6.1: Fabrication of CNT sensor using a capillary tube 91
Figure 6.2: Radiation induced conductivity in carbon nanotube suspension under 15 MV, 600 MU/min X-ray radiation. 92
Figure 6.3: Comparison of calculated relative radiation induced conductivity for different diameters of carbon nanotubes. 93
Figure 6.4: Comparison of calculated relative radiation induced conductivity for different radii of ZnO nanoparticles. 94

List of Tables

Table 1.1: Radiation weighting factor as a function of energy of neutrons. 2
Table 1.2: The range of wavelength, energy and frequency of x-ray and gamma radiations................ 7
Table 1.3: comparison of the advantages in the current dosimetry technology 14
Table 3.1: Molecular formula of comprising amino acids of bacteriorhodopsin. The amino acids in each of the graphs are referred by their number specified in the table. Bacteriorhodopsin contains an Asx1 or an Asx2 as well as a Glx1 or a Glx2 [62]. 33
Table 3.2: Effective atomic numbers of amino acids for total photon interactions (with coherent) at photon energies 10-200 keV.. 38
Table 3.3: Effective atomic numbers of amino acids for total photon interactions (with coherent) at photon energies 1-20 MeV. 39
Table 3.4: Effective electron densities $\boldsymbol{Nel}$ x10^{23} (electrons/g) of amino acids for total photon interactions (with coherent) at photon energies 10-200 keV.. 40
Table 3.5: Effective electron densities $\boldsymbol{Nel}$ x10^{23} (electrons/g) of amino acids for total photon interactions (with coherent) at photon energies 1-20 MeV. 41
Table 4.1: Averaged radiation induced current per area generated from BR molecules only............. 48
Table 4.2: Summary of the tube potential, tube current and beam quality parameters. 56
Table 4.3: Average radiation induced current per area generated in BR molecules only. 60
Table 7.1: Significant advantages of the fabricated sensors.. 98

Chapter 1
Introduction

1.1 General background:

Light is an electromagnetic radiation. Another way of describing light is through particle theory which indicates that light is comprised of photons. When one assumes light as an electromagnetic wave, different wavelengths of light are considered. On the other hand, when light is discussed in particle theory, the energy of photons is considered. According to wave-particle duality principle, all particles exhibit wave and particle properties, however, in an experiment both properties can not be observed simultaneously. The energy of photons and the wavelength of the electromagnetic wave of light are related by the Planck's equation ($E= h\,\nu=h.c/\lambda$) with Planck constant $h = 6.626\times10^{-34}$ J.s. This equation is also valid for other particles such as electrons and protons.

The visible part of light spectrum has the wavelength between 380 nm and 740 nm, which are the upper boundary of UV and lower boundary for infrared, respectively. Part of the light spectrum with wavelength lower than UV is comprised of X-rays and gamma rays. The detection and measurement of the X-ray radiation is the topic of this thesis.

1.2 Units of measurement in radiation sensing:

To quantify radiation measurements, several different units of measurement are used. The most applied units of measuring radiation are introduced below:

1.2.1 Unit of measuring radiation energy

Electron volt (eV) is a very common unit of measuring radiation energy. In a closed electrical circuit with a battery and a resistance, the battery creates a potential difference across the resistance. The work done in the electrical circuit is the product of the potential difference and the charge passing through the circuit. As the unit of work is joule, this concept can be used to measure energy. An electron volt is equal to the amount of energy required to pass an electron of charge $e = 1.602 \times 10^{-19}$ C across a potential difference of 1 V.

$1 \text{ eV} = 1.602 \times 10^{-19} \text{ CV} = 1.602 \times 10^{-19} \text{ J}$

$1 \text{ MeV} = 1.602 \times 10^{-13} \text{ J}$

1.2.2 Units of measuring radiation dose

The energy deposited in or absorbed by unit mass (1 kg) of an irradiated material from radiation is called Gray (Gy), which is the SI unit for absorbed dose. The older unit is the “rad”:

1 rad = 0.01 Gy

1.2.3 Unit of measuring equivalent dose and effective dose

The effective biological damage of the radiation depends on the absorbed dose by the human tissue and the type of radiation. For the same amount of the absorbed dose, the biological effect can be different for different types of radiations. This can be taken into account by defining a radiation weighting factor (WR), which is a coefficient that is multiplied by the absorbed dose to show the associated equivalent dose. The SI unit for equivalent dose is Sievert (Sv)

equivalent dose (Sv) = absorbed dose (Gy) × radiation weighting factor

WR is equal to 1 for X-rays, gamma rays and beta particles (e^- and e^+) absorbed by human tissue, 20 for alpha particles (He^{2+}) and a function of energy for neutrons.

Table 1.1: Radiation weighting factor as a function of energy of neutrons.

Energy of neutrons	radiation weighting factor
E< 10 keV	5
10 keV<E<100 keV	10
100 keV<E<2MeV	20
2 MeV<E<20 MeV	10
20 MeV<E	5

The biological damage also depends on the irradiated organ. The effective dose (Sv), is defined as the product of the equivalent dose and tissue weighting factor (WT). If more than one organ is irradiated, the effective dose is the sum of all the effective doses.

effective dose (Sv) = equivalent dose (Sv)× tissue weighting factor

1.2.4 Unit of measuring radiation exposure

Exposure is the measurement of the ability of radiation to ionize air and create electric charges. The unit of exposure is roentgen (1 R = 2.58×10^{-4} c/kg of air). One roentgen of gamma or X-ray radiation creates ~ 10 mSv tissue dose [1].

1.2.5 Unit of measuring the machine output

Linear accelerators are employed in radiation therapy and their output is measured using monitor unit (MU).These radiation sources are calibrated for a specific energy spectrum such that 1 MU gives an absorbed dose of 1 cGy under reference conditions (i.e. field size of 10cm×10cm, source-axis distance (SAD) of 1 m, etc) [1].

1.3 X-ray generation mechanisms

X-rays were discovered by Rontgen in 1895 when a high electric voltage was passed through a cathode ray (stream of electrons) tube filled with gas. He covered the tube, however he observed a fluorescent light on a screen close by. He named this radiation X-rays.

X-rays are generated as a result of the impact of accelerated electrons and a target atom. Two atomic processes can produce X-rays:

1.3.1 Bremsstrahlung (braking radiation)

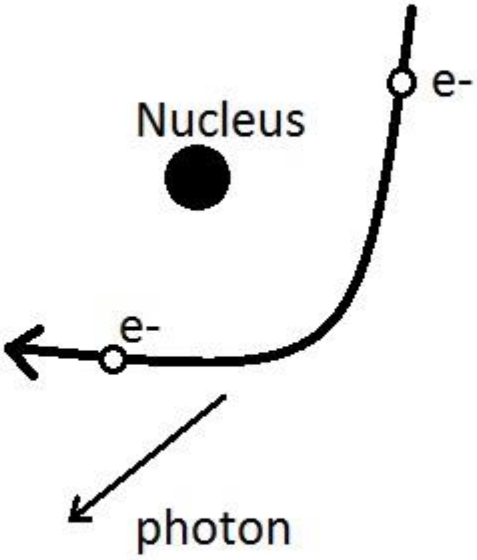

Figure 1.1: Bremsstrahlung (braking radiation)

In Bremsstrahlung process, the incident electron interacts with the electrons of the target atom through electromagnetic forces and it is slowed down. If the energy of the incident electron is high enough, the change in the kinetic energy of the incident electron as it slows down appears as X-ray photons. The energy of none of the generated X-ray photons exceeds the initial kinetic energy of the incident electron. The positive electric field of the nucleus may be strong enough in heavy elements to bring the incident electron to complete stop. In this case, the total kinetic energy of the electron will be emitted as X-ray radiation. X-rays generated from Bremsstrahlung process have a continuous spectrum.

1.3.2 Characteristic emission

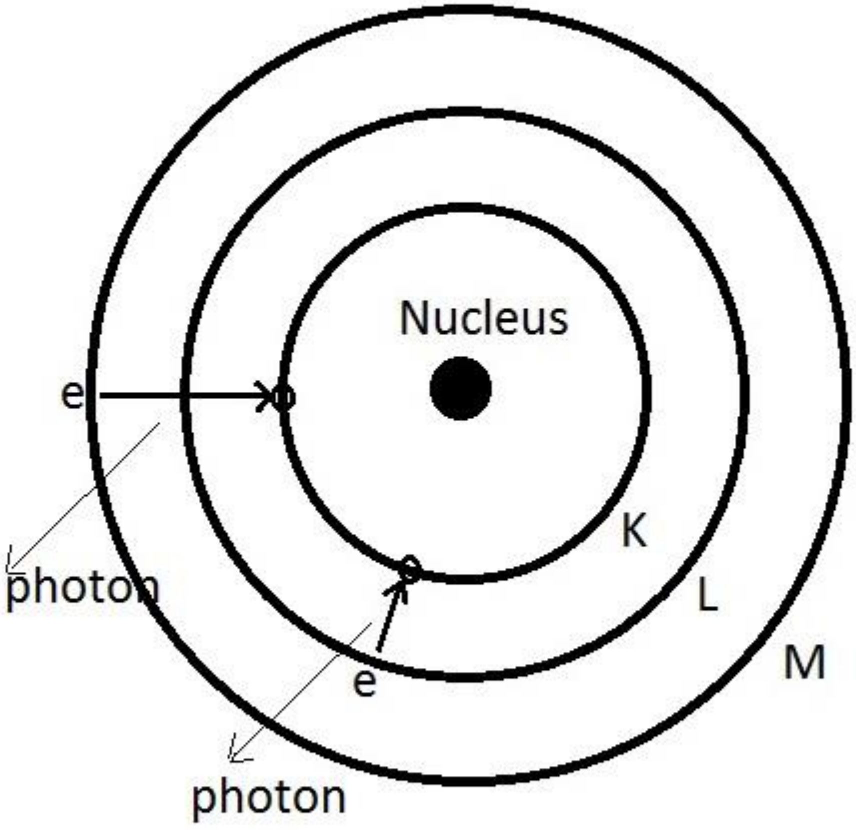

Figure 1.2: electron transitions in lower energy levels of atoms and generated characteristic X-ray photons

Characteristic X-rays are generated from electron transitions in lower energy levels of heavy atoms. K-shell (n=1) is the lowest energy level of an atom. If the energy of the incident electron is large enough to knock out an electron from K-shell, another electron from a higher energy level will fill the position of the released electron. The difference in the initial energy level of this electron and the K-shell appears as an X-ray photon. The X-rays are called K_α and K_β if the transitions are from n=2 (L-shell) to n=1 and from n=3 (M-shell) to n=1, respectively. The emitted characteristic X-rays have sharp peaks in certain energies associated with the difference between the atomic energy levels of the target atom.

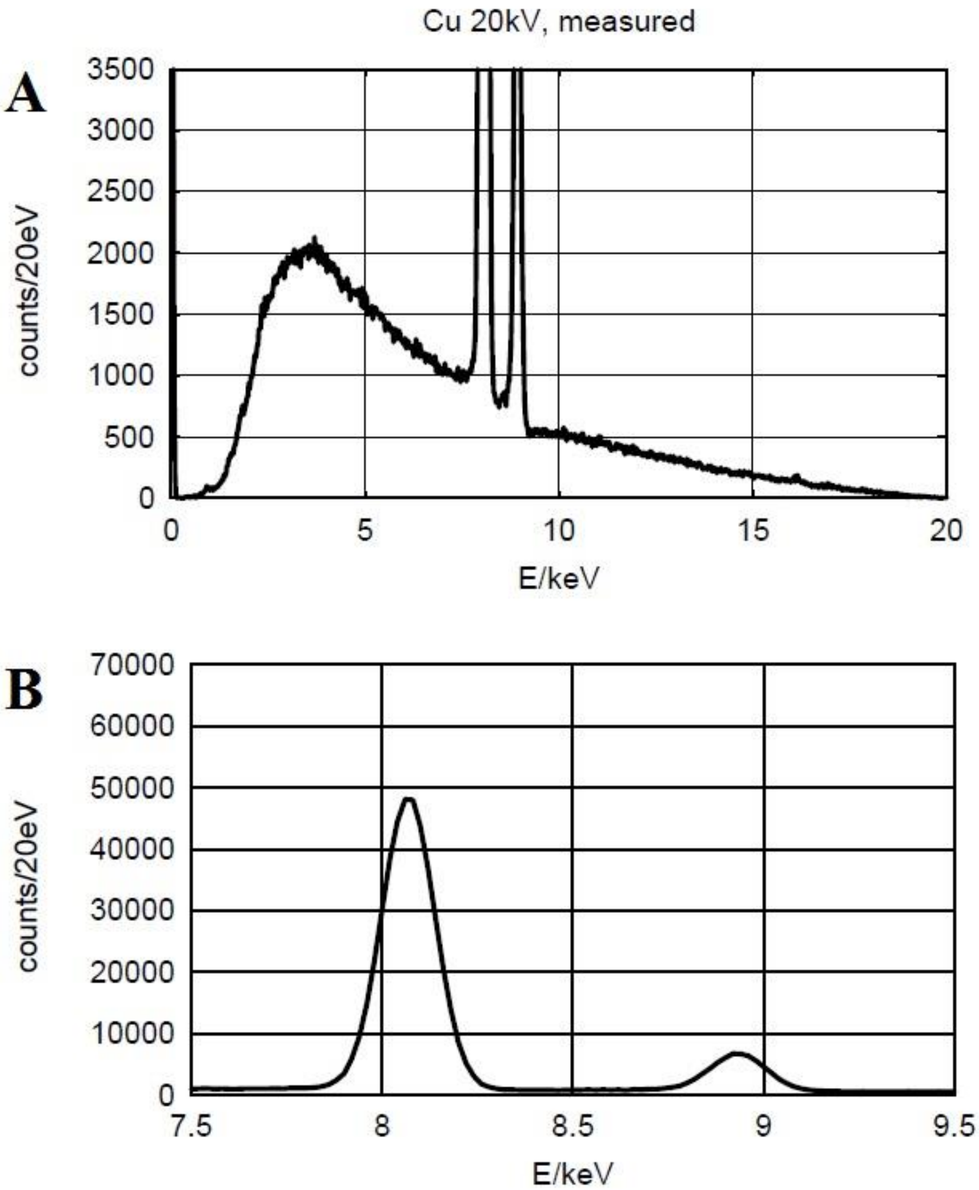

Figure 1.3 Measured X-ray spectrum of Cu. The characteristic Cu K_α and Cu K_β radiation peaks in the photon energy range from 7.5 to 9.5 keV are shown in B [2].

1.4 Interaction of X-ray photons with matter

X-ray and gamma photons can penetrate and transmit through the irradiated matter without interacting, or can interact and be scattered or absorbed by the medium. The wavelength of these radiations is within the range 10^{-4} A$^\circ$ to 100 A$^\circ$. The associated energy and frequency can be calculated by Planck's equation.

The transfer of energy of X-ray photons to the irradiated matter occurs through the process whereby an X-ray photon transfers its energy to an electron ejecting it from the atom and the electron depositing its energy to the medium through excitation and ionization. In ionization, an electron is removed from the atom or molecule and the target is left with a net positive charge. In excitation, an electron receives part of the energy of the photon and moves to a higher level of energy. X-ray photons interact with matter through several processes. The most important ones are described below:

Table 1.2: The range of wavelength, energy and frequency of x-ray and gamma radiations.

Wavelength	10^{-4} A°	100 A°
Energy	0.124 GeV	124 ev
Frequency	3× 10^{16} MHz	3× 10^{10} MHz

1.4.1 Coherent scattering

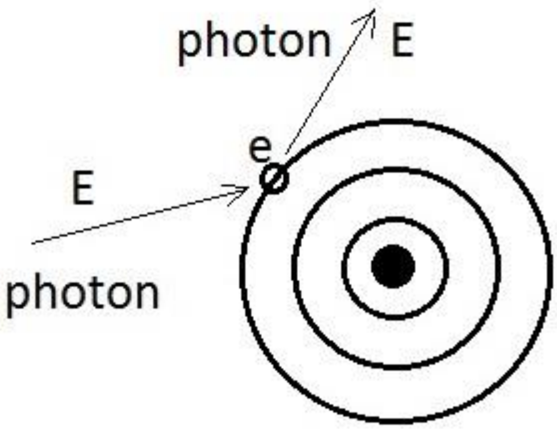

Figure 1.4: coherent scattering

In coherent or Rayleigh scattering, the incident photon interacts with an orbit electron without any energy transfer and it is scattered at a small angle [3]. The energy of the scattered photon is the same as the energy of the incident photon. Coherent scattering is likely to occur in the interaction of low energy photons with high atomic number targets.

1.4.2 Photoelectric effect

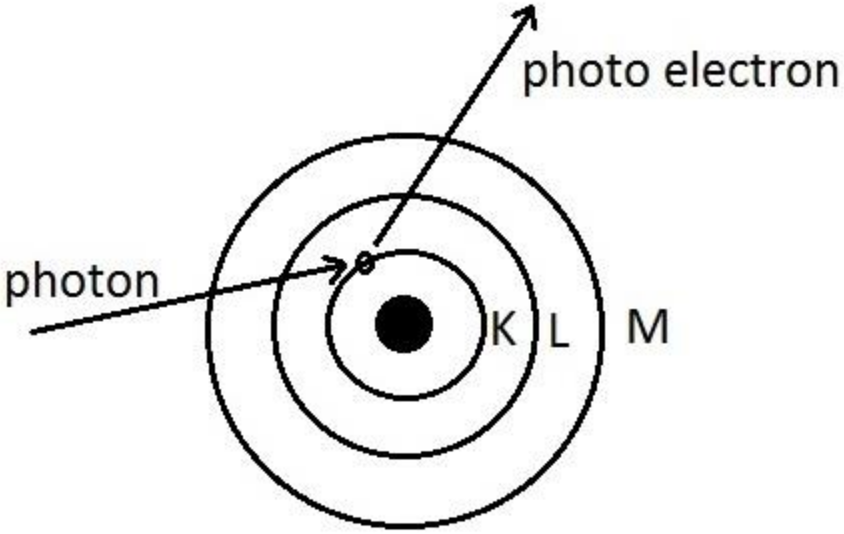

Figure 1.5: photoelectric effect

In photoelectric effect, a photon interacts with an electron (usually the innermost electrons) and the energy of the X-ray photon is completely absorbed by the electron ejecting it from the atom [3]. Part of this energy is required to overcome the electron binding energy to release the electron from the atom. The rest of the energy of the photon appears as the kinetic energy of the released electron also known as the photoelectron. According to the conservation of energy one can write

$$E_P = WF + KE,$$

where E_p is the energy of the incident X-ray photon, WF is the work function of the material which defines the binding energy of the electron, and KE is the kinetic energy of the released photoelectron. The atom is then left in the excited state and the electron vacancy is filled by an outer orbital electron with the emission of characteristic X-rays. Absorption of the produced characteristic X-ray photons results in the production of mono-energetic Auger electrons.

1.4.3 Compton scattering

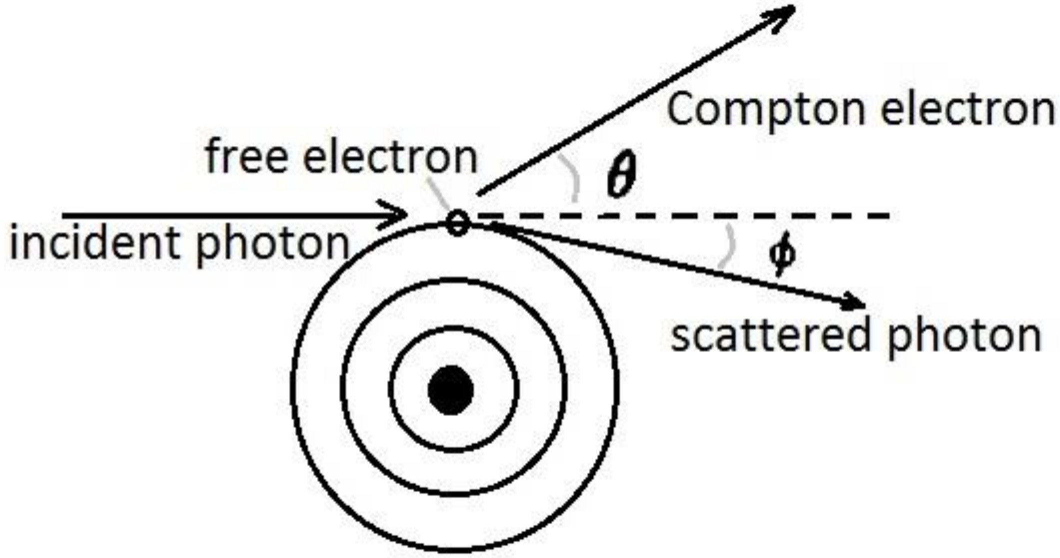

Figure 1.6: Compton scattering

If the energy of the incident photon is much more than the binding energy of the interacting electron, the electron interacts with the photon as a free electron [3]. The photon interacts with the free electron transferring part of its energy to it and ejecting it from the atom. The rest of the energy appears as the energy of the scattered photon which is lower than the energy of the incident photon. This is observed as a scattered photon with longer wavelength and a recoil electron. The energy and direction of the recoil electron and scattered photon can be calculated using conservation of energy and momentum:

$$\lambda_f - \lambda_i = \Delta\lambda = \frac{h}{m_e c}(1 - \cos\theta) \qquad (1.1)$$

In this equation, λ_i is the wavelength of the incident X-ray photon and λ_f is the wavelength of the scattered photon. θ is the angle of deflection of the scattered photon from the direction of incident photon. m_e is the rest mass of the electron.

1.4.4 Pair production

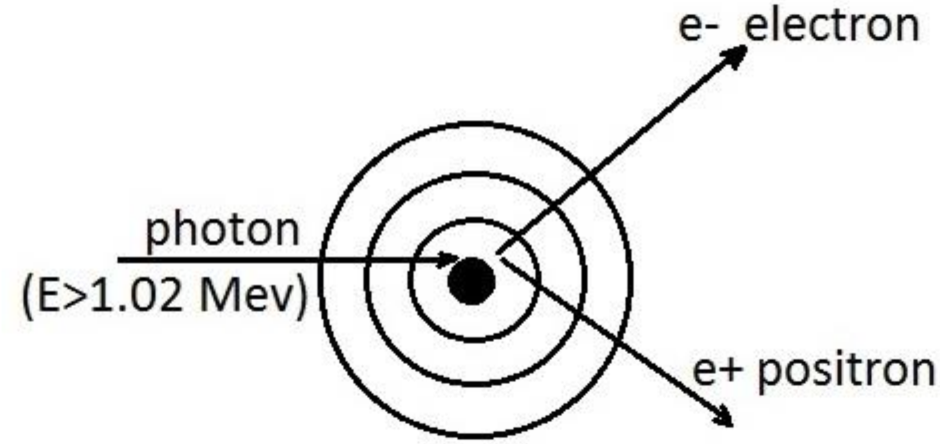

Figure 1.7: pair production

Pair production occurs when the incident photon interacts with the electromagnetic field of the nucleus of the target atom and an electron and a positron are created [3]. Positron has the same mass as an electron but with opposite electric charge. The rest mass of an electron is 0.51 MeV and so the minimum photon energy required for pair production to occur is 1.02 MeV. The kinetic energy of the electron and positron is originated from the difference of the energy of the incident photon and 1.02 Mev. It is also worth mentioning that pair production is an example of conversion of energy to mass according to Einstein's mass-energy conversion equation $E=mc^2$.

1.5 Radiation measurement devices for medical applications

1.5.1 Ionization Chamber

Ionization chamber is based on ionization of gas under X-ray radiation, creation of electron- ion pairs and collection of the charged particles [4], [5], [6], [7], [8]. At higher intensities of photons, higher number of electron-ion pairs are created and collected. The effective voltage inside the chamber at time *t* can be written as the following:

$$V_{eff}(t) = V_0 - V_{np}(t) \qquad (1.2)$$

V_0 is the static potential applied across the electrodes and $V_{np}(t)$ is the potential difference created by the negative and positive charges inside the chamber at time t. According to conservation of energy, the total potential energy due to the potential V_0 is equal to the addition of the potential energy of the charged particles inside the chamber and their kinetic energy [8],

$$\frac{1}{2}CV_0^2 = \frac{1}{2}CV_{np}^2 + N_0eEv_nt + N_0eEv_pt \qquad (1.3)$$

In this equation, the chamber has been assumed to be comprised of two parallel flat electrodes. $\frac{1}{2}CV_0^2$ and $\frac{1}{2}CV_{np}^2$ are the potential energy delivered by the voltage V_0 and V_{np}, respectively. N_0eEv_nt and N_0eEv_pt are also kinetic energies of the negative and positive charges inside the chamber. E is the intensity of the electric field ($E= V_0/d$, d= distance between electrodes), v_n and v_p are the average velocities of negative and positive charges, and N_0 is the number of ion pairs at time t. The above equation can be simplified as the following:

$$(V_0 - V_{np})(V_0 + V_{np}) = \frac{2N_0V_0e}{Cd}(v_n + v_p)t \qquad (1.4)$$

Assuming $V_0 + V_{np} \approx 2V_0$ we can finally find V_{eff},

$$V_{eff}(t) = \frac{N_0e}{Cd}(v_n + v_p)t \qquad (1.5)$$

The advantages of an ion chamber are as following:

(i) The ionization current is independent of the applied voltage. Therefore, small fluctuations in the supplied bias voltage do not affect the measurement.

(ii) The saturation current is proportional to the deposited energy by radiation.

The disadvantages of the ion chamber can be listed as following:

(i) Measurement of low current generated by low radiation requires shielding and low noise electronics.

(ii) The atmospheric conditions such as pressure and temperature may change the output of the ion chamber.

1.5.2 Thermoluminescence dosimeter

Certain materials such as lithium fluoride show thermoluminescence property. Electrons which have been moved out of their initial state upon receiving X-ray or gamma photons, are trapped within lattice defect sites [9]. Heating causes the trapped electrons to return to their initial states. This return is compensated by emission of photons. Under controlled heating conditions, the intensity of photons can quantify the absorbed radiation dose. This phenomenon is called thermoluminescence and the materials which have this property are used in thermoluminescent dosimeters (TLDs). These materials store the energy of the radiation and release the energy as photons upon heating which can be used to measure the integrated doses. This is useful in monitoring the total dose received by personnel and sensitive equipment over longer periods of time [10], [11]. Thermoluminescent materials are packaged as small sealed capsules or they are homogenously mixed with polymers and plastic materials. After being exposed to radiation, TLDs are placed in a precisely temperature controlled electric heater and their photon emission is read.

Each thermoluminescent material has its own characteristic “glow curve”. The output light intensity versus temperature is plotted to get the glow curve of the TLD. The total area under the curve is proportional to the accumulated dose. The peaks of the glow curve are associated with the defect energy levels and the height of each peak depends on the absorbed dose, heat transfer rate and the type of the material. The total dose, the energy spectrum and type of the incident radiation are important factors for the choice of the TLD for an application. Sometimes a mixture of materials sensitive to different radiations is used to make a TLD suitable for an environment where different types of radiations are present. Also the fading time of the material has to be negligible in comparison to the time required for irradiation and read out of the TLD. TLDs do not require any electronics for storing the exposure dosage and they are small. TLD needs to be calibrated in order to convert its reading to absorbed dose.

1.5.3 Radiochromic film

Irradiation changes the color of radiochromic materials [12]. The color or image formation is initiated through a chemical process in which the energy of the X-ray photons is transferred to the receptive part of the leuko-dye or colorless photomonomer molecule. A leuko dye contains molecules which can acquire two forms, one of which is colorless [13], [14].

The color change depends on the absorbed radiation dose and can be observed under white light. Darker areas of the film block the light. The absorbed dose is proportional to the logarithm of the ratio of the intensity of the incident beam (I_i) to the intensity of the transmitted beam (I_t),

$$D \propto \log(\frac{I_i}{I_t}) \quad (1.6)$$

This technique of dosimetry provides high level of spatial resolution and uniformity. The spatial resolution depends on the size of the monomer crystals used in the films which can be within sub-micron range. However, the radiochromatic films are sensitive to UV light and temperature.

1.5.4 MOSFET dosimeters

Metal oxide semiconductor field effect transistor (MOSFET) is a relatively miniaturized and accurate dosimeter [15], [16], [17], [18], [19], [20]. Radiation creates electron-hole pairs in the oxide region, which changes the threshold voltage of the MOSFET. This change can be used as a measure of the deposited energy by radiation. The small size of the MOSFET provides high spatial resolution and in vivo usage capability. However, MOSFETs are very sensitive to instabilities in bias voltage and fluctuations in temperature. They also have a short life time due to structural damage under radiation. MOSFETs have applications in photon, electron and proton radiation dosimetry.

Table 1.3: comparison of the advantages in the current dosimetry technology

	Real time/ no post processing	Miniaturizable/ miniaturized	Long life time	No bias voltage	No high voltage source
TLD		✓	✓	✓	✓
Ion chamber	✓		✓		
Film			✓	✓	✓
MOSFET	✓	✓			✓

1.6 Research objectives

The research objectives of my PhD program have been the design, fabrication and characterization of novel radiation sensors. The work includes (i) application of new materials for the purpose of radiation measurement and (ii) understanding the radiation sensing mechanisms involved. In this work I have fabricated several radiation sensors for detection and measurement of X-rays. The sensors are fabricated on a mechanically flexible substrate which adds to their potential applications. The fabricated sensors are characterized at Grand River Cancer Centre and Grand River Hospital in Kitchener, Ontario, Canada.

My original contributions to knowledge in this thesis are as following:

(i) An X-ray sensor was fabricated using Bacteriorhodopsin (BR), a proton pump protein in the cell membrane of *Halobacterium Salinarum*. This sensor was used to measure dose and dose rate in the kilovoltage and megavoltage energy range.

(ii) The mass attenuation coefficients, effective atomic numbers and electron densities of BR and its comprising amino acids have been calculated for 1 keV-100 GeV.

(iii) An equation for radiation induced conductivity for nanoparticles is given. Relative radiation induced conductivity for ZnO nanoparticles with different radii and carbon nanotubes with different diameters have been calculated.

(iv) Laser micromachining and chemical deposition techniques have been used to fabricate an X-ray sensor based on thin film of bismuth sulfide. This sensor has been characterized under an X-ray machine with keV energy beam.

1.7 Thesis scope

This thesis is organized in 7 chapters. There are 5 core chapters which address the research objectives. The results of chapters 2-4 have been published in 3 journal papers in "*Biosensors and Bioelectronics"*[21], *"Sensors and Actuators B: Chemical"* [22] and *"Nuclear Instruments and Methods in Physics Research B: Beam Interactions with Materials and Atoms"*[23] . The results of chapter 5 have been published in a conference paper in *Proceedings of the IEEE 11th International Conference on Nanotechnology (IEEE Nano 2011, Portland, Oregon, USA)*[24]. The author of this thesis is the first author of the above papers.

In Chapter 2, design, fabrication and characterization of a radiation sensor based on bacteriorhodpsin is presented. This sensor was fabricated on a flexible substrate and was tested under a LINAC X-ray source with MeV energy X-ray beam.

In Chapter 3, characterization of the bacteriorhodopsin sensor under keV X-ray radiation is presented. The source of X-ray for these experiments was a Gulmay Medical D3000 DXR superficial X-ray machine.

In Chapter 4, a theoretical study of the interaction of X-ray photons with bacteriorhodopsin and its comprising amino acids is provided for energy range of 1keV-100 GeV.

In Chapter 5, the theory of radiation induced conductivity is applied to nanoparticles. The goal is to understand and study the change of radiation induced conductivity with the size of the materials in nanometer scale and to look at the possible applications of nanomaterials in fabrication of radiation sensors.

In Chapter 6, fabrication and characterization of a radiation sensor based on thin film of bismuth sulfide is provided.

In Chapter 7, the conclusion of this thesis is presented and recommendations regarding the future possible work are provided.

Chapter 2

Bacteriorhodopsin

There are many organisms in nature which react to light. Absorption of photons in certain wavelength by the photosensitive organism may trigger a response in its cell membrane. This response could be charge separation or may be directing a flow of ions into or out of the cell which leads to generation of an electrical potential in the structure of the organism.

There are only two main types of photoreceptor molecules in nature: retinal proteins (rhodopsins) and chlorophylls [25]. Chlorophylls have vegetative and bacterial origin and exist in leaves of plants, seaweed and bacteria. Rhodopsins have visual and bacterial nature. There are two absorption peaks in the absorption spectrum of natural chlorophylls in the blue and near infrared. Natural retinal protein complexes absorb a wide range of spectrum from UV to red.

Visual rhodopsin experiences a series of electrostatic changes upon receiving and absorbing a photon. The electrostatic changes will lead to conformational changes in the structure of the protein as well as electrical stimulation of optic nerve. In contrast, bacterial rhodopsin is a molecular photosensor which assists the organism in its orientation. The bacterial rhodopsin was discovered in 1971 in a group of bacteria called Halobacteria which lives in salt saturated (or nearly saturated) water [26]. Bacteriorhodopsin (BR) is a proton pump protein in the cell membrane of *Halobacterium salinarum*. This cell membrane is called purple membrane (PM) due to its color and is comprised of a two-dimensional hexagonal unidirectional crystalline array of BR molecules and lipids [26], [27], [28], [29]. The absorbed energy of light in BR is used for hydrogen ion transport across the cell membrane, to generate a potential difference which is necessary for the synthesis of adenosine triphosphate (ATP) from adenosine diphosphate (ADP). This photosynthesis is different from that of chlorophyll. In chlorophyll, absorption of light energy leads to separation of electric charges and generation of electrochemical potential difference on the membrane [30].

Isolation of BR form bacterial membrane in 1973 has attracted a lot of attention due to BR’s distinct properties. BR is different from visual rhodopsin in its exceptional stability and functioning in harsh conditions and its reversible photocycle.

2.1 Synthesis of PM

Halobacteria can be cultivated in lumostats in lab, at 30-40° C with a cell division period of 7-8 hours. The total cultivation time may vary between 3 to 7 days. Several factors such as temperature, pH, light intensity, light spectrum and the chemical composition of the medium may affect the concentration of BR the cells [31]. Under light exposure, PM is synthesized by the cells and the ATP content is highly increased. An anaerobic method of growth of halobacteria is described in [32]. The obtained biomass is suspended in water mixed with DNAse enzyme. The suspension is centrifuged several times after osmotic shock and DNA splitting. Centrifuging can also be replaced by filtering. The sediment of the centrifuging process is pure PM which can be suspended in distilled water to the required concentration or can be dried in a lyophilizer (freeze-dryer). 400-600 mg of dry PM can be obtained from 10 liters of culture extract [25].

2.2 Properties of PM and BR

BR molecules form 75% of the structure of the PM by weight. The rest of PM is comprised of lipids. A PM patch may have up to 1 μm width and 4.5-5 nm thickness. The BR molecule has a molecular weight of 26.534 DA. The purple membrane is a very stable biomaterial. The concentration of the salt in the Dead Sea, a habitat of halobacteria, reaches 34%. PM is able to keep its properties over a range of 0–12 pH, and up to 140 °C in dry shape and over 80 °C in water conditions [33], [34]. A concentrated suspension of PM in water can be stored in room temperature for weeks. The refrigerated suspension at 5-8 ° C, and the freeze-dried form can be used for years. Monomolecular BR is not stable and what is used is PM or a BR molecule in a lipid medium [25].

Such properties are important for the potential applications of BR in the fabrication of micrometer and nanometer scale devices, structures and patterns for a wide range of applications [35], [36]. In most cases, oriented single or multilayer of BR film is coated on a substrate to maximize the generated signal.

2.3 Methods of coating surfaces with BR for device fabrication

To employ BR in a device, it is necessary to immobilize the protein on a substrate and create a BR-device interface such that BR's functionality is maintained and the protein would not degrade over time. Dry form of BR has several advantages over the suspension form. Applying BR in suspension form in a device requires sealed packaging and which add to the complexity of the device. However, since BR keeps its photosensitive properties in dry form, it does not denature over years in dry shape, and due to simplicity in fabrication, methods of fabrication of dry film of BR are favored. The most important methods of immobilizing BR on a substrate are described below:

2.3.1 Layer by layer electrostatic deposition (LBL-ESD)

At pH > 5, the cytoplasmic side of PM is more negatively charged in comparison to the outside of the membrane. So the cytoplasmic side can be attached to a positively charged surface such as some polyelectrolytes, conductive polymers, enzymes, proteins or nanoparticles. This technique is suitable for creating an interface between BR molecules and other bio/nanomaterials and opens windows to novel functionalities which may lead to fabrication of new devices based on BR [37], [38]**.**

2.3.2 Langmuir-Blodgett (LB)

In LB method, a layer of amphiphilic organic molecules is spread on water and the target substrate is dipped in and out of the water either vertically or horizontally. This method can be used to create single or multilayered ordered films of the amphiphilic molecules on the substrate. The cytoplasmic side of PM is more hydrophilic than the extracellular side and so LB method is a suitable method of creating thin films of BR. This technique is not suitable if thicker layers of BR are required.

2.3.3 Electrophoretic sedimentation (EPS)

PM orients very well in an electric field due to its relatively high permanent electric dipole moment (~ 140 Debye at pH 7 in the suspension form). If a drop of BR suspension is placed between two parallel electrodes and an electric field is applied between the electrodes, the PM patches will move and sit on the anode. EPS method has several advantages over other methods of fabricating a thin film of BR. Thin films of BR created by EPS technique show high degree of orientation and produce higher photocurrents [39].

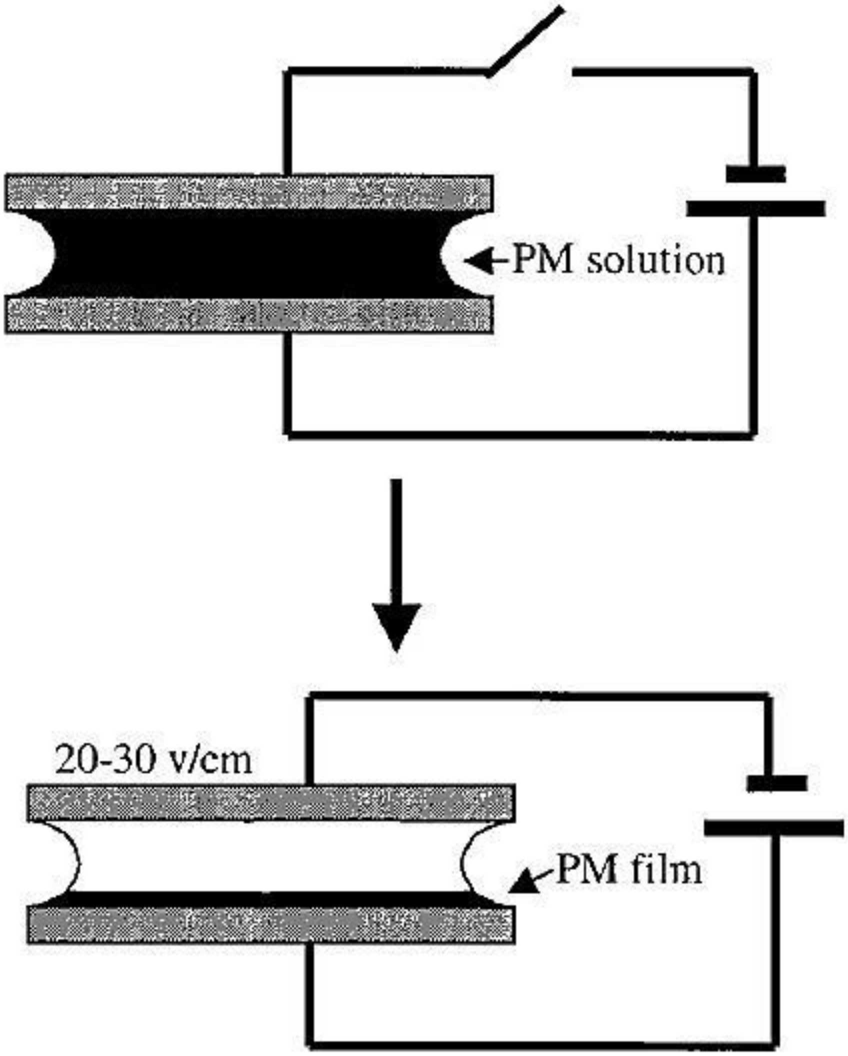

Figure 2.1: EPS method of coating BR on conductive substrates [39].

2.4 Photocycle of BR

The photocycle of BR consists of several intermediate states. K, L, M, N, O are the intermediate states of the photocycle and bR is the initial resting state. Each intermediate state has an absorption peak and a life time. The photocycle is completed in millisecond time range. After absorption of light photon by the retinal chromophore in the bR state, the all-*trans* BR retinal structure converts to a 13-*cis* state and several structural rearrangements occur. The release and uptake of the proton occur in the L→M and M→N transitions, respectively[40]. In the intermediate state M, a proton is transferred from the retinal's Schiff base linkage to Asp85 and a proton is released to the extracellular membrane surface [41].

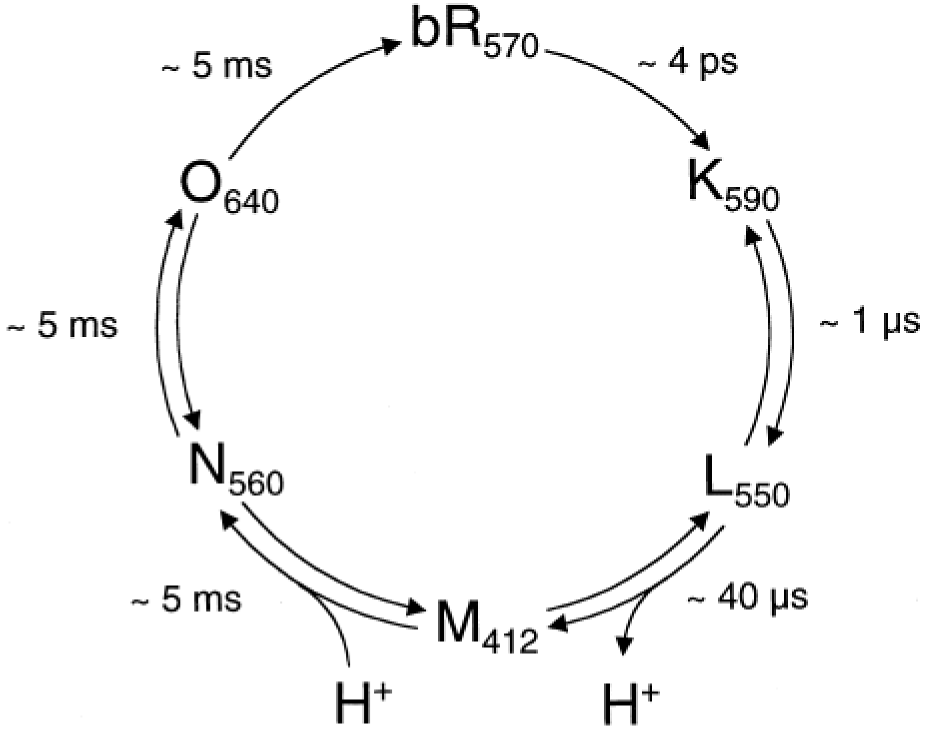

Figure 2.2: Photocycle of BR [40]. K, L, M, N, O are the intermediate states of the photocycle of BR. bR is the initial state. The absorption peaks for intermediate states are shown as subscripts in nanometers. The life times at room temperature are also shown for each transition.

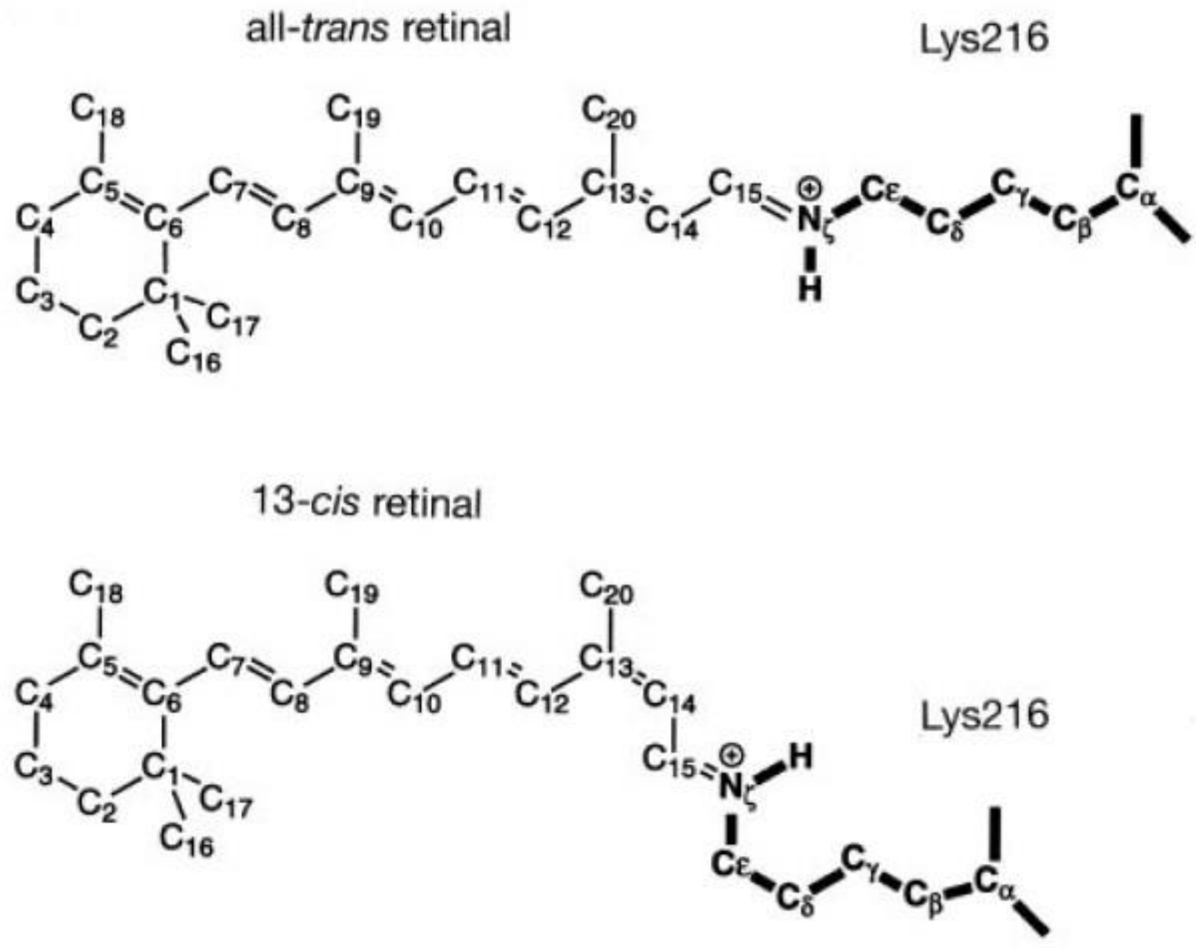

Figure 2.3: The all-*trans* (before photoisomerization) and 13-*cis* (after photoisomerization) configurations of BR [40].

2.5 Electron transport in BR

Proteins can be considered as uniform medium for electrons to tunnel between separated cofactors or they can be viewed as a complex molecular medium with several tunneling pathways [42].

There is limited information about the underlying mechanism of electron transport via BR containing monolayers or single PM patches. The structure of the PM is comprised of BR and lipids. In a study, BR-containing artificial lipid bilayers were sandwiched between two conductive electrodes and the current passing via the lipids and BR were measured. The two major results of this study are as follows: (i) The transmembrane electron transport mainly occurs through BR and not through the lipid bilayers. (ii)

Presence of retinal or a similar π-electron system is an essential requirement for the transmembrane electron transport to occur [43].

Conducting probe atomic force microscopy (CP-AFM) is a technique which has been used to study the electron transport through supported biomembranes [44]. This technique was used to create a conductivity map and to measure current-voltage characteristics of the PM patches. CP-AFM technique showed that the majority of PM patches are not conductive and only 5% of them have nanometric conductive defects [45].

There is a correlation between the conformational change and the variation in the electron transport of BR. Substantial increase in current is observed at a given voltage in the current-voltage curve of BR if it is irradiated by green light after being in dark (which will result in a structural change in the protein) [46]. It has been proposed that the conductivity of BR can be modeled by a sequential tunneling mechanism through amino acids of the protein. The positions of the amino acids defines the conformation of the protein and a light induced conformation change will cause a change in the conductivity of the protein [47].

2.6 Applications of BR

2.6.1 Optical data storage

The initial state bR and the intermediate state M have absorption peaks in the blue (λ_{max} = 570 nm) and green (λ_{max} = 412 nm) part of light spectrum, respectively. The probabilities of the occurrence of bR→M and M→bR reactions after the absorption of a photon (quantum efficiency of the reactions) are 0.65 and 0.95, respectively. Each of the states bR and M can be assigned to a binary state 0 or 1. BR has a very high two photon absorption cross section. An optical system based on two photon absorption can be arranged to use BR as optical data storage [48]. Two laser sources are used such that their beams intersect on BR at the position of reading and writing data and their wavelengths λ_1 and λ_2 satisfy the two photon absorption condition $1/\lambda_{excite} = 1/\lambda_1 + 1/\lambda_2$. Here, λ_{excite} has to match the absorption peaks of the bR or M states. This condition can be fulfilled if $2\lambda_{excite}$ is selected for each wavelength, i.e. 824 nm and 1140 nm. For writing, $\lambda_1 = \lambda_2 = 1140$ nm and $\lambda_1 = \lambda_2 = 824$ nm are used to initiate the bR→M and M→bR transitions, respectively. For readout, two laser beams with wavelengths $\lambda_1 = \lambda_2 = 1140$ nm are applied and if BR is in its initial state, there will be a transition to M state and as a result an electric signal can be recorded [28].

2.6.2 Solar cell

BR can be used as an energy conversion system and it has been employed in fabrication of solar cells. One group have fabricated a solar cell using a mutant of BR interfaced with TiO_2 which delivers a short circuit photocurrent density of 0.09 mA/cm^2 and the open circuit photovoltage 0.35 V under an illumination intensity of 40 mW/cm^2 [49]. Another team has achieved conversion rate of 0.5% and short circuit photocurrents of 0.02 mA/cm^2 [50].

2.6.3 Image detector

An 8×8 array of BR photocells was fabricated for the purpose of image detection [51]. Each photocell in this detector has a multi-layer sandwich structure containing layers of SnO_2/ BR/ electrolyte/Au. SnO_2 is conductive and transparent and it can be coated on glass substrates. In this design BR is directly in contact with the SnO_2 electrode and indirectly in contact with Au electrode through electrolyte solution. The photocell responds differentially to the incident light and a photocurrent of 100 nA/cm^2 is observed.

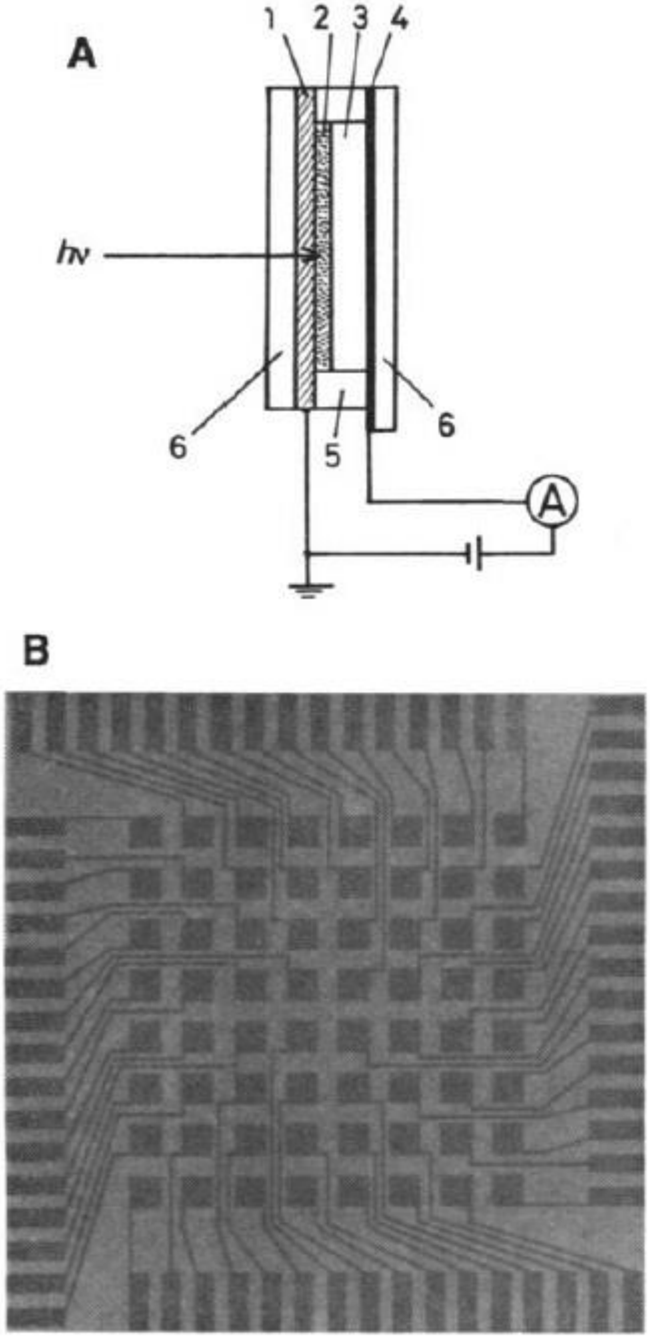

Figure 2.4: (A) 1 transparent SnO_2 conductive layer, 2 BR film, 3 aqueous electrolyte gel layer 4 Au layer, 5 Teflon ring spacer, 6 glass substrate (B) An 8×8 array of BR photocells [51].

2.7 Fabrication of BR sensor

In the fabrication of the radiation sensor, ITO coated polyethylene terephthalate (PET) sheets are used as the main substrate. This substrate is flexible, electrically conductive on the ITO coated side and transparent to a wide range of wavelength [52]. BR is deposited on the conductive side of the substrate using EPS method. 20 µl of BR suspension is inserted between the ITO coated sides of two PET sheets which act as two electrodes. The sheets are separated by two microscope glass slides and ITO electrodes are connected to a voltage supply. An electric potential difference of 3V/mm is applied between the electrodes for 5 min. Higher electrical voltages or a longer time damage the quality of the response of the coated BR. The substrate with the BR is held in a dark box at room temperature for 24 h to get dry. A second sheet of ITO coated PET is placed on top of the first sheet such that the dried BR coating is sandwiched in between. In the area where there is no BR, Kapton Polyimide film (DuPont Electronics Technologies) with 50 µm thickness is used as an electrical insulation between two conductive ITO coated surfaces of the PET sheets. The completed sensor is comprised of the following layers respectively: PET-ITO-(BR, Kapton film)-ITO-PET. The sensing area has a circular shape with radius of 3mm.

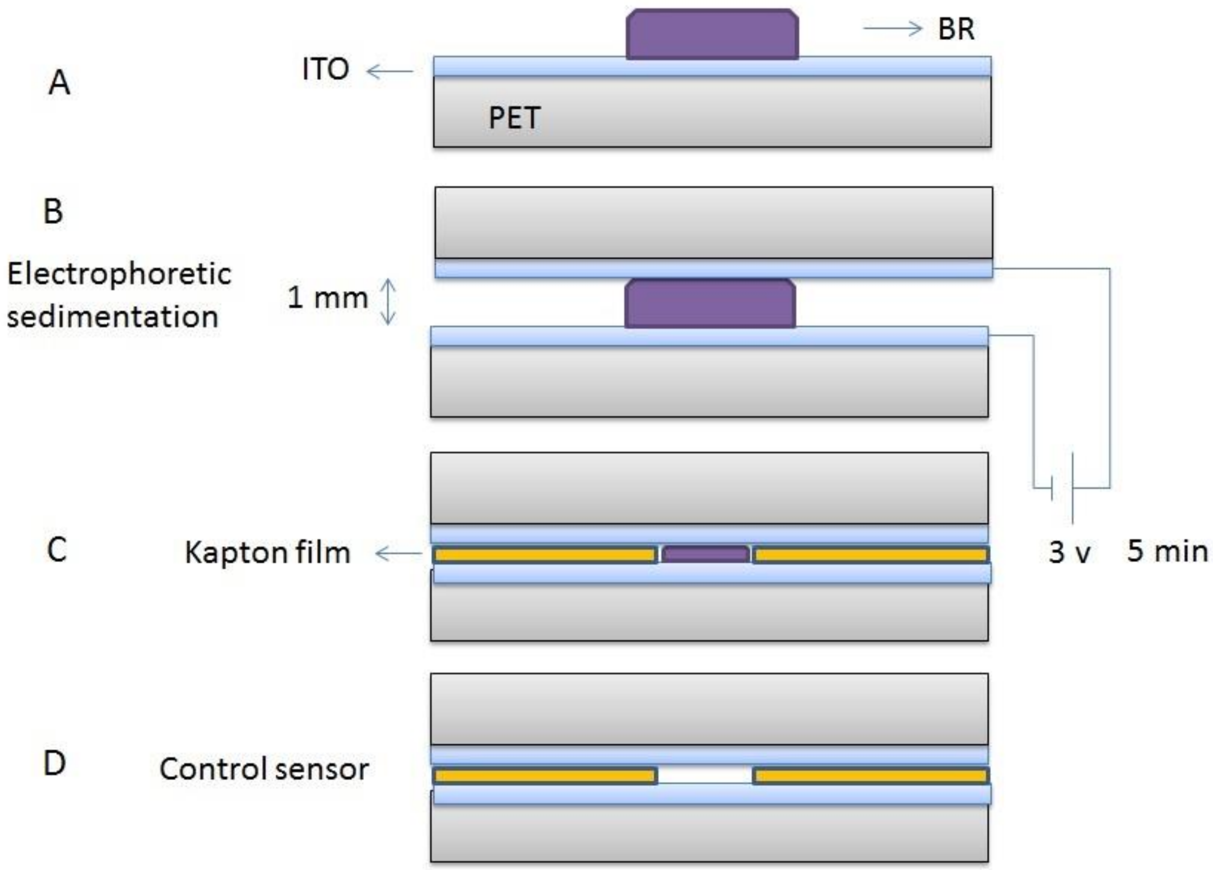

Figure 2.5: Fabrication of BR sensor. (A) BR suspension on ITO-PET; (B) electrophoretic sedimentation; (C) placing the insulation (Kapton film) between ITO layers and completing the BR sensor; (D) Control sensor is the same as BR sensor without the BR deposition.

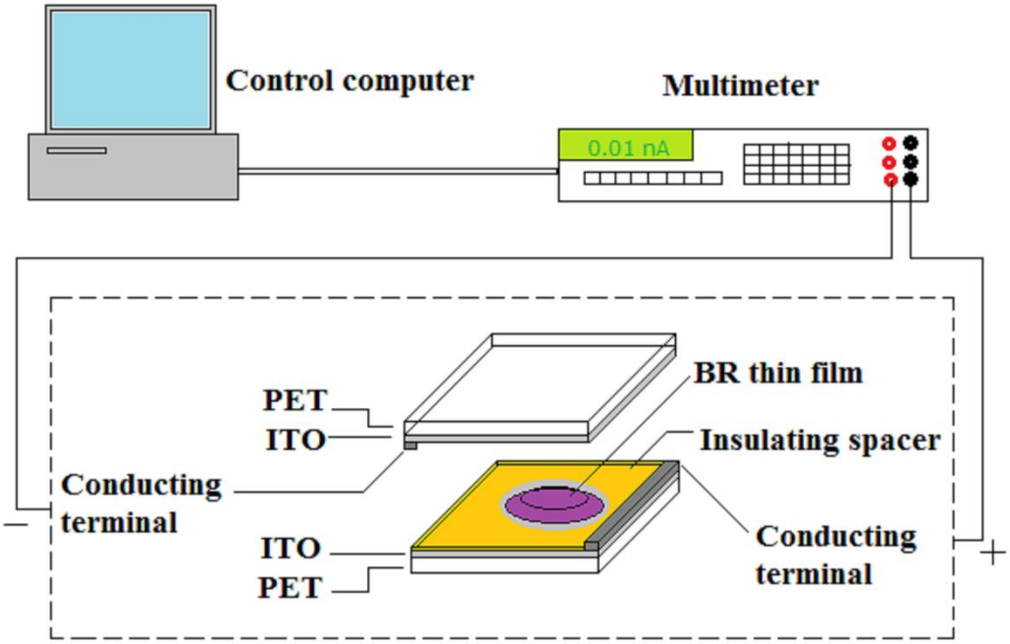

Figure 2.6: Schematic diagram of the radiation sensor based on BR and the measurement set up.

Chapter 3

Interaction of X-ray photons with bacteriorhodopsin

3.1 Mass attenuation coefficient, effective atomic number and effective electron density

An understanding of how sensing materials interact with radiation is essential in the development of radiation sensors. Functional proteins such as BR can be interfaced with solid substrates for fabrication of micro/nano devices and sensors.

The mass attenuation coefficient μ/ρ, effective atomic number Z_{eff} and effective electron density N_{el} are important attributes of a material, as they can be used to better understand the interactions of radiation with a medium. The mass attenuation coefficient of a medium is a measure of penetration of radiation in medium at a given energy. As dominant radiation-matter interaction depends not only on radiation energy but also on the atomic number of the target element, for a mixture or compound an "effective" atomic number is defined. Effective electron density is also determined as number of electrons per unit mass of the mixture or compound. These two values vary with radiation energy. Various studies have been performed to evaluate the above quantities in compounds and mixtures such as alloys, polymers and biomolecules. The values of μ/ρ, Z_{eff} and N_{el} have been calculated for a number of amino acids and compounds containing H, C, N and O in previous studies using a matrix method [53], [54]. In another similar study [55], the Z_{eff} values were determined through experimental data of scattering cross-sections, and confirmed that low Z composite materials interact almost exclusively by incoherent scattering and can be represented by a Z_{eff} that is merely an average atomic number of its constituents for energies of 280-1200 keV. In a number of studies by Manohara, et al. the Z_{eff} values for certain biomolecules were calculated by variaous methods, including a direct and interpolation method [56], [57] and by absorption cross-sections [58]. WinXCom is a program which calculates tables of cross sections for the interactions of photons with any element, compound or mixture for photons with energies between 1 keV to 100 GeV. It is also capable of calculating the interaction coefficients and total attenuation coefficients for compounds and mixtures [59], [60]. Using the coefficients given by WinXCom, the effective atomic number and effective electron densities can be calculated. The Z_{eff} and N_{el} values of many amino acids were experimentally found to be in agreement with calculations of this program [61].

In this chapter, we use WinXCom program to calculate the mass attenuation coefficient of BR and its comprising amino acids for photon energies from 1 keV to 100 GeV. These amino acids include alanine, arginine, asparagine, aspartic acid, glutamine, glutamic acid, glycine, isoleucine, leucine, lysine, methionine, phenylalanine, proline, serine, threonine, tryptophan, tyrosine, valine, Asx1, Asx2, Glx1 and Glx2. We then use that data to calculate effective atomic number and electron densities for the same range of energy. We also emphasize on two ranges of energies (10-200 keV and 1-20 MeV) in which X-ray imaging and radiotherapy machines work.

3.2 Method of Computation

The effective (average) atomic cross-section σ_a and the effective electron cross-section σ_e of a compound can be determined from the following equations [56],

$$\sigma_a = \frac{1}{N_A}\sum_i f_i A_i (\mu/\rho)_i \qquad (3.1)$$

$$\sigma_e = \frac{1}{N_A}\sum_i \frac{f_i A_i}{Z_i}(\mu/\rho)_i = \frac{\sigma_a}{Z_{eff}} \qquad (3.2)$$

where $f_i = n_i / \sum_j n_j$ and Z_i are the mole fraction and the atomic number of the constituent element, respectively. $(\mu/\rho)_i$ is the mass attenuation of the *i*th constituent element. n_i is the total number of atoms of the constituent element in the molecule and $\sum_j n_j$ is the total number of all atoms in the molecule. n_i and A_i are the total number of atoms and the atomic weight of the *i*th element in the molecule, respectively. N_A is Avogadro's Number. The effective atomic number Z_{eff} can be written as,

$$Z_{\text{eff}} = \frac{\sigma_a}{\sigma_e} = \frac{\sum_i n_i A_i (\mu/\rho)_i}{\sum_i \frac{n_i A_i}{Z_i} (\mu/\rho)_i} \tag{3.3}$$

The effective electron density, N_{el} (number of electrons per unit mass) is given as follows,

$$N_{el} = \frac{(\mu/\rho)_C}{\sigma_e} = \frac{N_A}{M} Z_{\text{eff}} \sum_i n_i \tag{3.4}$$

Berger and Hubbell developed XCOM as a tool for calculating the mass attenuation coefficients and photon interaction cross-sections for elements (Z=1-100), compounds or mixtures in the energy range of 1 keV-100 GeV. This program was later enhanced and transferred to the Windows platform and was renamed as WinXCom [60]. The mass attenuation coefficients from different photon interactions are obtained for BR and its comprising amino acids (table 3.1) using WinXCom program. These values are then used to calculate effective atomic number Z_{eff} and effective electron density values N_{el} for energy range of 1 keV-100 GeV.

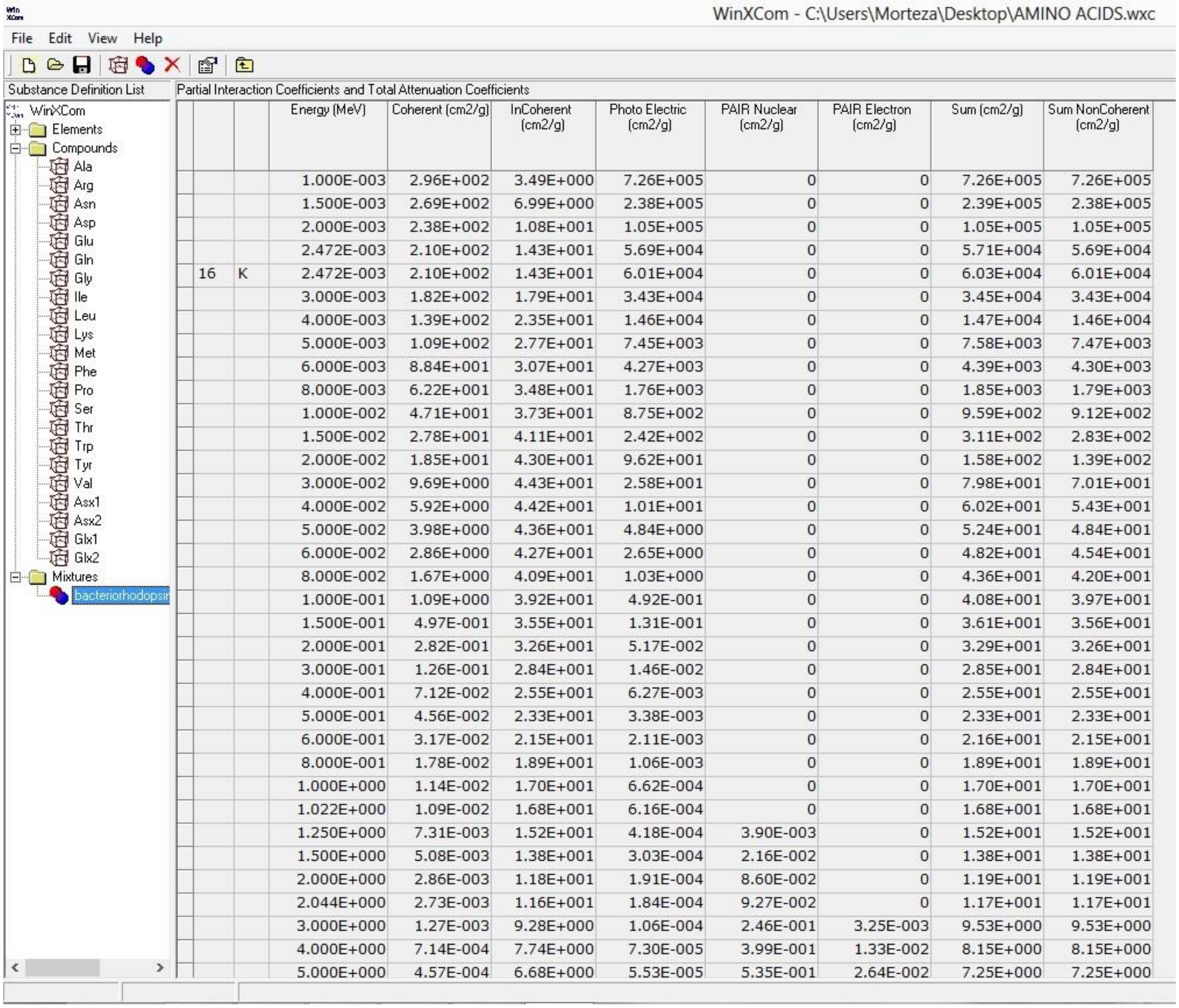

Partial Interaction Coefficients and Total Attenuation Coefficients

		Energy (MeV)	Coherent (cm2/g)	InCoherent (cm2/g)	Photo Electric (cm2/g)	PAIR Nuclear (cm2/g)	PAIR Electron (cm2/g)	Sum (cm2/g)	Sum NonCoherent (cm2/g)
		1.000E-003	2.96E+002	3.49E+000	7.26E+005	0	0	7.26E+005	7.26E+005
		1.500E-003	2.69E+002	6.99E+000	2.38E+005	0	0	2.39E+005	2.38E+005
		2.000E-003	2.38E+002	1.08E+001	1.05E+005	0	0	1.05E+005	1.05E+005
		2.472E-003	2.10E+002	1.43E+001	5.69E+004	0	0	5.71E+004	5.69E+004
16	K	2.472E-003	2.10E+002	1.43E+001	6.01E+004	0	0	6.03E+004	6.01E+004
		3.000E-003	1.82E+002	1.79E+001	3.43E+004	0	0	3.45E+004	3.43E+004
		4.000E-003	1.39E+002	2.35E+001	1.46E+004	0	0	1.47E+004	1.46E+004
		5.000E-003	1.09E+002	2.77E+001	7.45E+003	0	0	7.58E+003	7.47E+003
		6.000E-003	8.84E+001	3.07E+001	4.27E+003	0	0	4.39E+003	4.30E+003
		8.000E-003	6.22E+001	3.48E+001	1.76E+003	0	0	1.85E+003	1.79E+003
		1.000E-002	4.71E+001	3.73E+001	8.75E+002	0	0	9.59E+002	9.12E+002
		1.500E-002	2.78E+001	4.11E+001	2.42E+002	0	0	3.11E+002	2.83E+002
		2.000E-002	1.85E+001	4.30E+001	9.62E+001	0	0	1.58E+002	1.39E+002
		3.000E-002	9.69E+000	4.43E+001	2.58E+001	0	0	7.98E+001	7.01E+001
		4.000E-002	5.92E+000	4.42E+001	1.01E+001	0	0	6.02E+001	5.43E+001
		5.000E-002	3.98E+000	4.36E+001	4.84E+000	0	0	5.24E+001	4.84E+001
		6.000E-002	2.86E+000	4.27E+001	2.65E+000	0	0	4.82E+001	4.54E+001
		8.000E-002	1.67E+000	4.09E+001	1.03E+000	0	0	4.36E+001	4.20E+001
		1.000E-001	1.09E+000	3.92E+001	4.92E-001	0	0	4.08E+001	3.97E+001
		1.500E-001	4.97E-001	3.55E+001	1.31E-001	0	0	3.61E+001	3.56E+001
		2.000E-001	2.82E-001	3.26E+001	5.17E-002	0	0	3.29E+001	3.26E+001
		3.000E-001	1.26E-001	2.84E+001	1.46E-002	0	0	2.85E+001	2.84E+001
		4.000E-001	7.12E-002	2.55E+001	6.27E-003	0	0	2.55E+001	2.55E+001
		5.000E-001	4.56E-002	2.33E+001	3.38E-003	0	0	2.33E+001	2.33E+001
		6.000E-001	3.17E-002	2.15E+001	2.11E-003	0	0	2.16E+001	2.15E+001
		8.000E-001	1.78E-002	1.89E+001	1.06E-003	0	0	1.89E+001	1.89E+001
		1.000E+000	1.14E-002	1.70E+001	6.62E-004	0	0	1.70E+001	1.70E+001
		1.022E+000	1.09E-002	1.68E+001	6.16E-004	0	0	1.68E+001	1.68E+001
		1.250E+000	7.31E-003	1.52E+001	4.18E-004	3.90E-003	0	1.52E+001	1.52E+001
		1.500E+000	5.08E-003	1.38E+001	3.03E-004	2.16E-002	0	1.38E+001	1.38E+001
		2.000E+000	2.86E-003	1.18E+001	1.91E-004	8.60E-002	0	1.19E+001	1.19E+001
		2.044E+000	2.73E-003	1.16E+001	1.84E-004	9.27E-002	0	1.17E+001	1.17E+001
		3.000E+000	1.27E-003	9.28E+000	1.06E-004	2.46E-001	3.25E-003	9.53E+000	9.53E+000
		4.000E+000	7.14E-004	7.74E+000	7.30E-005	3.99E-001	1.33E-002	8.15E+000	8.15E+000
		5.000E+000	4.57E-004	6.68E+000	5.53E-005	5.35E-001	2.64E-002	7.25E+000	7.25E+000

Figure 3.1: Snapshot of WinXCom program.

Table 3.1: Molecular formula of comprising amino acids of bacteriorhodopsin. The amino acids in each of the graphs are referred by their number specified in the table. Bacteriorhodopsin contains an Asx1 or an Asx2 as well as a Glx1 or a Glx2 [62].

Number	Name	Abbreviation	Molecular Formula	Number Present in Bacteriorhodopsin
1	Alanine	Ala	$C_3H_7NO_2$	29
2	Arginine	Arg	$C_6H_{14}N_4O_2$	7
3	Asparagine	Asn	$C_4H_8N_2O_3$	3
4	Aspartic Acid	Asp	$C_4H_7NO_4$	8
5		Asx1	$C_4H_7NO_4$	1
6		Asx2	$C_4H_8N_2O_3$	1
7	Glutamine	Gln	$C_5H_{10}N_2O_3$	3
8	Glutamic Acid	Glu	$C_5H_9NO_4$	9
9		Glx1	$C_5H_{10}N_2O_3$	1
10		Glx2	$C_5H_9NO_4$	1
11	Glycine	Gly	$C_2H_5NO_2$	25
12	Isoleucine	Ile	$C_6H_{13}NO_2$	16
13	Leucine	Leu	$C_6H_{13}NO_2$	36
14	Lysine	Lys	$C_6H_{14}N_2O_2$	7
15	Methionine	Met	$C_5H_{11}NO_2S$	8
16	Phenylalanine	Phe	$C_9H_{11}NO_2$	13
17	Proline	Pro	$C_5H_9NO_2$	11
18	Serine	Ser	$C_3H_7NO_3$	13
19	Threonine	Thr	$C_4H_9NO_3$	18
20	Tryptophan	Trp	$C_{11}H_{12}N_2O_2$	8
21	Tyrosine	Try	$C_9H_{11}NO_3$	11
22	Valine	Val	$C_5H_{11}NO_2$	21

3.3 Results and Discussion

3.3.1 Mass attenuation coefficients

The dependence of mass attenuation coefficient μ/ρ of BR and its amino acids to photon energy is shown in Figure **3.2**. There are two points at which the slope of the total interctions with the coherent plot is significantly changed. Those points define three ranges of energies related to dominant X-ray interactions: photoelectric absorption, incoherent (Compton) scattering and pair production. This trend matches previous reports [57], [58]. Also, except between 100 keV-10 MeV, the mass attenuation coefficient shows variation with chemical composition of amino acids. This is due to the dependence of X-ray-matter interaction cross-sections to atomic number of the target material. Interaction cross-section is an indicator of the likelihood of interaction of the incident photons with the target atom. Interaction cross-section is proportional to Z for incoherent scattering, Z^2 for pair production, Z^2 or Z^3 (depending on the energy) for coherent scattering and Z^4 or Z^5 (depending on the energy) for photoelectric absorption.

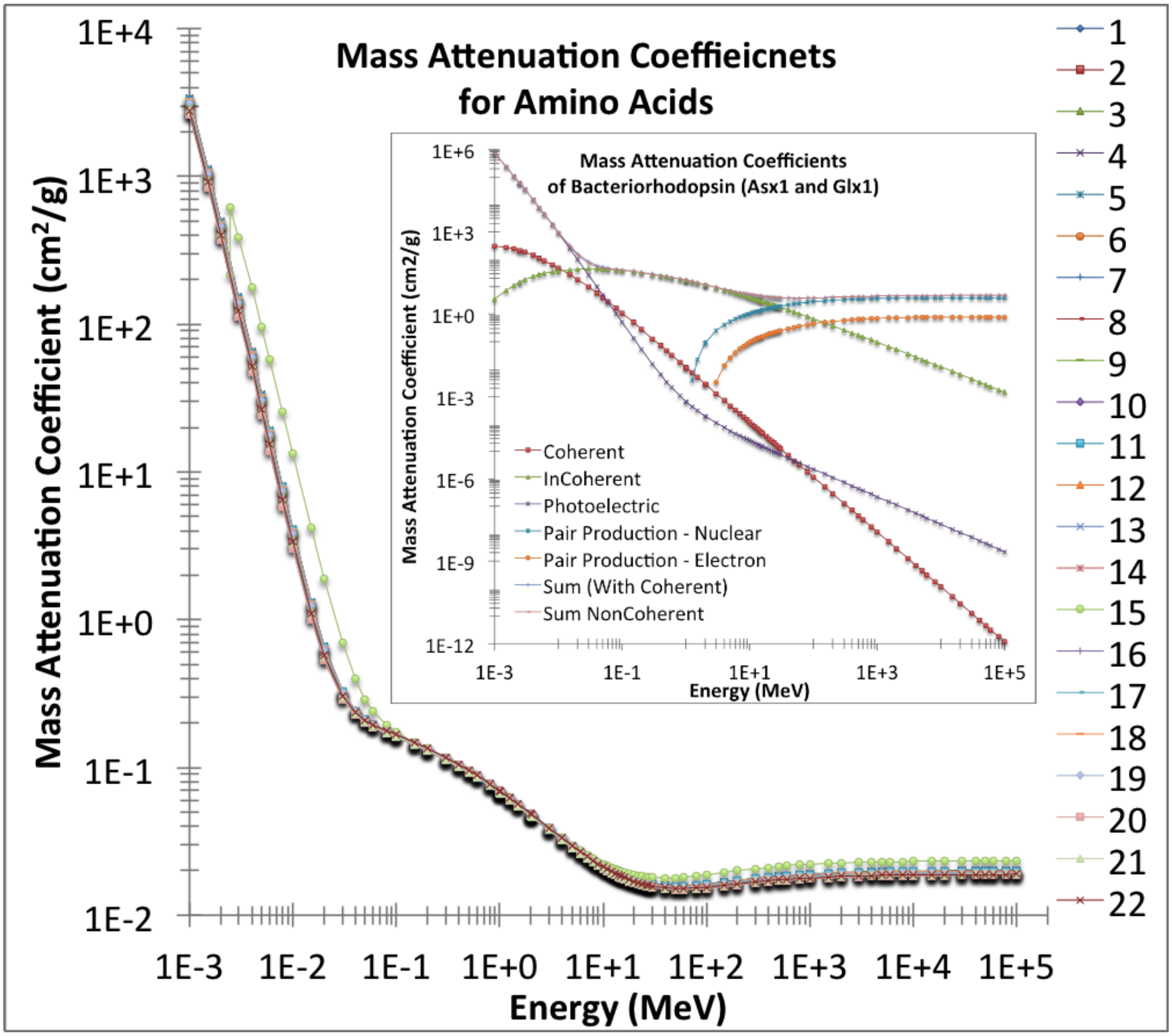

Figure 3.2: Mass attenuation coefficients of amino acids of bacteriorhodopsin. Inset shows the mass attenuation coefficient of bacteriorhodopsin for different interactions.

3.3.2 Effective atomic number

The effective atomic numbers for different photon interactions at varying photon energies are shown for BR in Figure **3.3**. In the total interactions (with coherent), there are three areas where variation of Z_{eff} against photon energy is minimal. These areas are 1-10 keV, 0.1-10 MeV and above 100 MeV.

For photoelectric effect, the $\mathrm{Z_{eff}}$ varies between 6.9 and 8.1. For coherent scattering, the Z_{eff} of BR increases until about 800 keV, then becomes largely independent of photon energies. For incoherent scattering, Z_{eff} of BR increases quickly until about 400 keV after which it is largely constant and independent of photon energy. The values of Z_{eff} are within 6.05-6.85 and 2.5 - 3.7 for coherent and incoherent scattering, respectively.

Pair production (electric field) does not occur until after ~2 MeV. Z_{eff} is independent of energy until about 10 MeV where the Z_{eff} begins to decrease. Pair production in the nuclear field does not occur until after 1 MeV. The Z_{eff} gradually decreases as the photon energy increases until about 10 GeV where it becomes almost constant. It is worth mentioning that the effective atomic numbers can be also calculated in an easier way using a new software called Auto-$\mathrm{Z_{eff}}$ [63].

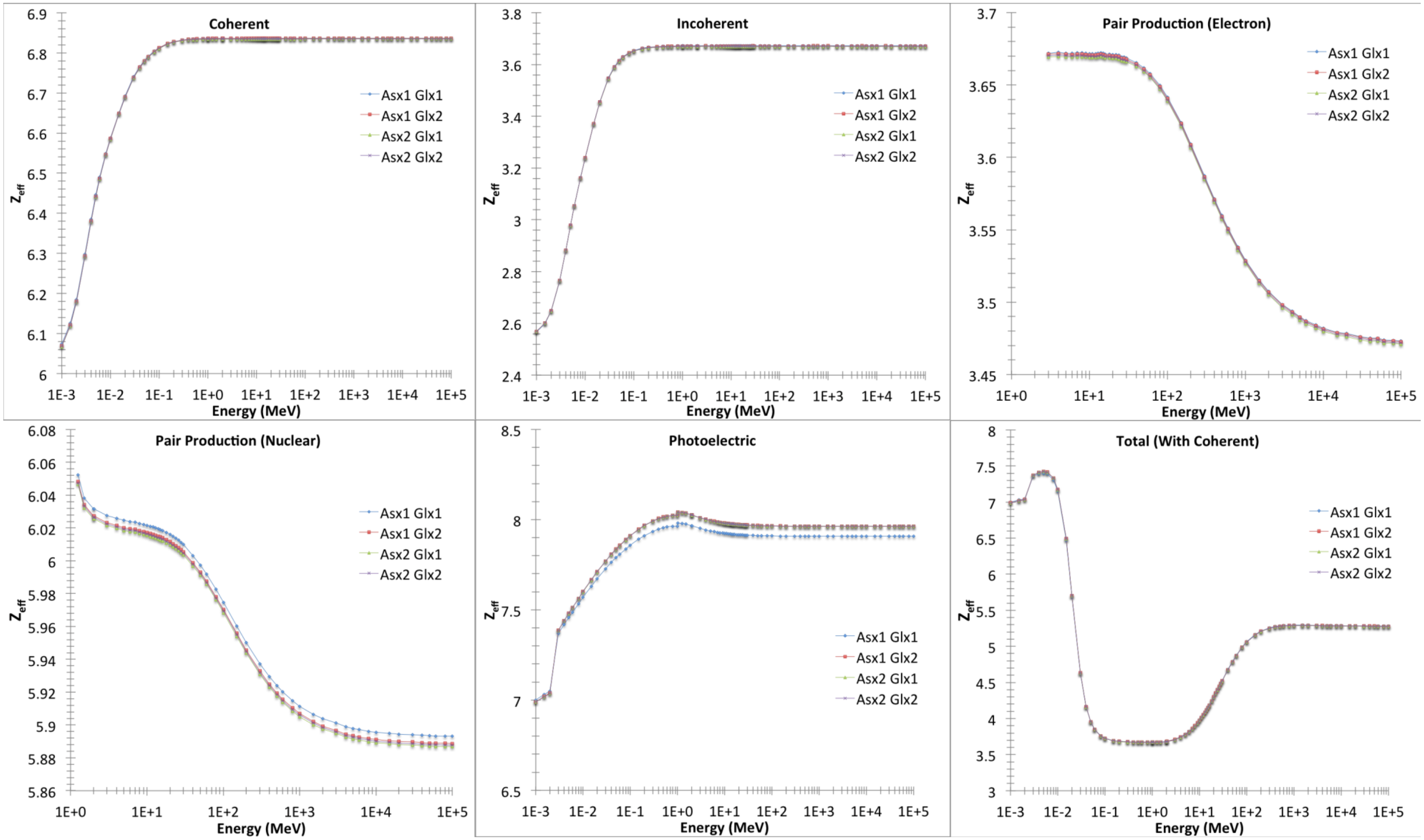

Figure 3.3: Effective atomic number of bacteriorhodopsin for partial and total interactions.

3.3.3 Effective electron density

Effective electron density N_{el} of BR and its comprising amino acids shows the same trend as effective atomic number against energy of photons. This trend is observed not only in partial interactions but also in total interaction processes.

3.4 Radiation oncology applications

The BR radiation sensor is designed to be tested using a superficial X-ray machine (Gulmay Medical D3000 DXR, Gulmay Ltd., Chertsey, UK) and a linear accelerator (Varian CLINAC 21 EX, Varian Medical Systems, Inc.). As such, we emphasize on the mass attenuation coefficients, Z_{eff} and N_{el} values of BR for 10-200 keV and 1-20 MeV photons. The calculated results are shown in Appendix. Also, Z_{eff} and N_{el} of comprising amino acids of BR are given in tables 3.2-3.5. The above radiation sources have a continuous spectrum of energies. Thus, for practical applications, Z_{eff} has to be spectral-weighted [63]. The dominant interaction of X-ray and target depends on the energy of the beam and the atomic number of the target. The comprising chemical elements of amino acids in BR have low atomic numbers. The dominant interaction of X-ray photons with BR under superficial X-ray beam (100-150 kV tube potential) is photoelectric effect, while Compton scattering is dominant for BR-photon interaction under Linear Accelerator X-ray beam (6-15 MV X-ray beam).

Table 3.2: Effective atomic numbers of amino acids for total photon interactions (with coherent) at photon energies 10-200 keV.

Energy (keV)	1	2	3	4	5	6	7	8	9	10	11	12	13	14	15	16	17	18	19	20	21	22
10	6.86	6.58	6.97	7.16	7.16	6.97	6.86	7.04	6.86	7.04	7.06	6.46	6.46	6.49	12.49	6.43	6.64	7.09	6.94	6.41	6.64	6.57
20	5.51	5.25	5.86	6.14	6.14	5.86	5.64	5.89	5.64	5.89	5.86	4.92	4.92	4.99	10.58	5.26	5.31	5.88	5.61	5.36	5.52	5.07
30	4.55	4.37	4.98	5.28	5.28	4.98	4.73	4.99	4.73	4.99	4.92	4.00	4.00	4.07	8.03	4.49	4.42	4.93	4.65	4.63	4.72	4.13
40	4.13	4.00	4.57	4.85	4.85	4.57	4.33	4.57	4.33	4.57	4.48	3.64	3.64	3.70	6.33	4.16	4.04	4.48	4.22	4.33	4.37	3.75
50	3.95	3.84	4.38	4.65	4.65	4.38	4.15	4.37	4.15	4.37	4.28	3.48	3.48	3.55	5.40	4.02	3.87	4.28	4.03	4.19	4.22	3.59
60	3.85	3.76	4.28	4.55	4.55	4.28	4.06	4.28	4.06	4.28	4.18	3.41	3.41	3.47	4.90	3.95	3.79	4.18	3.93	4.12	4.14	3.51
80	3.77	3.69	4.20	4.47	4.47	4.20	3.98	4.19	3.98	4.19	4.09	3.34	3.34	3.40	4.43	3.89	3.72	4.09	3.85	4.06	4.07	3.44
100	3.74	3.66	4.17	4.43	4.43	4.17	3.95	4.16	3.95	4.16	4.05	3.31	3.31	3.37	4.24	3.86	3.69	4.05	3.82	4.04	4.04	3.41
150	3.71	3.63	4.14	4.40	4.40	4.14	3.92	4.13	3.92	4.13	4.02	3.29	3.29	3.35	4.09	3.84	3.67	4.02	3.79	4.02	4.02	3.39
200	3.70	3.63	4.13	4.39	4.39	4.13	3.91	4.12	3.91	4.12	4.01	3.28	3.28	3.34	4.05	3.84	3.66	4.01	3.78	4.01	4.01	3.38

Table 3.3: Effective atomic numbers of amino acids for total photon interactions (with coherent) at photon energies 1-20 MeV.

Energy (MeV)	1	2	3	4	5	6	7	8	9	10	11	12	13	14	15	16	17	18	19	20	21	22
1	3.69	3.62	4.12	4.38	4.38	4.12	3.90	4.11	3.90	4.11	4.00	3.27	3.27	3.33	4.00	3.83	3.65	4.00	3.77	4.00	4.00	3.37
2	3.70	3.63	4.13	4.39	4.39	4.13	3.91	4.12	3.91	4.12	4.01	3.28	3.28	3.34	4.02	3.84	3.66	4.01	3.78	4.01	4.01	3.38
3	3.73	3.65	4.16	4.42	4.42	4.16	3.94	4.15	3.94	4.15	4.04	3.31	3.31	3.37	4.07	3.86	3.68	4.04	3.80	4.03	4.04	3.40
4	3.77	3.68	4.19	4.45	4.45	4.19	3.97	4.18	3.97	4.18	4.08	3.34	3.34	3.40	4.13	3.89	3.72	4.08	3.84	4.06	4.07	3.44
5	3.80	3.72	4.23	4.49	4.49	4.23	4.01	4.22	4.01	4.22	4.12	3.37	3.37	3.43	4.19	3.92	3.75	4.12	3.88	4.09	4.10	3.47
6	3.84	3.76	4.27	4.53	4.53	4.27	4.05	4.26	4.05	4.26	4.16	3.41	3.41	3.47	4.26	3.96	3.79	4.16	3.92	4.13	4.14	3.51
7	3.88	3.80	4.31	4.58	4.58	4.31	4.09	4.30	4.09	4.30	4.20	3.44	3.44	3.51	4.33	3.99	3.83	4.20	3.96	4.16	4.17	3.54
8	3.93	3.83	4.35	4.62	4.62	4.35	4.13	4.34	4.13	4.34	4.25	3.48	3.48	3.54	4.40	4.03	3.86	4.25	4.00	4.20	4.21	3.58
9	3.97	3.87	4.39	4.66	4.66	4.39	4.17	4.38	4.17	4.38	4.29	3.52	3.52	3.58	4.46	4.06	3.90	4.29	4.04	4.23	4.25	3.62
10	4.00	3.91	4.43	4.70	4.70	4.43	4.21	4.42	4.21	4.42	4.33	3.55	3.55	3.62	4.53	4.09	3.94	4.33	4.08	4.26	4.28	3.66
11	4.04	3.94	4.47	4.74	4.74	4.47	4.25	4.46	4.25	4.46	4.37	3.59	3.59	3.65	4.59	4.13	3.97	4.37	4.12	4.29	4.31	3.69
12	4.08	3.98	4.51	4.77	4.77	4.51	4.28	4.50	4.28	4.50	4.41	3.62	3.62	3.69	4.65	4.16	4.01	4.41	4.16	4.32	4.35	3.73
13	4.12	4.01	4.54	4.81	4.81	4.54	4.32	4.54	4.32	4.54	4.44	3.65	3.65	3.72	4.71	4.19	4.04	4.45	4.19	4.35	4.38	3.76
14	4.15	4.04	4.58	4.84	4.84	4.58	4.35	4.57	4.35	4.57	4.48	3.68	3.68	3.75	4.77	4.22	4.08	4.48	4.23	4.38	4.41	3.79
15	4.18	4.08	4.61	4.88	4.88	4.61	4.38	4.60	4.38	4.60	4.51	3.71	3.71	3.78	4.83	4.25	4.11	4.52	4.26	4.41	4.44	3.82
16	4.22	4.11	4.64	4.91	4.91	4.64	4.42	4.63	4.42	4.63	4.55	3.74	3.74	3.81	4.88	4.28	4.14	4.55	4.30	4.44	4.47	3.85
18	4.28	4.16	4.70	4.97	4.97	4.70	4.47	4.69	4.47	4.69	4.61	3.80	3.80	3.87	4.98	4.33	4.19	4.61	4.36	4.49	4.52	3.91
20	4.33	4.22	4.76	5.02	5.02	4.76	4.53	4.75	4.53	4.75	4.67	3.85	3.85	3.92	5.07	4.37	4.25	4.67	4.42	4.53	4.57	3.97

Table 3.4: Effective electron densities $\boldsymbol{N_{el}}$ x10^{23} (electrons/g) of amino acids for total photon interactions (with coherent) at photon energies 10-200 keV.

Energy (keV)	1	2	3	4	5	6	7	8	9	10	11	12	13	14	15	16	17	18	19	20	21	22
10	6.03	5.91	5.40	5.18	5.18	5.40	5.65	5.47	5.65	5.47	5.67	6.53	6.53	6.42	10.08	5.39	5.91	5.68	5.96	5.11	5.30	6.42
20	4.84	4.72	4.54	4.45	4.45	4.54	4.64	4.58	4.64	4.58	4.70	4.97	4.97	4.93	8.54	4.41	4.72	4.72	4.83	4.26	4.40	4.95
30	4.00	3.93	3.86	3.82	3.82	3.86	3.90	3.88	3.90	3.88	3.94	4.04	4.04	4.02	6.48	3.76	3.93	3.95	3.99	3.69	3.77	4.04
40	3.63	3.59	3.54	3.51	3.51	3.54	3.57	3.55	3.57	3.55	3.59	3.67	3.67	3.66	5.11	3.49	3.59	3.60	3.63	3.44	3.49	3.66
50	3.47	3.45	3.39	3.37	3.37	3.39	3.42	3.40	3.42	3.40	3.43	3.52	3.52	3.51	4.36	3.37	3.44	3.43	3.46	3.33	3.36	3.51
60	3.39	3.38	3.32	3.30	3.30	3.32	3.35	3.33	3.35	3.33	3.35	3.44	3.44	3.43	3.95	3.31	3.37	3.35	3.38	3.28	3.30	3.43
80	3.32	3.31	3.26	3.23	3.23	3.26	3.28	3.26	3.28	3.26	3.28	3.37	3.37	3.36	3.58	3.26	3.31	3.28	3.31	3.23	3.25	3.36
100	3.29	3.29	3.23	3.21	3.21	3.23	3.25	3.23	3.25	3.23	3.25	3.35	3.35	3.34	3.43	3.24	3.28	3.25	3.28	3.21	3.22	3.33
150	3.26	3.27	3.21	3.18	3.18	3.21	3.23	3.21	3.23	3.21	3.23	3.32	3.32	3.31	3.30	3.22	3.26	3.23	3.25	3.20	3.20	3.31
200	3.25	3.26	3.20	3.18	3.18	3.20	3.22	3.20	3.22	3.20	3.22	3.32	3.32	3.31	3.27	3.22	3.25	3.22	3.25	3.19	3.20	3.30

Table 3.5: Effective electron densities $\boldsymbol{N_{el}}$ x10^{23} (electrons/g) of amino acids for total photon interactions (with coherent) at photon energies 1-20 MeV.

Energy (MeV)	1	2	3	4	5	6	7	8	9	10	11	12	13	14	15	16	17	18	19	20	21	22
1	3.25	3.25	3.19	3.17	3.17	3.19	3.21	3.19	3.21	3.19	3.21	3.31	3.31	3.30	3.23	3.21	3.24	3.21	3.24	3.19	3.19	3.29
2	3.25	3.26	3.20	3.18	3.18	3.20	3.22	3.20	3.22	3.20	3.22	3.32	3.32	3.31	3.24	3.22	3.25	3.22	3.25	3.19	3.20	3.30
3	3.28	3.28	3.22	3.20	3.20	3.22	3.25	3.22	3.25	3.22	3.24	3.34	3.34	3.33	3.28	3.24	3.28	3.24	3.27	3.21	3.22	3.32
4	3.31	3.31	3.25	3.22	3.22	3.25	3.27	3.25	3.27	3.25	3.27	3.37	3.37	3.36	3.33	3.26	3.30	3.27	3.30	3.23	3.24	3.36
5	3.34	3.34	3.28	3.25	3.25	3.28	3.31	3.28	3.31	3.28	3.30	3.40	3.40	3.39	3.38	3.29	3.34	3.30	3.33	3.26	3.27	3.39
6	3.38	3.38	3.31	3.28	3.28	3.31	3.34	3.31	3.34	3.31	3.34	3.44	3.44	3.43	3.44	3.32	3.37	3.34	3.37	3.29	3.30	3.43
7	3.41	3.41	3.34	3.31	3.31	3.34	3.37	3.35	3.37	3.35	3.37	3.48	3.48	3.47	3.49	3.35	3.40	3.37	3.40	3.31	3.33	3.46
8	3.45	3.45	3.37	3.34	3.34	3.37	3.40	3.38	3.40	3.38	3.41	3.51	3.51	3.50	3.55	3.38	3.44	3.41	3.44	3.34	3.36	3.50
9	3.48	3.48	3.40	3.37	3.37	3.40	3.44	3.41	3.44	3.41	3.44	3.55	3.55	3.54	3.60	3.41	3.47	3.44	3.47	3.37	3.39	3.53
10	3.52	3.51	3.44	3.40	3.40	3.44	3.47	3.44	3.47	3.44	3.47	3.59	3.59	3.58	3.66	3.43	3.50	3.47	3.51	3.39	3.41	3.57
11	3.55	3.54	3.46	3.43	3.43	3.46	3.50	3.47	3.50	3.47	3.50	3.62	3.62	3.61	3.71	3.46	3.53	3.51	3.54	3.42	3.44	3.61
12	3.59	3.58	3.49	3.46	3.46	3.49	3.53	3.50	3.53	3.50	3.54	3.66	3.66	3.64	3.76	3.49	3.56	3.54	3.57	3.44	3.47	3.64
13	3.62	3.61	3.52	3.48	3.48	3.52	3.56	3.53	3.56	3.53	3.57	3.69	3.69	3.68	3.81	3.51	3.59	3.57	3.61	3.47	3.49	3.67
14	3.65	3.64	3.55	3.51	3.51	3.55	3.59	3.55	3.59	3.55	3.59	3.72	3.72	3.71	3.85	3.54	3.62	3.60	3.64	3.49	3.52	3.70
15	3.68	3.66	3.57	3.53	3.53	3.57	3.61	3.58	3.61	3.58	3.62	3.75	3.75	3.74	3.90	3.56	3.65	3.62	3.66	3.51	3.54	3.73
16	3.70	3.69	3.60	3.55	3.55	3.60	3.64	3.60	3.64	3.60	3.65	3.78	3.78	3.77	3.94	3.58	3.68	3.65	3.69	3.53	3.56	3.76
18	3.76	3.74	3.64	3.60	3.60	3.64	3.69	3.65	3.69	3.65	3.70	3.84	3.84	3.83	4.02	3.63	3.73	3.70	3.75	3.57	3.61	3.82
20	3.81	3.79	3.68	3.64	3.64	3.68	3.73	3.69	3.73	3.69	3.74	3.89	3.89	3.88	4.09	3.67	3.78	3.75	3.79	3.61	3.64	3.87

.

3.5 Discussion

Electrical conductivity originates from transport of charged particles inside a medium and under the influence of an electric field. Electrical conductivity of BR is very close to that of insulators [47]. According to the model of radiation induced conductivity in insulators, the electrical conductivity of the irradiated insulator (i.e. BR) is increased under X-ray radiation [64]. Also, in this model the time dependent density of free electrons in an irradiated insulator is proportional to its electrical conductivity and depends on radiation energy [65]. Therefore, the density of free electrons in the insulator is increased under radiation and the electrical conductivity under radiation depends on the energy of the beam. Radiation induced current is a direct result of radiation induced conductivity.

Chapter 4

Use of bacteriorhodopsin as an X-ray sensor

4.1 Megavoltage (MeV) X-rays beam energy range

The BR sensor with PET-ITO-(BR, Kapton)-ITO-PET layers was tested under Varian linear accelerator for its response to megavoltage X-rays. The results of characterization are presented in this chapter.

4.1.1 Linear accelerator

Experiments are performed using Varian CLINAC 21 EX linear accelerators (Varian Medical Systems, Inc.) at Grand River Regional Cancer Centre, Kitchener, Ontario. The X-ray generator is capable of producing 6MV and 15MV X-ray beam at different dose rates of 100–600 MU/min. The X-ray beam source can be positioned at different gantry angles and distances from the target, and is capable of providing various beam shapes. In this study, we keep 1m distance between the source and target and the gantry is set to zero (i.e. beam is vertical to the sensor surface). We also use square field shape only.

4.1.2 Measurement set up for experiments with LINAC

Each sensor is placed on a 10 cm block of water phantom which is intended to represent the target. The sensor is positioned such that it is at the center of an X-ray beam with a square shaped field of (i) 10cm×10cm for different dose rates, (ii) 7.5cm×7.5cm for repeatability test, (iii) 3 cm×3cm, 6cm×6 cm, 9 cm×9 cm, 12cm×12cm and 15cm×15cm for current measurement versus different field sizes. The electrodes are directly connected to an Agilent 3458A multimeter (Agilent Technologies, Inc.). This multimeter is able to measure nanoampere electrical current. The multimeter is controlled by a program written in Matlab on a computer. The program continuously records the real time nanoampere current with the sampling rate of 5 Hz. No external bias voltage was applied in the measurement. The multimeter measures current by placing an internal shunt resistor of 545.2 kΩ across the input terminals, measuring the voltage across the resistor and calculating the current by dividing voltage by resistance. The calibration of the linear accelerator is traceable to an accredited national dosimetry laboratory (NRC, Ottawa, Canada).

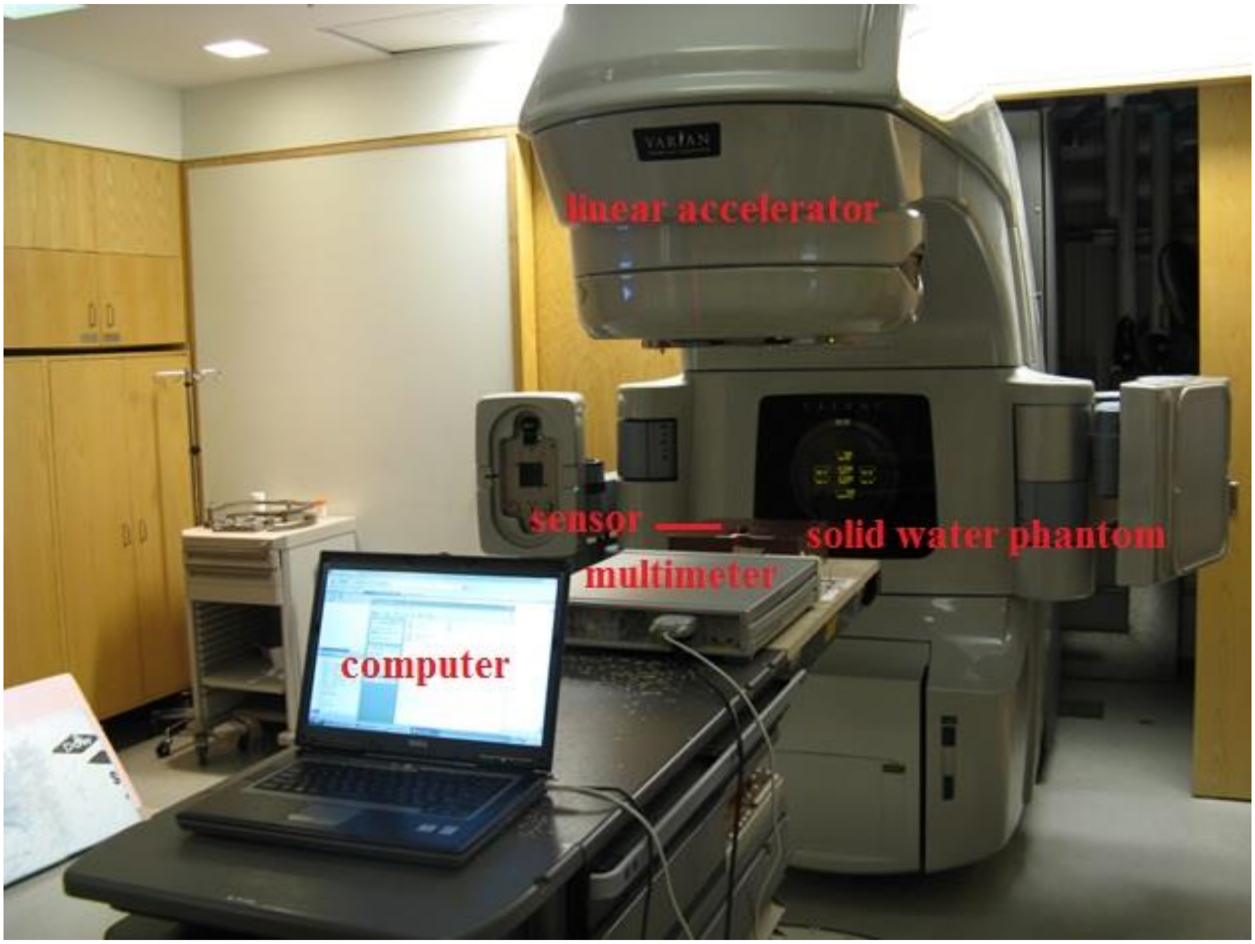

Figure 4.1 Varian linear accelerator in Grand River Cancer Centre, Kitchener, Ontario. This machine has been used as an X-ray source for characterization of the fabricated sensors.

4.1.3 Variation with dose rate and beam energy

Figure **4.2** illustrates the response of the fabricated radiation sensor to different radiation dose rates. The sensor is irradiated by 6 MV X-ray radiation for dose rates of 100–600 MU/min for 12 s.

The recorded change in the electrical current shows a steep rise and a fall followed by a plateau. Such response is independent of the amount of dose rate and the energy of the X-ray radiation. This is clear in Figure **4.3** for the radiation energy of 15MVas well. Increasing the dose rate causes an increase in the generated electrical current. After the X-ray beam is turned off the current also drops to its initial value such that no residual current in addition to the initial current is observed. In Figure **4.3**, it is observed that an increase in the energy of the radiation from 6 MV to 15 MV enhances the produced current. Such increase is amplified at higher dose rates. The response of the sensor is also compared to a control sensor which does not have the BR coating. The induced electrical current generated by the BR molecules under X-ray radiation is calculated by subtracting the response of the control sample from the sensor with BR coating. Table **4.1** presents the averaged induced current generated by unit area of BR molecules under 6 MV and 15 MV X-ray radiations. Such information can be very useful in designing radiation sensors based on BR coated on a different substrate.

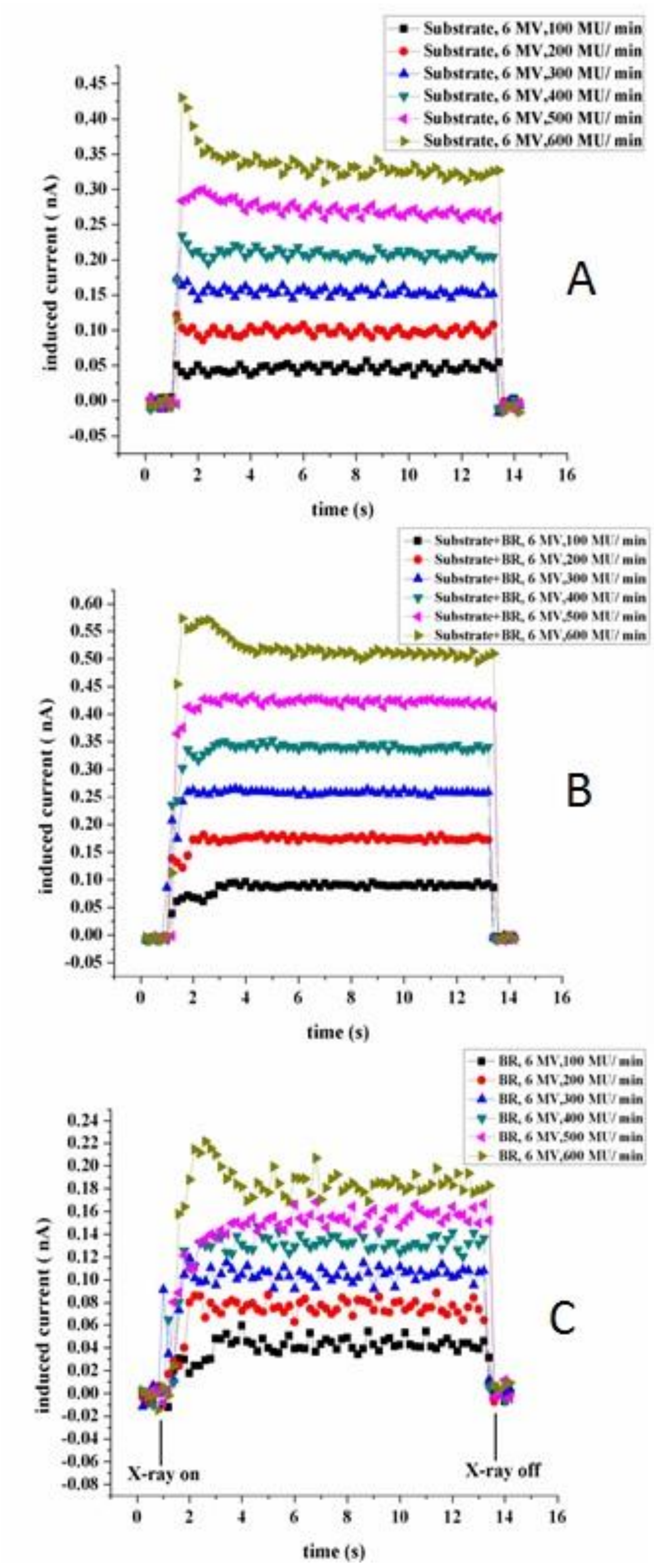

Figure 4.2: Electrical current induced in the flexible BR sensor under 0.2 minute of 6 MV X-ray radiation. Different dose rates are applied (100 MU/min – 600 MU/min) and the field size is 10 cm × 10 cm. (A): Response of the control sample (substrate only). (B): The sensor (substrate + BR) shows an up and down in the beginning and then the current becomes stable. (C): The current generated by BR molecules only.

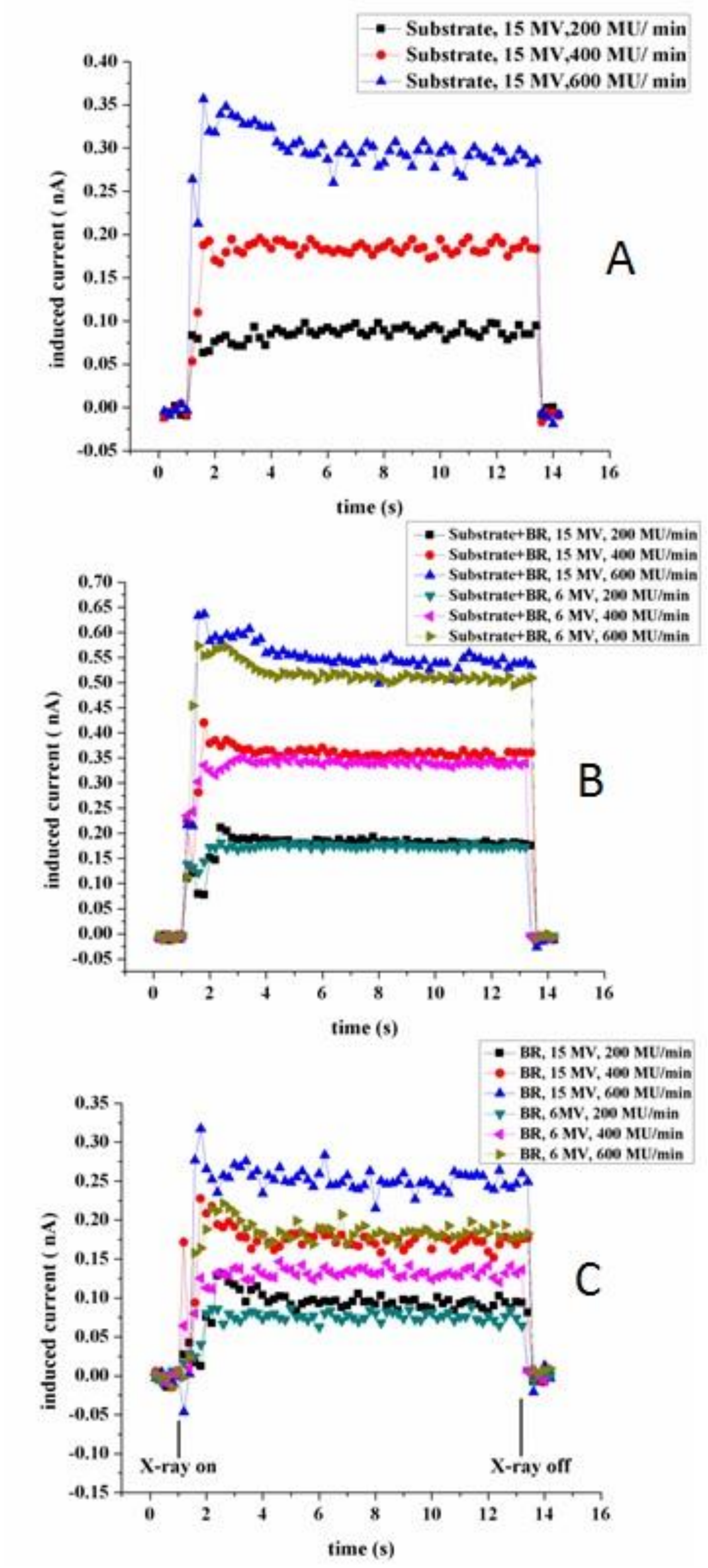

Figure 4.3: Increasing the energy from 6 MV to 15 MV causes a rise in the induced current for different dose rates. (A): control sample (substrate); (B): sensor (substrate + BR); (C): BR only. (field size = 10 cm × 10 cm).

Table 4.1: Averaged radiation induced current per area generated from BR molecules only.

Dose Rate (MU/min)	**Induced current (nA/cm^2)**	
	6 MV	*15 MV*
100	0.14649	0.28434
200	0.26170	0.59558
300	0.35761	0.92012
400	0.45230	1.20156
500	0.52597	1.49167
600	0.64694	1.88327

4.1.4 Variation with field size

To test the effect of radiation field size on the induced current, the radiation sensor was irradiated by X-ray under constant energy (15 MV), dose (100 MU) and dose rate (600 MU/min) but with different field sizes. The result is presented in Figure **4.4**. An increase in the magnitude of the induced current is observed with the increase of the X-ray field size. In the initial response of the sensor, there is a rise and fall before the plateau which is clearer when the size of the X-ray field is much larger than the area of the sensor (3 cm×3 cm). This can be attributed to the scattering electrons that are released by the background materials.

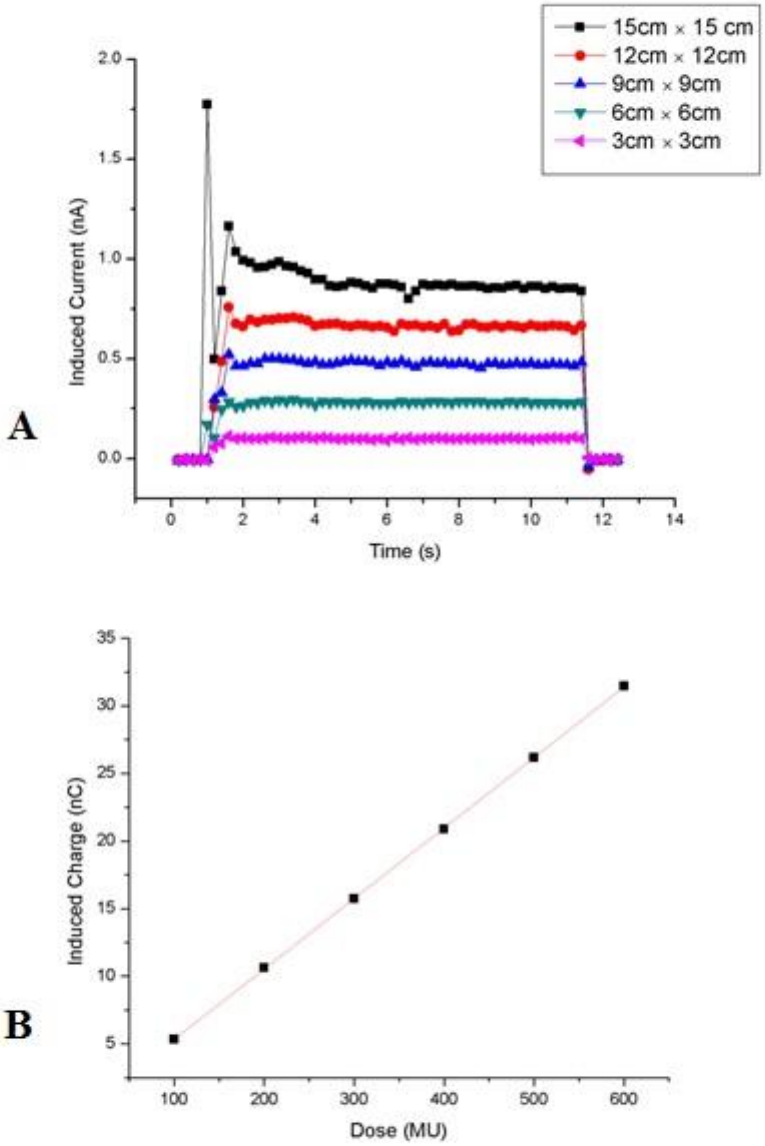

Figure 4.4:(A): Effect of choosing different X-ray radiation field sizes on the induced current. The sensor (substrate + BR) is irradiated with 100 MU of 15 MV X-ray radiation and under the dose rate of 600 MU/min. (B) The sensor (substrate + BR) is irradiated with different doses of 6 MV X-ray radiation (100 MU-600 MU) under constant dose rate of 600 MU/min. The radiation induced charge

is calculated by integrating the current over radiation time. Sensor shows an excellent linear response to the dose increase (field size = 10 cm × 10 cm).

4.1.5 Variation with absorbed dose

It is also possible to use the sensor to make measurements based on electric charge instead of electric current. Different radiation doses using 6 MV X-ray beam are delivered at a dose rate of 600 MU/min. The collected current (i) was integrated over radiation time to calculate the induced electric charge (C), C = $\int i \, dt$. The result illustrates an excellent linear response for radiation doses of 100–600 MU (Figure **4.4**). The radiation induced charge is increased with an increase of the radiation dosage. The best-fit line which includes all data points is as follows, $C = 0.05216\, D + 0.10886$ where C is the electric charge in nanoCoulomb (nC) and D represents radiation dose in monitor unit (MU).

4.1.6 Repeatability test

The response of a radiation sensor has to be repeatable under the same experiment conditions. The radiation sensor is irradiated using 15 MV X-ray beam (600 MU/min) for 2 s followed by 2 s of relaxation time and this process is repeated 6 times (Figure **4.5**). The radiation field size is 7.5 cm × 7.5 cm. The initial response of BR is a steep rise and fall which tends to turn into a plateau quickly. The average electric current measured is 0.35 nA and the relative standard deviation is 0.90%. The results given in Figure **4.5** is taken by one sensor only.

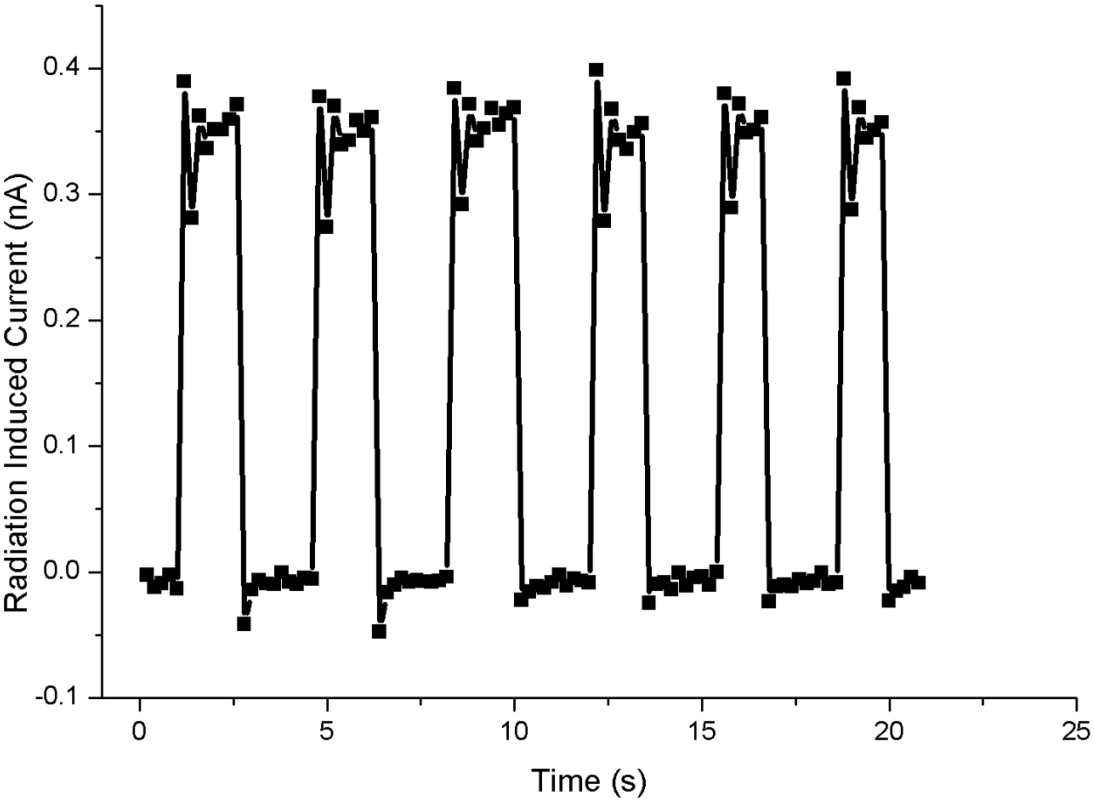

Figure 4.5: Repeatability test result of real time current induced in the BR sensor (substrate + BR) under 15 MV X-ray radiation with dose rate of 600 MU/min (field size = 7.5 cm × 7.5 cm).

4.1.7 Sensing mechanism

X-ray interacts with matter through different ways such as photoelectric absorption, elastic and inelastic Compton scattering, and pair production. These interactions produce different types of electrons such as photoelectrons, Auger electrons, Compton recoil electrons as well as fluorescent, coherent or Compton X-ray secondary photons. The dominant interaction and the result of the interaction highly depend on the energy of the interacting X-ray beam and the composition of the target. BR consists of 248 amino acids in the form of seven α-helical bundles inside the lipid membrane [28]. Amino acids contain mostly elements with low atomic numbers (Z) such as C (Z = 6), H (Z = 1), N (Z=7) and O (Z = 8). In the interaction of few MV X-ray radiations with low-Z materials, the dominant interaction mechanism is Compton scattering. The released Compton electron can be collected by electrodes.

There are evidences that BR disks have an unusual large permanent electric dipole moment perpendicular to the surface [66], [67] . The permanent dipole moment is 4×10^{6} D for membrane fragments of 1 μm diameter and it increases with the area of the membrane disk [67]. The direction of the dipole moment is also the same as the proton pumping direction, i.e. from inside to outside of the cell [68]. The proton pumping process in BR is related with diffusion phenomenon, however long range electrostatic interactions between the dipole moment and the released protons may help the process [67]. Although these results are for BR fragments in suspension, they might be also valid for dry BR film as BR molecules keep their electrical properties even in the dry form [69], [70]. We therefore hypothesize that the permanent dipole moment of BR might be also a driving force for the positive ions and electrons released from the BR molecules under irradiation. It also might have a long range effect on the freed charges at the ITO-BR interface.

4.1.8 Discussion

The total radiation detected by a radiation sensor is comprised of two parts: primary radiation and scatter radiation [71]. The primary dose originates from those photons that the sensor is the first material they are interacting with after being generated in the source. When primary photons hit other materials, scattered radiations are produced which is the source of scatter radiation. Radiations with large field sizes generate more scatter in comparison with the smaller fields due to the increased chance of interaction of photons with the medium between the source and the target. This may explain what is observed in 15cm×15cm field size in Figure **4.4** (A) as an initial uprise and drop.

Another phenomenon which occurs under irradiation is the radiation induced conductivity. Some examples in which this phenomenon has been observed include purple membrane and BR aqueous suspensions irradiated with photons of 577 nm wavelength [72], [73] and dry thin film of biological macromolecules (i.e. DNA) irradiated by X-ray [74]. Such effect has been also used to explain the response of other X-ray sensors like diamond dosimeters [75], [76] and carbon fiber radiation sensor [77]. X-ray absorption studies on BR and purple membrane have shown absorption spectrum over a wide range of X-ray energies [78], [79] . When the BR disk is irradiated by MV X-ray radiation, the absorption of the ionizing radiation causes a temporary change in the electrical conductivity of the BR thin film through the production of positive ions and electrons. The movement of the produced charged particles is affected by the current already in the circuit and produced charges with opposite poles move in opposite directions. Such movement reinforces the initial current. As a result, the electrical current passing through the BR disk increases under the X-ray radiation and returns to the initial value when the beams are off. The dose rate and therefore the intensity of the X-ray radiation determine the number of photons per second shined on the BR disk. This defines the number of produced charges in the BR disk which also specifies the change in the current.

A disk of r = 3 mm of dry BR on a 3cm×3cm square of ITO coated PET substrate is able to produce a measurable radiation induced current signal which is distinguishable from the signal of the control substrate. Therefore, utilizing a smaller substrate while keeping the BR coated area unchanged may significantly increase the signal to noise ratio. The best case is expected to be the one in which BR is coated all over the substrate. Ideally, the substrate can be as small as a BR molecule. This suggests the possibility of integrating an array of micro-scale radiation sensors based on BR. BR molecules proved to be highly sensitive to X-ray radiations. Comparing with other radiation dosimeters, BR sensor does not require a bias voltage for operation and provides real-time dose and dose rate information. BR sensor is also easy to operate and the measurements show low noise at room temperature. The stability of dry BR film in high temperature is well-suited for patterning micrometer and possibly nanometer scale designs on a wide range of substrates. BR can be sandwiched between two layers and can be totally isolated from the environment around. As such, the sensor can be made compatible to chemically harsh environments. The possibility of making BR sensors out of flexible substrates opens up opportunities for radiation monitoring applications on curved surfaces. BR is a commercially available biomaterial. Mass production of the BR radiation sensor is possible due to the simplicity of the deposition and fabrication process.

4.2 Kilovoltage (keV) X-rays beam energy range

There are several applications of kilovoltage X-rays in radiation therapy including the treatment of basal or squamous cell carcinomas of the skin and the palliative irradiation of bone metastases [80]. A very good quality assurance of radiation therapy of patients should include patient-specific in vivo dosimetry, whereby the radiation dose delivered to the patient is measured during the treatment. Recent radiation therapy incidents involving high dose delivery to patients in the UK [81] has also demanded the use of in vivo patient dosimeters to measure the radiation dose delivered for those treatments where an independent check of dose cannot be carried out by other means. The use of some current technology for in vivo patient dosimetry is either cumbersome or inadequate. For example, Metal-oxide-semiconductor field effect transistor (MOSFET) dosimeters have short life time, ionization chambers are not miniaturizable and thermoluminescence dosimeters (TLDs) are not real-time. The purpose of this section is to present the results of using bacteriorhodopsin for superficial X-ray sensing, which has the potential for in vivo patient dosimetry.

4.2.1 Superficial X-ray machine

The superficial X-ray machine is a Gulmay Medical D3000 DXR (Gulmay Ltd., Chertsey, UK) X-ray unit at the Grand River Regional Cancer Center in Kitchener, Ontario. There are generally two main types of kilovoltage X-rays beams used for therapy; the superficial X-ray beams which typically are generated at tube potentials ranging from 50 to 160 kV, and the orthovoltage X-ray beams which are generated at tube potentials ranging from about 160 to 500 kV. The Gulmay D3000 DXR which was used for this study operates at tube potentials from 80 to 150 kVp. The system is fully user-configurable across its range of operation with regard to tube potential (kVp), tube current (mA) and external added filtration, making it possible to obtain a wide range of beam qualities. A range of circular open-ended cone applicators (15 and 25 cm focus-to-surface distance (FSD)), are used to define the radiation field size on the patient. Lead cutouts are also used to further define any beam shape or size as needed. The dose output calibration of the unit is achieved by determining the absorbed dose delivered to a reference point for a fixed time using one reference applicator, which is defined for each beam energy. The calibration of the unit is traceable to an accredited national dosimetry laboratory (NRC, Ottawa, Canada). Different quality assurance tests are performed on this unit daily, weekly, monthly and annually to ensure the consistency and reproducibility of the output of the unit. The unit has been configured to the radiation beam characteristics given in Table 1.1.

Table 4.2: Summary of the tube potential, tube current and beam quality parameters.

Filter	External Filtration	Effective Photon Energy (keV)	Mean Photon Energy (keV)	Tube Potential (kV_p)	Tube Current (mA)	Measured HVL (mm Al)	Reference Output (cGy/min)
1	0.8 mm Al	23.3	36.6	80	4.0	1.1	350.0
2	2.0 mm Al	29.2	40.9	80	8.0	2.3	319.9
3	0.1mm Cu + 1.8mm Al	41.2	53.2	100	10.5	5.0	274.4
4	0.3mm Cu + 1.1mm Al	55.1	64.7	120	11.2	8.1	254.0
5	2.0mm Cu + 1.2mm Al	91.6	95.2	150	18.0	13.8	167.8

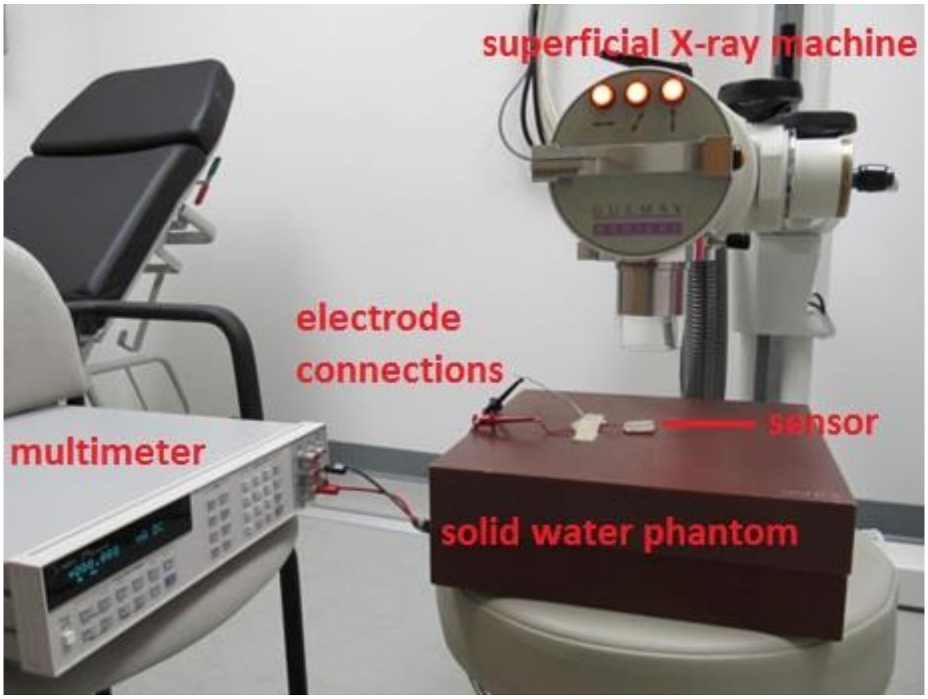

Figure 4.6 Superficial X-ray source used for characterization of radiation sensors under kilovoltage X-ray beam

4.2.2 Measurement set up for experiments with superficial X-ray machine

The tube potential ranges from 80 to 150 kVp, corresponding to mean photon beam energies of 36.6 keV and 95.2 keV, respectively. The tube current ranges from 4.0 mA to 10 mA and the half value layers ranges from 1.1 mm Al to 13.8 mm Al. For a selected beam quality different dose rates can be achieved by varying the source to target distance. Unless otherwise mentioned, the source to sensor distance is 15 cm and the diameter of the cone is 5 cm.

The sensor was placed along the central axis of the beam and on a 10 cm thick block of water equivalent phantom (solid water) to provide adequate backscatter. The electrodes are directly connected to an Agilent 3458A multimeter (Agilent Technologies, Inc.). The multimeter records the real time current on a connected computer. The sampling rate of data acquisition is 10 Hz. No external bias voltage was applied in the measurement.

4.2.3 Results

In order to study the response of BR sensor under X-ray beam irradiation, various variables such as radiation beam energy, dose rate, dose and field size are considered. Figure **4.7** presents radiation induced current in the BR sensor under dose rates of 50, 100 and 150 cGy/min for radiation energies of 100, 120 and 150 kVp. For each tube potential energy, the moving average of the measured current is also calculated based on sets of 10 data points. In each graph, the moving average is shown on the right for more clarity. The average current increases linearly with the increase of the dose rate. The magnitude of the radiation induced current is in the range of 10 pA to 0.1 nA.

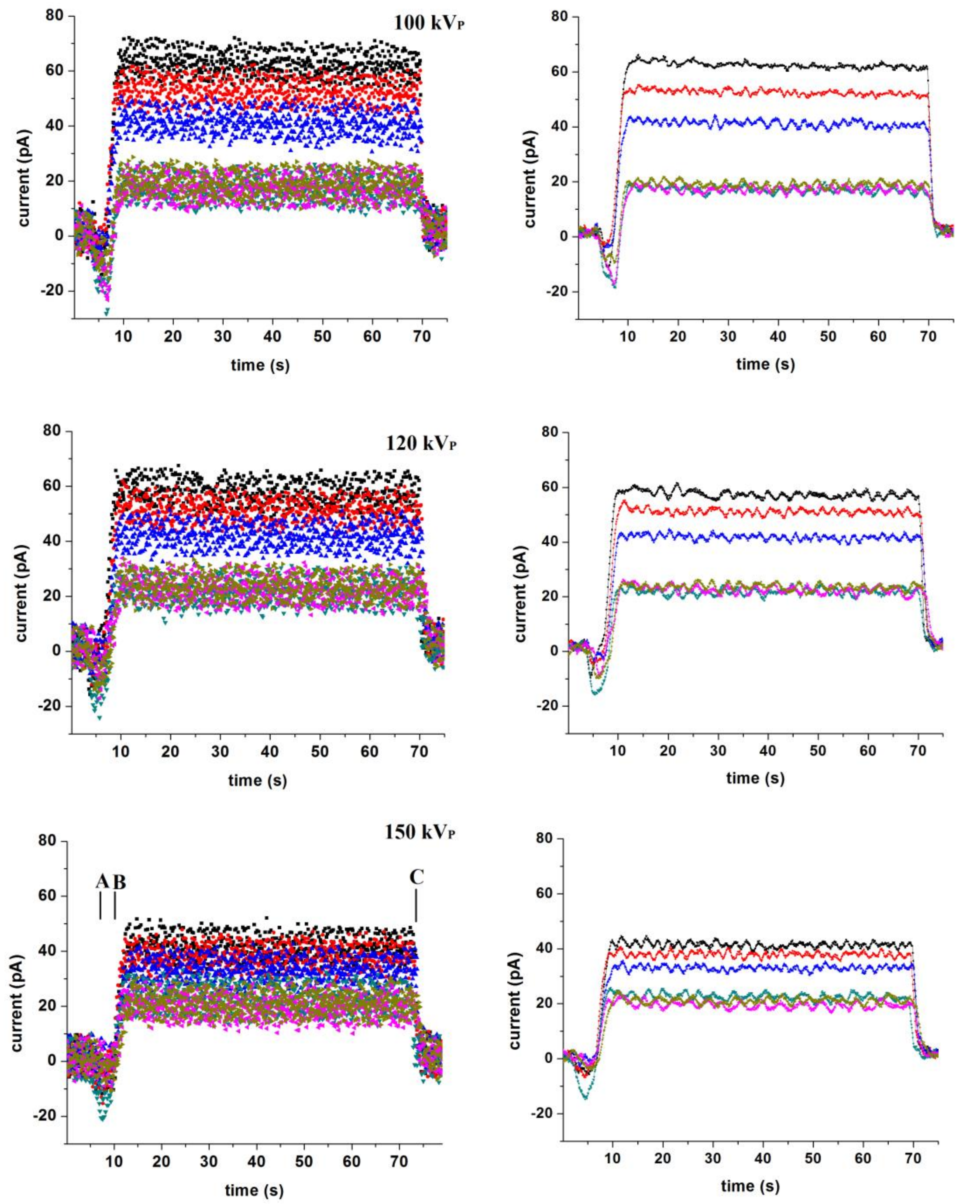

Figure 4.7: Response of BR sensor under dose rates of 50 cGy/min (blue), 100 cGy/min (red) and 150 cGy/min (black) for tube potential energies of 100 kVp , 120 kVp and 150 kVp. For each energy, response of control sample (sensor without BR) for three dose rates are also presented, which have lower values comparing with BR sensor. X-ray machine is on at point A, however it does not reach its set values before point B. X-ray is off

at point C. For each tube potential energy, the moving average is calculated based on sets of 10 data points and shown on right.

The initial response of the sensor is a negative signal with a sudden increase to a level which stays as a plateau during radiation. When the radiation beam is turned off, the signal disappears with no residual effect. Experiments are also repeated for a control sensor. The control sensor is exactly the same as the BR sensor without the sensing material (BR). For all the above energies, BR sensor not only resolves different dose rates but also there is a distinguishable difference between the response of the control and BR sensor. This suggests that the main response to X-ray radiations is coming from BR molecules. Radiation induced current by BR molecules is calculated by subtracting the control signal from the sensor and the result is summarized in Table **4.3**.

Table 4.3: Average radiation induced current per area generated in BR molecules only.

Dose Rate (cGy/min)	Average Radiation Induced Current per Area (pA/cm^2)		
	100 kV_p	120 kV_p	150 kV_p
50	70.81	58.56	35.99
100	114.08	89.99	54.17
150	144.48	114.76	56.76

At each energy, current rises when the dose rate is increased. The measured signal decreases slightly as energy is increased to 150 kVp. This might be due to more contribution from Compton effect in higher energies in comparison with dominant photoelectric effect in lower energies. Since the main constituents of BR are amino acids [28], BR molecules interact with X-rays as a low effective atomic number (low Zeff) material. While the change in energy is not dramatic, it is significant enough to produce overlap for dose rates of different energies. However, as long as the energy of the radiation is known, measured induced current for each dose rate is unique and can be recorded in real time. The dose dependence of BR sensor was tested by irradiating the sensor with 80 kV_p X-ray beam at a dose rate of 291.6 cGy/min (SSD = 15 cm) for 0.5, 1, 1.5, 2 and 2.5 min. The collected induced current is then integrated over radiation time to calculate radiation induced charge in the sensor, which is presented in nC. The response is relatively linear and there is an increase in charge as the irradiated dose on sensor increases (Figure **4.8**).

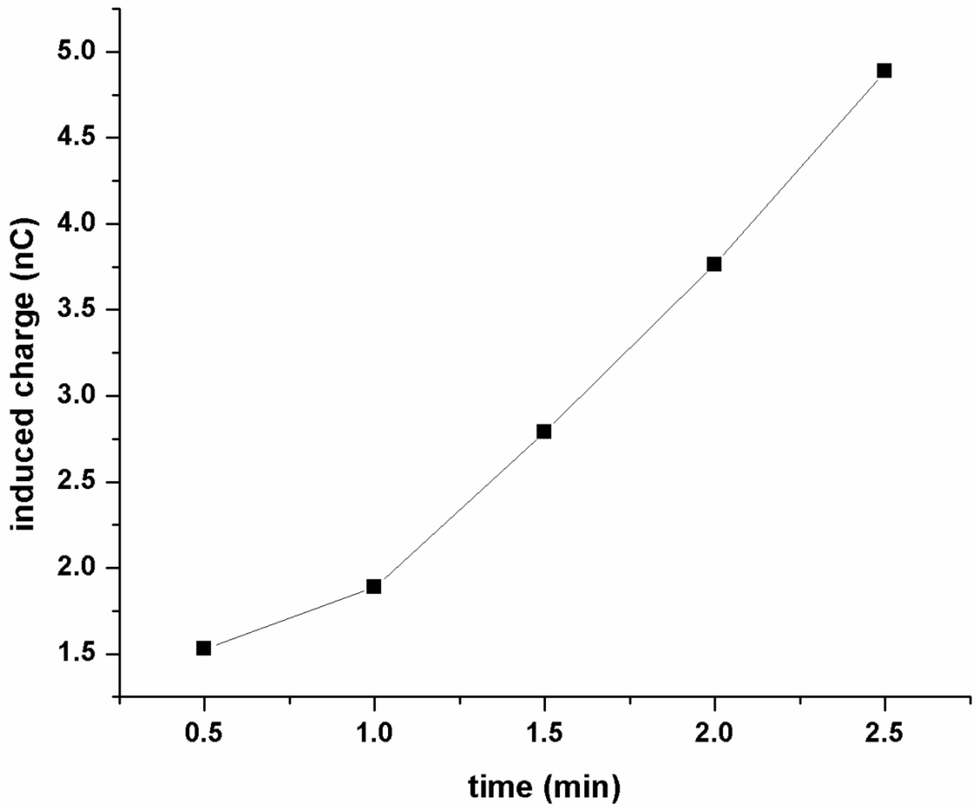

Figure 4.8: BR sensor for radiation dose measurement. Sensor is placed under 80 kVp X-ray radiations for 0.5, 1, 1.5, 2 and 2.5 minutes**.**

We also tested the sensor under different radiation field sizes and the average induced current increased by ~42% when we increased the diameter of radiation field size from Ø=1 cm to Ø= 4 cm (Figure **4.9**). As the radiation field size is increased, it covers an area larger than the sensor, and so not all the photons in the beam

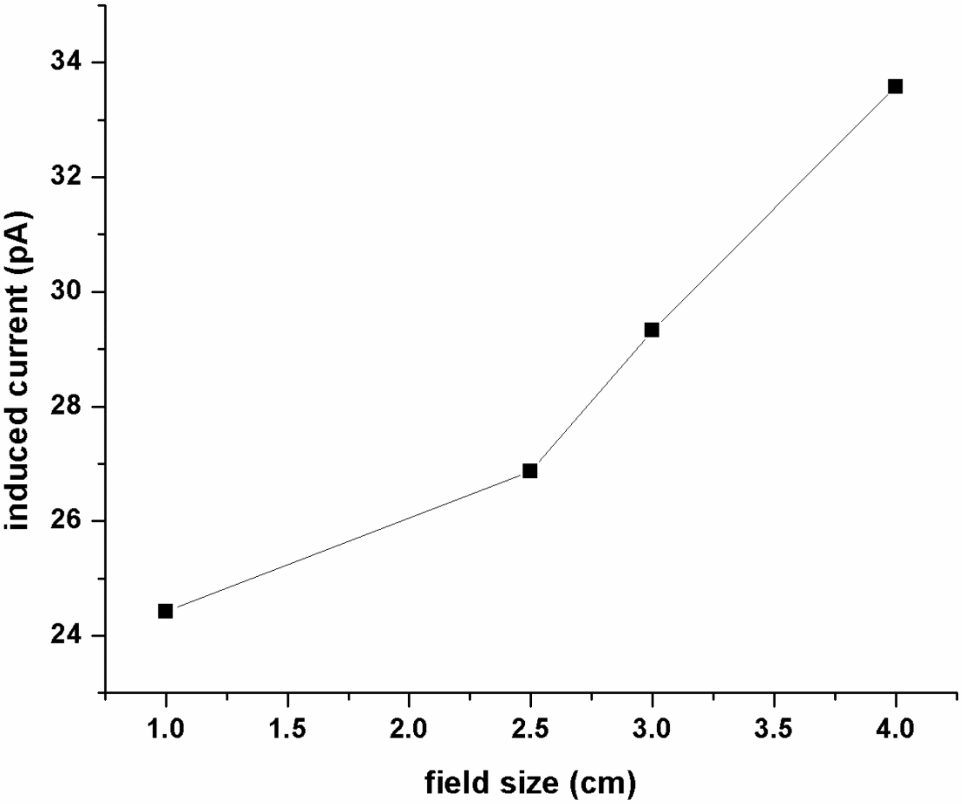

Figure 4.9: Response of BR sensor under different field sizes for 80 kVp X-ray radiation with dose rate of 291.6 cGy/min (SSD= 15 cm). Values shown on horizontal axis are diameters of the radiation field. The field size is changed by replacing the cones with different diameters at the head of the X-ray machine.

interact with the sensor. Therefore, it is not expected that the response of the sensor changes linearly with the increase in field size. Typically, radiation dose increases with radiation field size an gradually plateaus. Therefore, it is expected that the plateau occurs in larger field sizes. A reliable radiation sensor is one which generates repeatable signals under the same irradiation conditions. The BR sensor was irradiated with 80 kV X-ray beam at a dose rate of 291.6 cGy/min (SSD = 15 cm) for 12 s followed by 12 s of relaxation time and this process was repeated for 5 times (Figure **4**.**10**). The average measured induced current is 34 pA and the relative standard deviation is 7%. Also, to check the reproducibility, performance of two sensors which have been fabricated equally was tested under the same radiation conditions. Two sensors were placed under 150 kV_p X-ray beam for one minute (Ø= 5 cm, FSD=15 cm). The average currents measured for these sensors were 49 pA and 57.7 pA. Relative standard deviation of the signal for these two sensors is 8.15%.

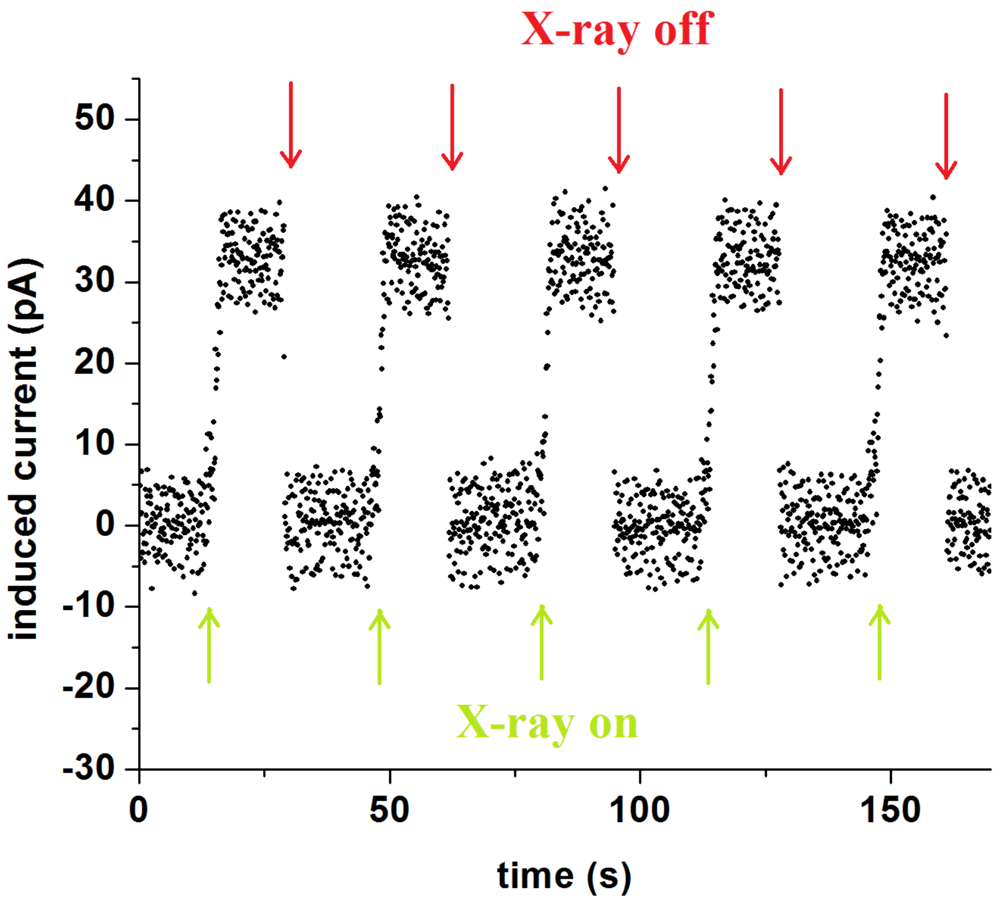

Figure 4.10: The sensor is irradiated by 80 kVp X-ray with dose rate of 291.6 cGy/min (SSD= 15 cm) for 12 s followed by 12 s of relaxation time and this process is repeated for 5 times.

4.2.4 Discussion

X-ray absorption of BR has been studied for a wide range of energies [78]. In keV energy range, X-ray absorption of cation binding sites in the purple membrane has been studied for energies of <10 keV [79]. In the interaction of few 10s keV photons with low-Z materials, the dominant interaction mechanisms are photoelectric effect and Compton scattering. While the dominant interaction in lower energies is photoelectric effect, in higher energies Compton scattering becomes dominant. This has been observed in interaction of photons with amino acids [82]. To get higher dose rates, the source head is placed closer to the sensor. For a constant dose rate, this distance is closer for higher energies. In this case there is less back scattering and as such less signal. In comparison with current radiation sensors and dosimeters, BR sensor is a biomaterial based radiation sensor and works based on measuring the radiation induced current. As the data is collected and recorded in real time, history of received dose with detail is stored and the total accumulated dose can be calculated. However, sensitivity of this sensor to background dose in radiation facilities over long time has not been tested yet. Current response time of sensor is 100 ms. A better data acquisition system is required to measure any faster response time. Under the superficial X-ray machine, we have tested BR sensor under tube potentials ranging from 80 to 150 kVp. In diagnostic radiology, tube potentials ranging from 40 to 150 kVp are used. The main difference between the spectrum we used and that of diagnostic radiology is that the superficial spectrum is heavily filtered to ensure a relatively high mean energy where as in diagnostic radiology the total filtration is relatively low (about 1 mm Be). If miniaturized, an array of this sensor can also be used in beam calibration of X-ray machines for radiation therapy.

Chapter 5

An X-ray sensor for diagnostic radiology based on thin film of bismuth sulfide

BR sensor has been tested under a linear accelerator with megavoltage energy beam and a superficial X-ray machine with a kilovoltage X-ray beam. The irradiation time under each of the above X-ray sources was more than 10 s. When tested under diagnostic X-ray machines, the response of BR sensor was not satisfactory and the level of noise was high. The best signal to noise ratio for BR sensor was obtained under megavoltage X-ray beam. One of the important differences in the application of diagnostic X-ray machines and radiation therapy X-ray sources is in their irradiation time. For imaging, few milliseconds of irradiation suffice, while several seconds and up to few minutes of irradiation may be required in radiation therapy. The goal of this chapter is to fabricate a radiation sensor for diagnostic X-ray machines for usage at room temperature.

Development of radiation detectors based on high atomic number and high density materials has been of interest for more than a decade. These materials have excellent detection efficiencies and higher photon stopping power (energy lost per unit thickness travelled) [83]. They also have attenuation coefficients, which are higher than that of sensing materials frequently used in radiation detection. For example, lead has an attenuation coefficient which is 10 times higher than the attenuation coefficient of germanium at some energies. Radiation detectors based on high atomic number and high density materials such as lead iodide (PbI_2) [84], thallium bromide (TlBr) [85] and mercury iodide (HgI_2) [86] have been fabricated and tested under different radiation energies.

Bismuth has a high atomic number of 83 and density of 9.78 g/cm^3. So far, several room temperature radiation detectors have been fabricated based on bismuth compounds such as bismuth tri-iodide (BiI_3) [87][88]. Bismuth sulfide (Bi_2S_3) is an invaluable metal chalcogenide with applications in optoelectronic, thermoelectric, and photoelectrochemical devices [89]. It has a wide band gap of 1.3-1.5 eV which allows low noise operation at room temperature [90]. In the nanometer scale, bismuth sulphide can be formed in structures such as quantum dots [91], [92], nanorods and nanofibers [93], [94], [95]. These materials can be used in bottom-up micro/nanofabrication processes or for new applications. For example, there are several thermoelectric applications proposed for bismuth nanowires [96]. Polymer coated bismuth sulfide nanoparticles have also been used as contrast agent in X-ray computed tomography [97].

In this chapter, we have fabricated a real-time radiation sensor capable for use in the diagnostic radiology departments. To fabricate the radiation sensor, an easy solution-based fabrication method is used to create a thin film of Bi_2S_3 on a mechanically flexible substrate. This sensor is capable of detecting few 10 kilovoltage X-ray photons under commercially available diagnostic radiology X-ray machines. It requires low bias voltage for operation and can potentially be miniaturized.

5.1 Materials and Methods

5.1.1 Bismuth sulfide

Bismuth sulfide thin film is formed on the conductive side of an indium tin oxide (ITO) coated polyethylene terephthalate (PET) sheet by means of chemical deposition. First, the ITO-PET sheet is cut into 2.5 cm × 4.5 cm rectangles by laser and double-sided tape is used to mount each rectangle on a glass slide. Part of the ITO side where ITO electrodes will be etched, does not require bismuth sulfide coating and is covered by a 1 mm thick polydimethylsiloxane (PDMS) rectangle (15 mm × 25 mm). A thin layer of uncured PDMS is applied on the bottom of the cured PDMS rectangle to bond the PDMS rectangle on ITO and it is left at room temperature for 48 hours for complete curing.

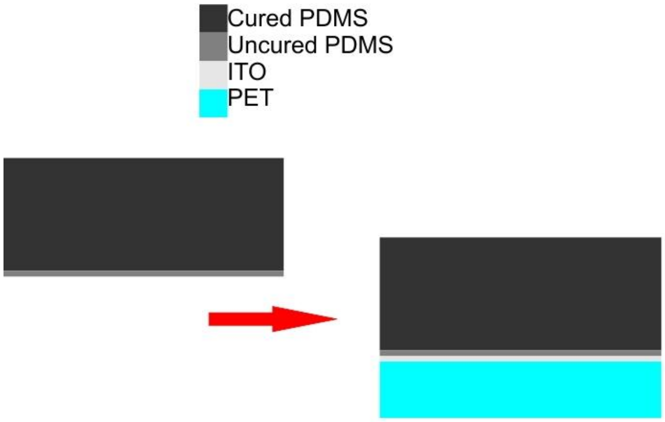

Figure 5.1: Transferring the PDMS layer to the PET ITO sheet using uncured PDMS to bond the two.

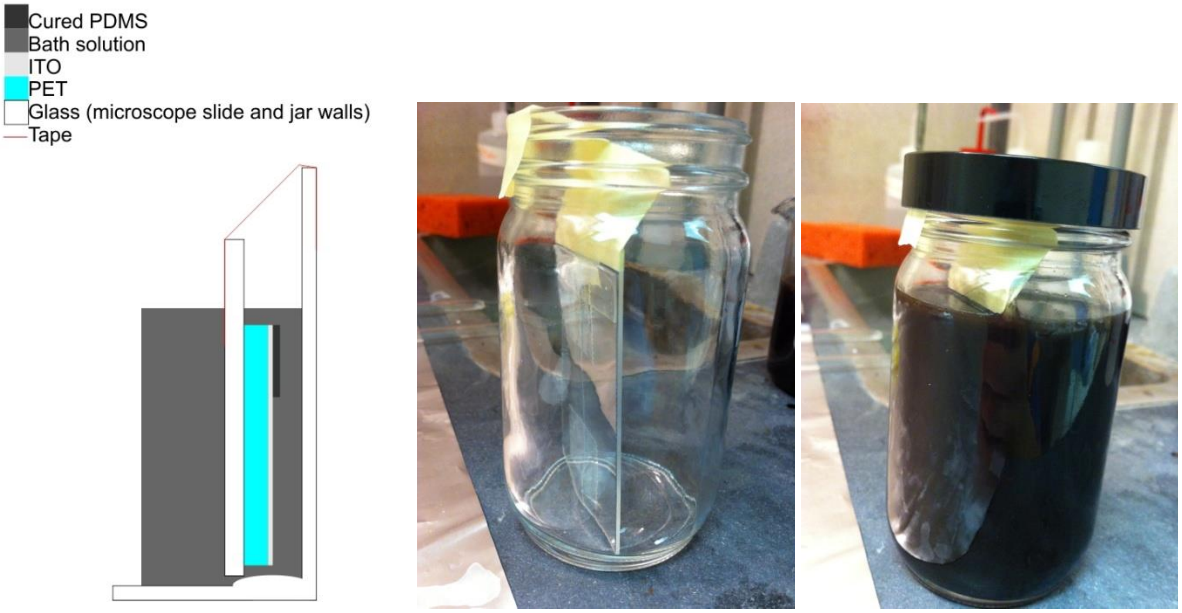

Figure 5.2: PET-ITO sheets mounted to microscope slides, sitting in the bath solution.

For the first solution, 24.25 g of $Bi(NO_3)_3 \cdot 5\ H_2O$ is stirred in with 70 mL of triethanolamine (TEA). After stirring, distilled water is added to get a total of 100 mL. 5 mL of the aforementioned solution is separately mixed in with 2 mL of a 1 M thioacetamide (TA) solution. Distilled water is added to get 50 mL total. Thickness of the deposited thin film is controlled by chemical bath time. The slides were left in the bath for six hours and then placed in a second, fresh bath for four more hours. This technique is known as the ‘double dip’ deposition method. The slides are removed, flushed with distilled water, and dried using a hot-air dryer [98]. Formation of bismuth sulfide thin film is confirmed by scanning electron microscopy (Figure **5.8**b) and energy-dispersive X-ray spectroscopy (Figure **5.9**).

The microscope slide is replaced with a clean one and the coating process is followed by deposition of a 100 nm thick layer of gold. The PDMS layer is removed and the sensor and electrodes are etched away by laser ablation of Au, bismuth sulfide and ITO layers.

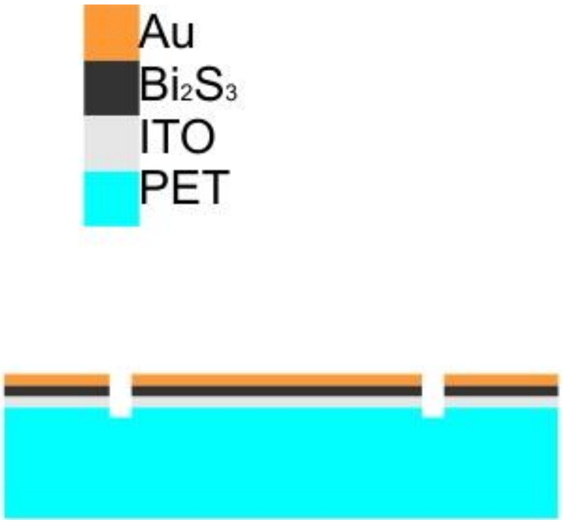

Figure 5.3: Laser etch cutting through surface layers to fabricate the sensing area, preventing electrical connections across etch.

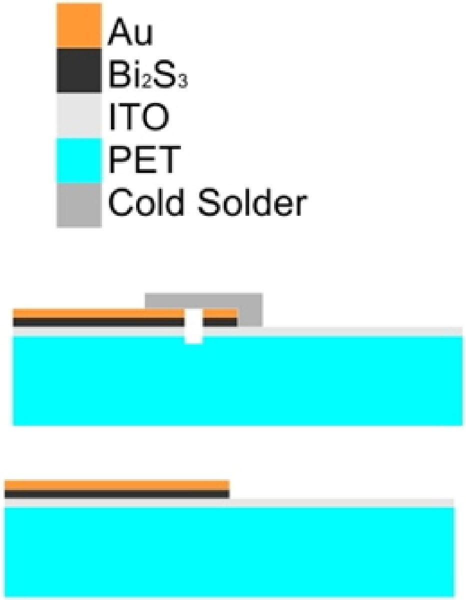

Figure 5.4: Top electrode: cold solder is used to bridge the gap from the etch to connect the gold layer to the ITO. Bottom electrode: ITO.

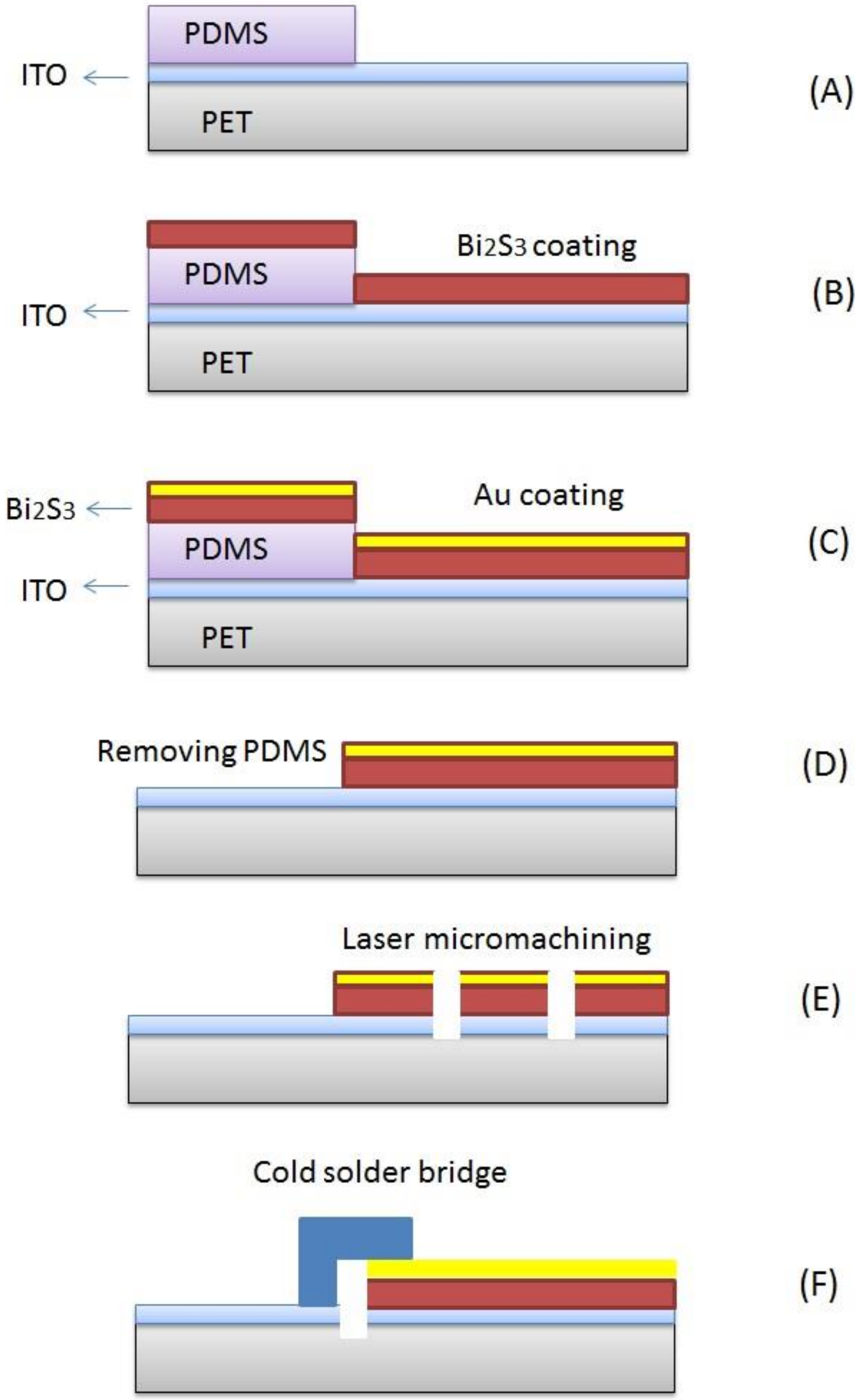

Figure 5.5: Summary of fabrication process of bismuth sulfide sensor.

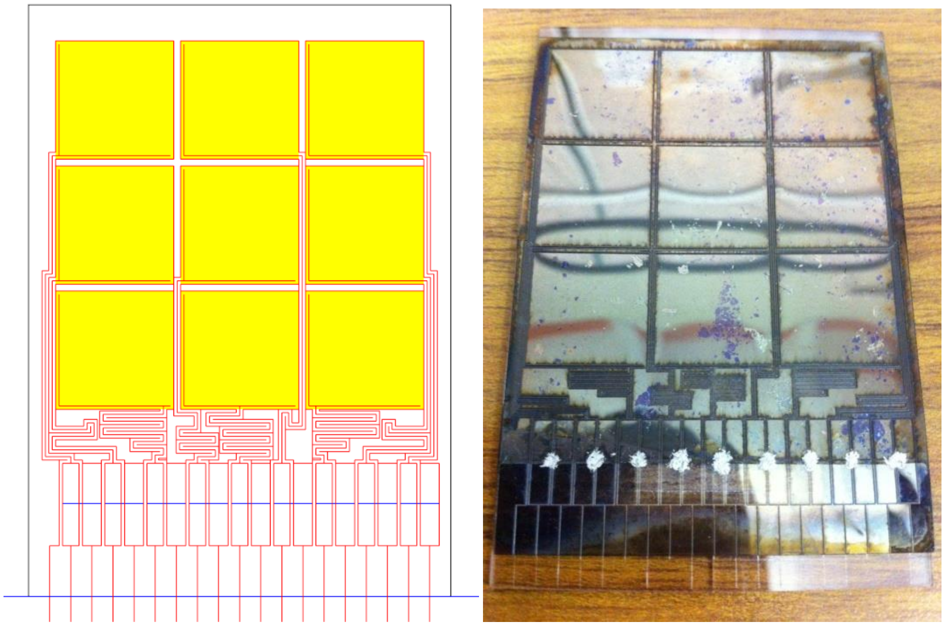

Figure 5.6: Etch design for an array of 3 × 3 sensors on a 50 mm×70 mm sheet and the fabricated array of sensors.

Variation of photon mass attenuation coefficient (μ/ρ) and effective atomic number were calculated using WinXCom program [59], [60].

5.1.2 Diagnostic X-ray imaging machine

The Ysio digital X-ray radiography system (Siemens) at Grand River Hospital, Kitchener, Ontario was used for irradiating the sensors under kilovoltage diagnostic X-rays for millisecond irradiation time. Unless otherwise mentioned, beam field size was 3 cm × 5 cm and the sensor was placed at a distance of 25 cm from the X-ray target.

Figure 5.7: Diagnostic X-raymachine used for characterization of radiation sensors under kilovoltage X-ray beam

5.1.3 Measurement set up for experiments with diagnostic X-ray machine

For characterization, each sensor is placed on a 10 cm thick block of solid water phantom (30cm x 30cm) during irradiation. A Keithley 6487 picoammeter and voltage source (Keithley Instruments) is used for current measurements.

5.2 Results

Bismuth sulfide thin film with thickness of 200 nm is formed on ITO layer. The fabricated radiation sensor is comprised of 4 layers: a flexible PET substrate, ITO coating, a thin film of bismuth sulfide and a 100 nm thick layer of gold. Photon mass attenuation coefficients of each layer are calculated for photon energies ranging from 10 keV to 150 keV (Figure **5.8** d-g). It is observed that the mass attenuation coefficients are higher for X-ray photons <50 keV. Most of the mean X-ray energies used in diagnostic radiology and computed tomography machines is within such energy range.

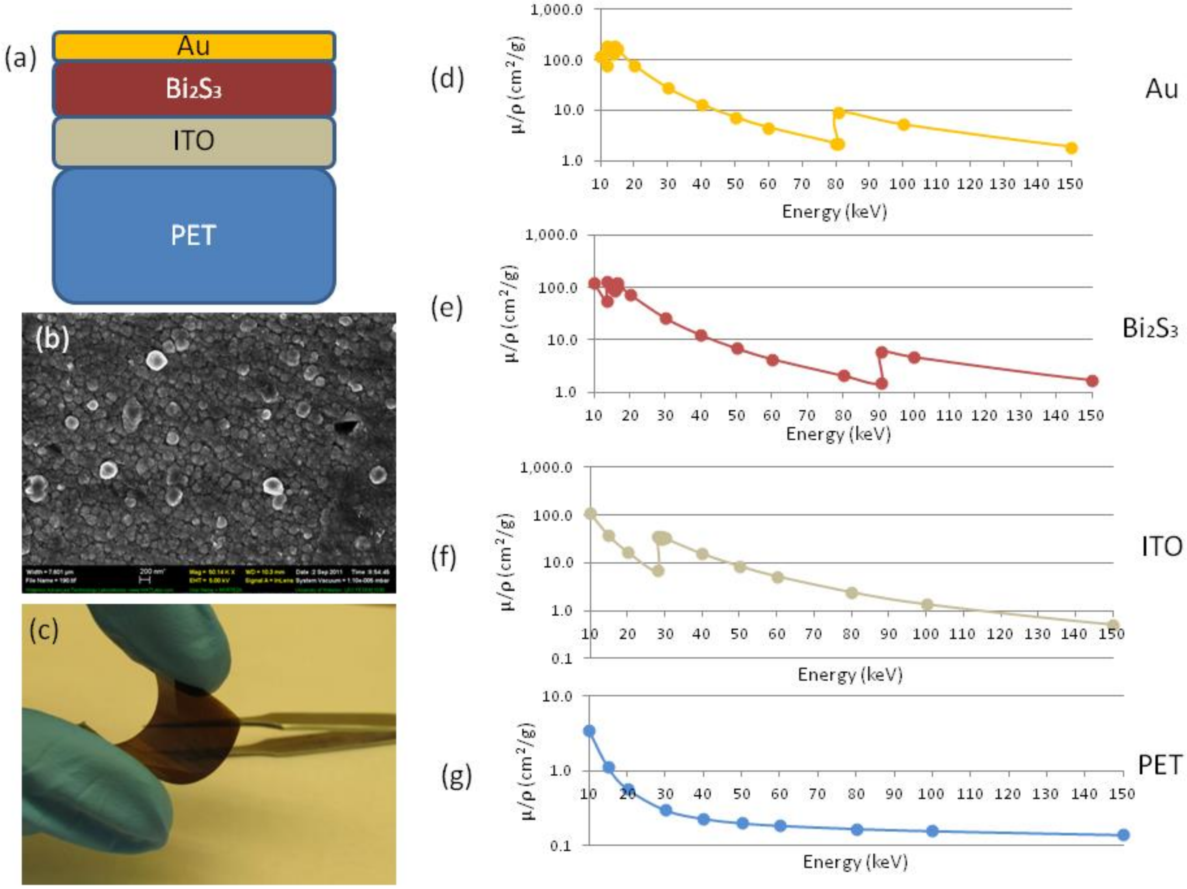

Figure 5.8: (a) Fabricated sensor is comprised of 4 layers: a flexible PET substrate, ITO, a thin film of bismuth sulfide and a layer of gold; (b) SEM image of thin film of Bi_2S_3. The scale bar is 200 nm; (c) This sensor is mechanically flexible. Photon mass attenuation coefficients of each layer are calculated for photons energies in the range 10-150 keV (d) Au; (e) bismuth sulfide; (f) ITO; (g) PET;

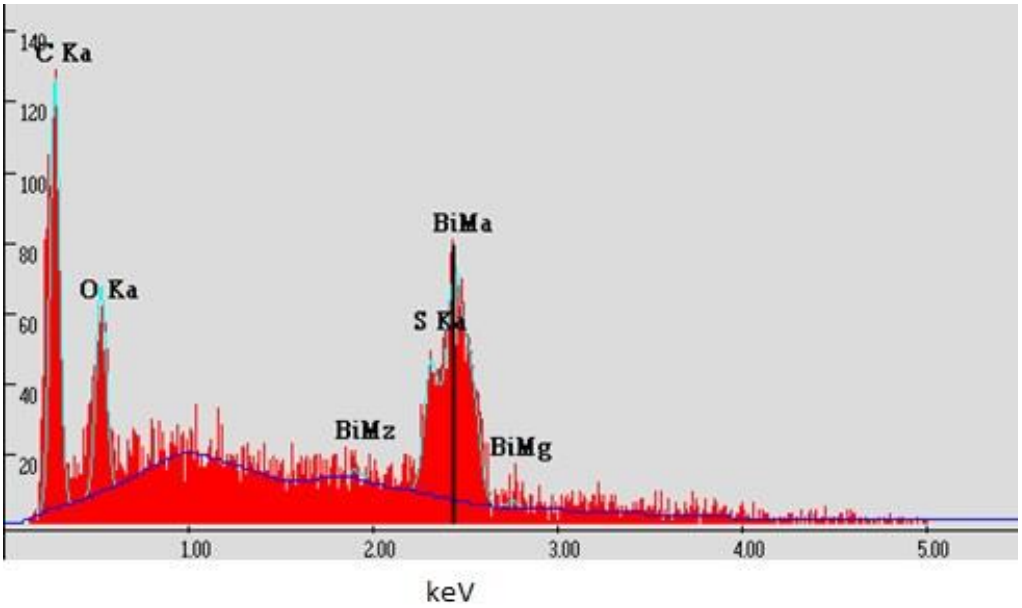

Figure 5.9: Formation of bismuth sulfide thin film on ITO surface is confirmed by energy-dispersive X-ray spectroscopy.

The sensor has a real-time response under X-ray irradiation. The response of the sensor is an increase in current when the sensor is irradiated with X-ray. This current is stored in a computer memory which can be used in real time or can be accessed later. The generated signal in the sensor is repeatable under the same irradiation conditions (Figure **5**.**10**) and has been observed for an irradiation time as short as 20 ms.

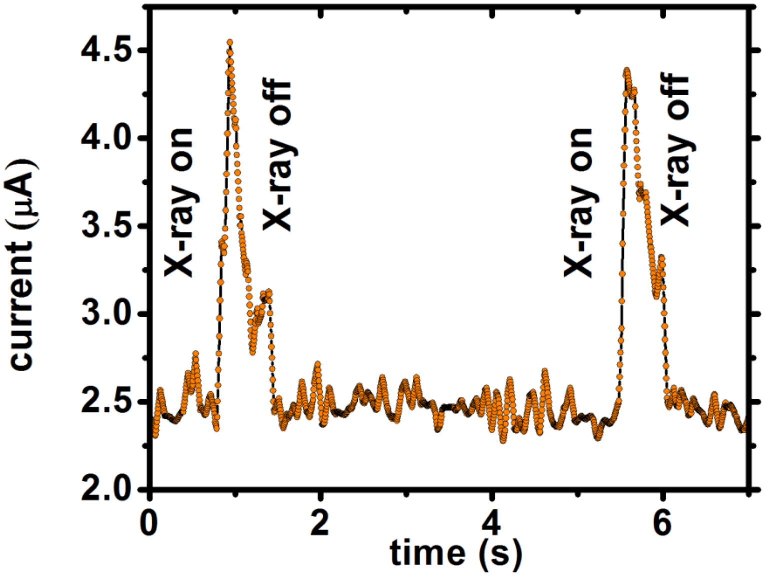

Figure 5.10: Reading was taken by Au- (Bi_2S_3)-ITO-PET sensor for X-ray radiation.This was repeated 4.5 s later. Machine was set for typical exposure parameters for a new born child chest X-ray image, thus: 0.5 mAs, 20 ms, 40 kV_p tube potential, 12 cm × 20 cm field. The applied bias voltage was 1μV.

The fabricated sensor is characterized in terms of different mAs (product of irradiation time and X-ray tube current) and mA (tube current) values of the X-ray machine. These two values determine the total delivered dose. Result of the characterization is then compared to that of an ion chamber. For this purpose a Farmer ion chamber is used, which is widely employed for Linear Accelerator absolute dosimetry and other dosimeter calibration. The liberated charges in the ion chamber are measured using an exposure meter (electrometer). In the first experiment, the exposure parameters of the X-ray machine is set from 40 mAs to 160 mAs (500 ms, 40 kV_p tube potential, 3 cm × 5 cm field size) and the signal on the sensor is measured and compared to a control sensor and the ion chamber. The current per unit area of the sensor (Figure **5.11**, black line) is higher than that of a control sensor comprising PET-ITO-Au layers (Figure **5.11**, red line). The response of the sensor versus the change in mAs is linear and shows the same trend as the ion chamber (Figure 7.9, inset).

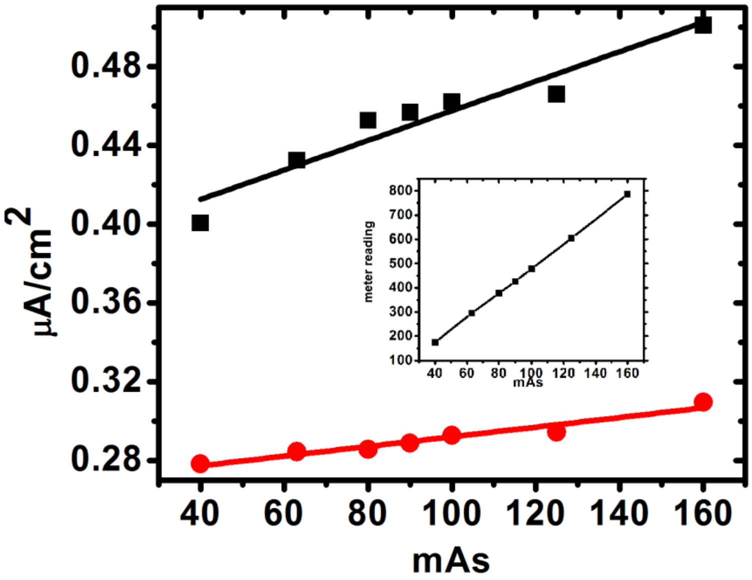

Figure 5.11: Changing mAs from 40 to 160 and measuring current per sensor area by Au- (Bi_2S_3) - ITO-PET sensor (black). Result is compared with the control sensor (red) which does not have the bismuth sulfide layer. The setting on the X-ray machine was as following: 500 ms, 40 kV_p tube potential, 5 cm × 3 cm field. The applied bias voltage was 1mV. Inset shows reading of a Farmer ion chamber under the same experiment conditions.

In the second experiment, the tube current in the X-ray generator is changed from 400 to 560 mA (200 mAs, 40 kV_p tube potential, 12 cm × 20 cm field). The response of the sensor varies linearly with the change of current (Figure 7.10). This current directly determines the photon fluence. The linear trend is also confirmed by the reading on the ion chamber (Figure **5.12**, inset).

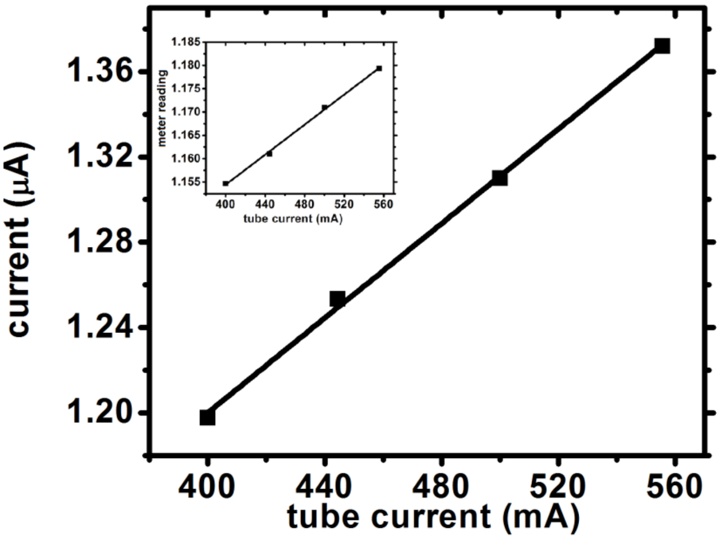

Figure 5.12: Changing tube current from 400 mA to 560 mA on X-ray machine and measuring current with Au- (Bi_2S_3) -ITO-PET sensor. The setting on the X-ray machine was as following: 200 mAs, 40 kV_p tube potential, 20 cm × 12 cm field. Inset shows reading of an ion chamber under the same experiment conditions.

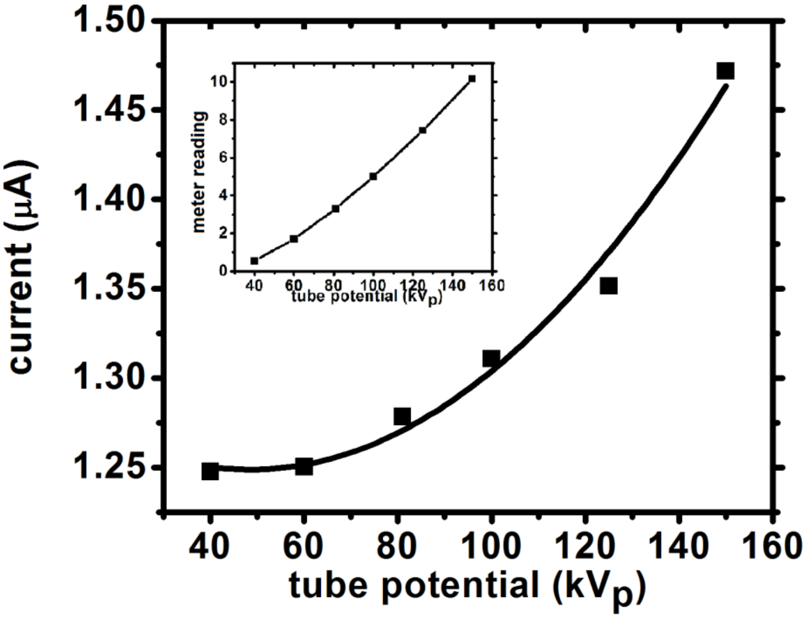

Figure 5.13: Changing tube potential from 40 kVp to 150 kVp on X-ray machine and measuring current with Au- (Bi_2S_3) -ITO-PET sensor. The setting on the X-ray machine was as following: 100 mAs, 500 ms, 40 kV$_p$ tube potential, 20 cm × 12 cm field. No bias voltage was applied for current measurement. Inset shows reading of an ion chamber under the same experiment conditions.

The fabricated sensor is sensitive to beam energy. The response of the sensor to 40 - 150 kV$_p$ tube potentials is presented in Figure **5.13**. The generated current increases with increase of the tube potential. This non-linear response is also confirmed by the reading of the ion chamber (Figure **5.13**, inset). In comparison to other energies, the sensor shows relatively constant current at 40 and 60 kV$_p$. One may roughly estimate the range of the mean X-ray energies to be ~ 13-50 keV for 40 - 150 kV$_p$. In this range of energy (up to 50 keV), photoelectric absorption is dominant for relatively high atomic number medium (i.e. bone) will absorb several times as much energy than relatively low atomic number materials (i.e soft tissue). In comparison, at higher energies, where Compton is the main interaction process (200 keV to 2 MeV), all materials, mass for mass, absorb nearly the same amount of radiation.

One of the advantages of this sensor is its capability to operate under very low bias voltages. The response of the sensor to negative and positive bias voltages is given in Figure **5.14**. For all bias voltages, the induced current increases under irradiation. A difference in the magnitude of the induced current is also observed when the sign of the bias voltage is changed. This is due to the difference in charge to mass ratio of negative and positive charges and ions.

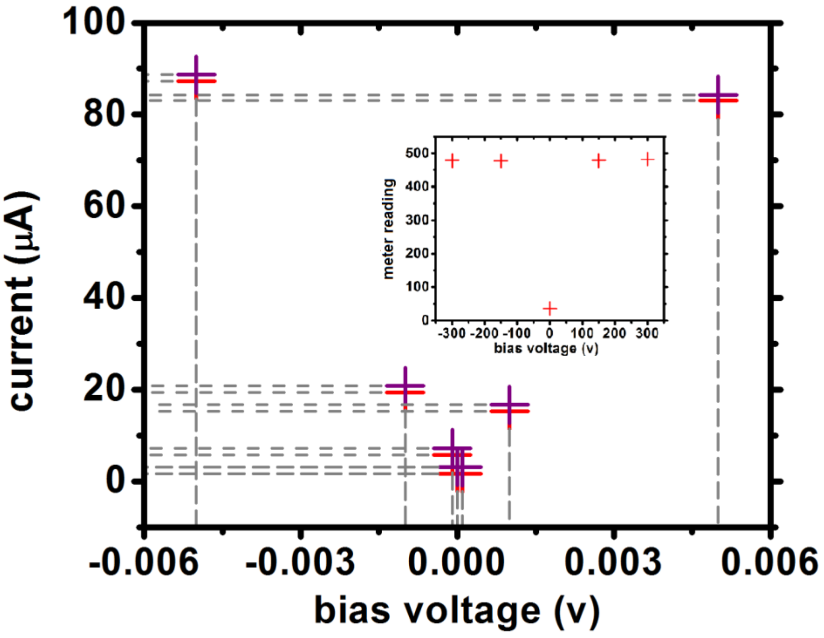

Figure 5.14: Changing bias voltage and measuring current with Au- (Bi_2S_3) -ITO-PET sensor. The current is increased under radiation (pink). An asymmetry is observed due to the difference in charge to mass ratio of negative and positive charges and ions. The setting on the X-ray machine was as following: 100 mAs, 500 ms, 40 kV_p tube potential, 5 cm × 3 cm field. Inset shows reading of an ion chamber under irradiation for the same setting on X-ray machine.

5.3 Discussion

The fabricated sensor has proved to be capable of measuring X-ray radiation for very short exposure time. However, this does not restrict the application of the sensor to only diagnostic X-ray machines. In radiation therapy, the exposure time is in the range of a few ten seconds while in diagnostic applications the exposure time is within millisecond range. As such, it is required that the dose data is recorded for longer period of time when used in radiation therapy. The drawback may be an increase of thermal effect in bismuth sulfide over longer irradiation time which may significantly decrease the signal to noise ratio [99], [100].

Dominant interaction of X-ray photons with matter depends on atomic number of the irradiated material and the energy of the X-ray beam. Bismuth sulfide is a high-Z material with an effective atomic number varying between 78.5 and 82.75 for 10-150 keV photon energies (Figure **5.15**). The dominant X-ray matter interaction for such atomic number and energy is the photoelectric effect.

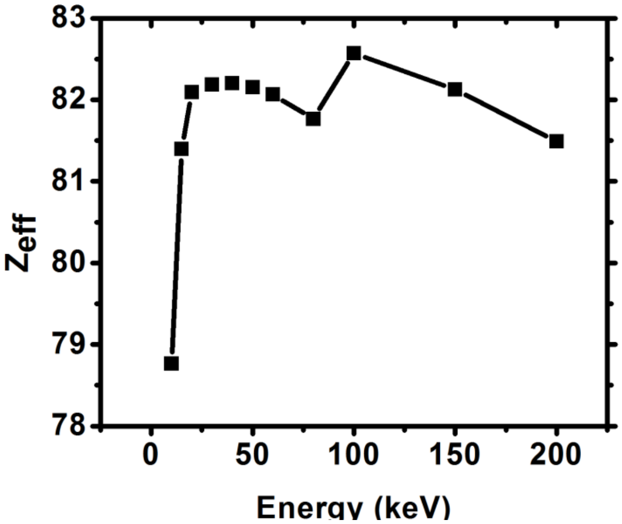

Figure 5.15: Effective atomic number of bismuth sulfide from 10-150 keV photon energies.

An ion chamber works based on collection of charges and ions produced by ionization in gas under radiation, however in the fabricated sensor the ionization in solid material is exploited to allow the detection of radiation. In addition to that, there is an increase in the conductivity under radiation. Transport of charged particles inside a medium and under the influence of an electric field is the source of electrical conductivity in materials. Ionizing radiations such as X-rays are able to increase the conduction in insulators and semiconductors by depositing energy in the material and exciting valence electrons to the conduction band. This phenomenon is called radiation induced conductivity (RIC). RIC is the difference between the conductivity of the material measured under irradiation and with no radiation [24]. Due to the presence of the bias voltage, the charges and ions generated are directed towards the opposite poles and an increase in current is observed. The movement of the induced charged particles is affected by the current already in the circuit and the generated charges with opposite poles move in opposite directions. Such movement and RIC effect reinforce the initial current. RIC has been used to explain the response of other X-ray sensors such as diamond dosimeters [75], [76]. RIC is also not limited to X-ray radiations and has been used for sensing other types of radiations [64], [101]. As such, the fabricated sensor may find other applications in radiation sensing, space technology and the nuclear industry.

An advantage of the fabricated sensor is the possibility of scale down to micrometer scale. Miniaturization of such dosimeter may lead to fabrication of an array of small dosimeters which can be used for beam symmetry and flatness checks, radiation and field light coincidence and beam detection purposes. As the fabrication process is relatively easy and cheap, this sensor will be mass producible and cost effective. The flexibility of this dosimeter may be used for new applications in radiation dosimetry on curved surfaces. While the response of the fabricated sensor can be compared to that of an ion chamber, it does not require high bias voltage for operation and this can introduce novel applications for this sensor for accurate dosimetry. Since the response of the sensor is recorded and stored on a computer memory, the data can be accessed later and cumulative dose can be calculated. As such, the fabricated sensor can be used for patient specific in vivo dosimetry to manage patient and target dose before and during radiation treatment.

Chapter 6

Radiation sensors based on nanomaterials

Application of a biomaterial in a radiation sensor has its own advantages and disadvantages. While the performance of the sensor is satisfactory and the fabrication process is easy, the cost of the biomaterial per unit weight is relatively high. Other materials which are more cost effective are nanomaterials. 1 mg of BR is sold for $651, however, 250 mg of single-walled carbon nanotube costs $356. The multi-walled carbon nanotubes are 100 times cheaper than single-walled per unit weight (Sigma-Aldrich Co). In addition to solving the cost issue, nanomaterials can be a candidate for fabrication of radiation sensors due to their specific physical and chemical properties: (i) Some of them (i.e. carbon nanotubes) are radiation resistant, which adds to the durability of the radiation sensor [102]; (ii) Depending on their geometry and size, their band gap can be engineered [103], which provides flexibility in designing the radiation sensor; (iii) The fabrication processes related to application of nanomaterials in sensors have been well developed [104].

The motivation of this chapter is to make the connection between engineering the bandgap of the nanomaterial through size change and its result on the output of the measured radiation induced conductivity or current under irradiation.

6.1 Conductivity

Conductance of an object is the ratio of the current passing through that object to the applied voltage across the object. The SI unit of conductance is seimens (S) which is equal to the conductance of an object which carries 1 A current if 1 V potential difference is applied across the object. Conductance, G, is equal to the inverse of resistance, R ($S=\Omega^{-1}$).

Electrical conductivity or specific conductance, σ, is the ability of a material to conduct an electric current. The SI unit of electrical conductivity is siemens per meter (S.m^{-1}).

Conductance and specific conductance of an object with length l and cross-section A are related by the following equation:

$$G = \sigma \frac{A}{l} \quad (7.1)$$

This equation is valid as long as the current density is uniform in the conductor. Long thin conductors such as wires have this condition.

Conductivity is based on the existence of free charge carriers in the materials (i.e. electrons in metals and ions in a melting or dissolving salt).

Conduction can be explained by the electronic structure of the material and the band model. An energy band is a range of allowed electron energies. According to this model, there are two energy bands (valence and conduction band). The population of electrons in each band and the width of the band gap between them affect the conductivity of the material. The band gap is the energy difference between the top of the valence band and the bottom of the conduction band. Insulators have large band gaps and semiconductors have smaller band gaps. Conductors have very small band gap or none, because of the overlap of the valence and conduction band.

In metals, the valence band is nearly filled with electrons and there are many free electrons in the conduction band. In semiconductors only few electrons exist in the conduction band and an insulator has almost no free electrons in the conduction band.

6.2 Radiation induced conductivity (RIC)

Ionizing radiations such as X-rays are able to increase the conduction in insulators and semiconductors by depositing energy in the material and exciting valence electrons to conduction band. This phenomenon is called radiation induced conductivity (RIC). RIC is the difference between the conductivity of the material measured under radiation and with no radiation. RIC has been studied well for insulator and semiconductor bulk materials.

RIC is a temporary change in the conduction of the material and the carrier life time of the irradiated material determines the response time. Carrier life time can be changed by introducing trapping sites in the target material by doping. If the material is pure crystalline, then the ionizing radiation can also change carrier life time by introducing radiation damage to its structure.

Standard theories of RIC [101] predict that the increase in the conductivity of the irradiated material is proportional to the rate of absorption of radiation energy by unit mass of the irradiated material i.e. dose rate:

$$\sigma_{RIC}(\dot{D}, T) = k_{RIC}(T).\,\dot{\mathrm{D}}^{\Delta(T)} \qquad (7.2)$$

The proportionality factor, k_{RIC}, is a function of temperature and properties of the irradiated material, while $\Delta(T)$ depends on the temperature only:

$$k_{RIC}(T) = e\,\mu_{\circ}\left[\left(\frac{\rho_m}{s\Sigma n_{\circ}T_1}\right)\left(\frac{m_e}{3k_BT}\right)^{\frac{1}{2}}\right]^{\Delta(T)}\left[2\left(\frac{k_BT}{2\pi\hbar^2}\sqrt{m_em_h}\right)^{3/2}\right]^{1/\Delta(T)} \qquad (7.3)$$

$$\Delta(T) = \frac{T_1}{T + T_1} \qquad (7.4).$$

In (7.3), s is capture cross section of conduction electrons by fixed holes, m_e and m_h are the electron and hole effective masses. ρ_m is the mass density , e is the charge of an electron, and $\mu_{\circ}$ is electron mobility. k_{RIC} also depends on the average energy absorbed to excite an electron from the valence band into the conduction band, which is shown as Σ.

$\Delta(T)$ is a function of the temperature of the sample (T). T_1 is a constant of the material which has the dimension of temperature and lies between T and 5T [105], [106], [107], [108]. If $T_1 \gg T$, then $\Delta \rightarrow 1$. Also, if $T_1 \rightarrow T$ then $\Delta \rightarrow 0.5$. These two limits set the top and bottom values of Δ to be 0.5 and

1 ($0.5 \leq \Delta \leq 1$). While $\Delta = 1$ shows a uniform distribution of traps in energy, $\Delta = 0.5$ represents a material with a steeply exponential distribution of traps. Equations (7.3) and (7.4) are driven with the assumption that at equilibrium, the distribution of trapped states decreased exponentially below the conduction band edge:

$$n_b\,(E) = n_0\, exp[-E_b/(k_B T_1)] \qquad (7.5)$$

In (7.5), E_b is the difference between the energy level of the state at the bottom of the conduction band and the steady state Fermi level generated due to irradiation.

6.3 RIC for radiation sensing

RIC can be used for measuring radiation. RIC sensors and detectors have the advantage of measuring radiation in the sub-nanosecond domain. To experimentally measure RIC in a sample under radiation, the sample is connected to two electrically conductive electrodes and a bias voltage is applied to define a direction for the flow of induced charges. Induced current is then measured. The range of this current is between nanoampere to picoampere. In another way, electrical resistance of the sample is directly measured under radiation and then conductivity is calculated according to the geometry of the sample.

The focus of this chapter is to investigate the possibility of fabricating nanosensors for radiation sensing based on RIC. The fabrication process of radiation sensors based on nanomaterials is a bottom-up process compared to the top-bottom strategy used for bulky materials. As such, there is a lot of flexibility on the geometry of the sensor and its customization according to its applications.

6.4 Dependence of band gap on particle size

The effective mass model of quantum confinement shows the dependence of the band gap of a nanomaterial to its size [109], [110]. Equation (7.6) shows that for a nanoparticle, the band gap (E^*) depends on the particle radius (r) as well as its electrical properties:

$$E^* \cong E_{\mathrm{g}}^{\mathrm{bulk}} + \frac{\pi^2\hbar^2}{2er^2}\left(\frac{1}{m_e m_0} + \frac{1}{m_h m_0}\right) - \frac{1.8\,e}{4\pi\epsilon\epsilon_0\,r} - \frac{0.124\,e^3}{\hbar^2\,(4\pi\epsilon\epsilon_0\,)^2}\left(\frac{1}{m_e m_0} + \frac{1}{m_h m_0}\right)^{-1} \qquad (7.6).$$

Here, $E_{\mathrm{g}}^{\mathrm{bulk}}$ is the bulk band gap in eV, m_0 is the mass of a free electron, ϵ is the relative permittivity and ϵ_0 is the permittivity of free space.

6.5 Radiation induced conductivity in nanomaterials

According to (7.3), the proportionality factor (k_{RIC})can be written as the product of two terms: one contains the average band gap energy Σ and the second part (η), which is a function of electrical properties of the sample and temperature,

$$k_{RIC} = \eta\,.\,(\Sigma)^{-\Delta/2} \qquad (7.7)$$

$$\eta = e\,\mu_{\circ}\left[\left(\frac{\rho_m}{sn_{\circ}T_1}\right)\left(\frac{m_e}{3k_BT}\right)^{\frac{1}{2}}\right]^{\Delta}\left[2\left(\frac{k_BT}{2\pi\hbar^2}\sqrt{m_e m_h}\right)^{3/2}\right]^{1/\Delta} \qquad (7.8).$$

As nanomaterials are usually comprised of only low number of atoms, one can estimate the average band gap to be equal to the band gap of the single nanomaterial ($\Sigma \cong E^*$). Equation (7.6) can then be written as below:

$$\Sigma \cong \varphi - \frac{\alpha}{r} + \frac{\beta}{r^2} \qquad (7.9)$$

$$\alpha = \frac{1.8\,e}{4\pi\epsilon\epsilon_0}\ , \qquad \beta = \frac{\pi^2\hbar^2}{2e}\left(\frac{1}{m_e m_0} + \frac{1}{m_h m_0}\right) \qquad (7.10)$$

$$\varphi = E_{\mathrm{g}}^{\mathrm{bulk}} - \frac{0.124\, e^3}{\hbar^2\, (4\pi\epsilon\epsilon_0\,)^2} \left(\frac{1}{m_e m_0} + \frac{1}{m_h m_0}\right)^{-1} \qquad (7.11)$$

The proportionality factor k_{RIC} can then be calculated by substitution of (7.9) in (7.7):

$$k_{RIC} = \eta\, .\, (\varphi - \frac{\alpha}{r} + \frac{\beta}{r^2})^{-\Delta/2} \qquad (7.12).$$

Substituting (7.11) in (7.1), relation of RIC with particle size and radiation dose rate can then be determined by:

$$\sigma_{RIC} = \left[\eta\, .\, (\varphi - \frac{\alpha}{r} + \frac{\beta}{r^2})^{-\Delta/2}\right] . (\dot{\mathrm{D}})^{\Delta} \qquad (7.13)$$

6.6 Carbon nanotube radiation sensor

6.6.1 Fabrication

A glass capillary with the size of 0.02 mm × 0.2 mm × 5 cm is filled with single wall CNT suspension (1 mg in 100 ml DI water). The ends of the capillary are closed and connected to wires by cold solder.

6.6.2 Set up

The sensor is placed under 15 MV X-ray radiations with dose rate of 600 MU/min. The field size is 10 cm × 10 cm and there is a distance of 100 cm between the source and the sensor. The wires are connected to a multimeter which measures and records the change in electrical resistance of the sensor.

6.6.3 Results

Figure **6.2** shows experimental data for a radiation sensor based on carbon nanotube (CNT) suspension that works based on RIC. More than 7% increase in the conductance of CNT suspension is observed under radiation. The conductance drops immediately after X-ray is off.

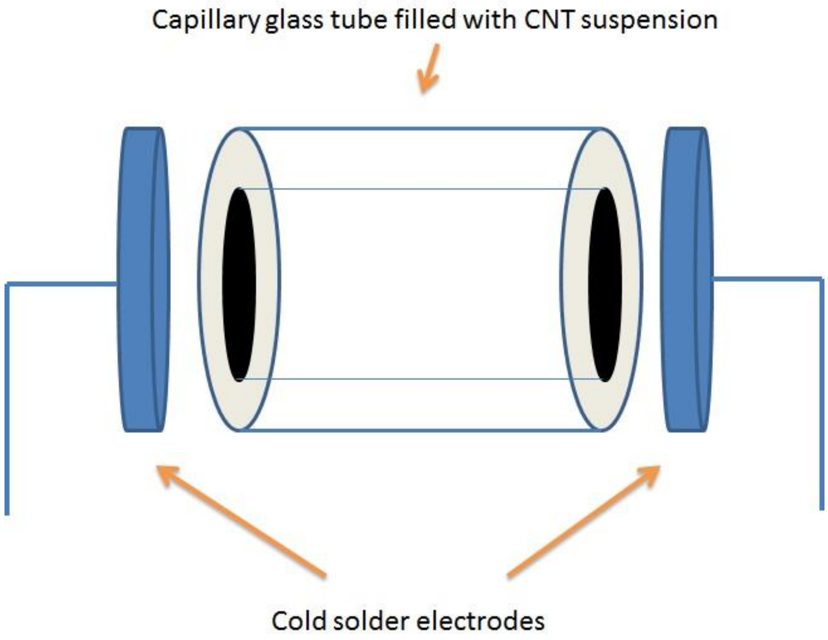

Figure 6.1: Fabrication of CNT sensor using a capillary tube

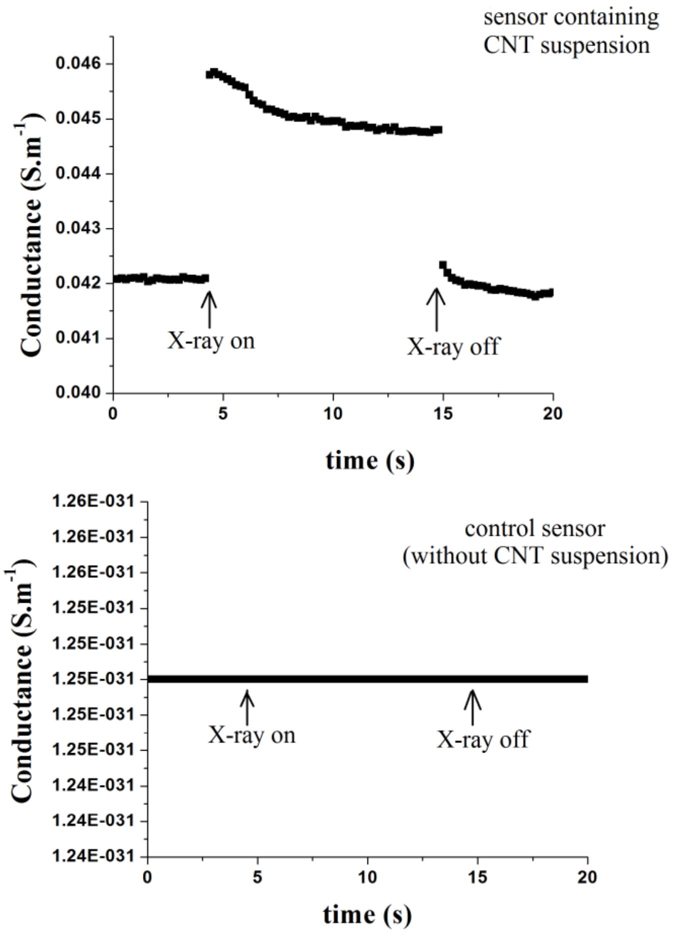

Figure 6.2: Radiation induced conductivity in carbon nanotube suspension under 15 MV, 600 MU/min X-ray radiation.

For single wall CNTs with diameter of 3 to 5 Å, band gap varies between ~ 0.24 to 0.002 eV [111]. The associated change in RIC is calculated using equations 7.2 and 7.3 (Figure **6.3**). For $\Delta = 1$, RIC increases ~ 10 times if the radius of CNT is increased by 2 Å.

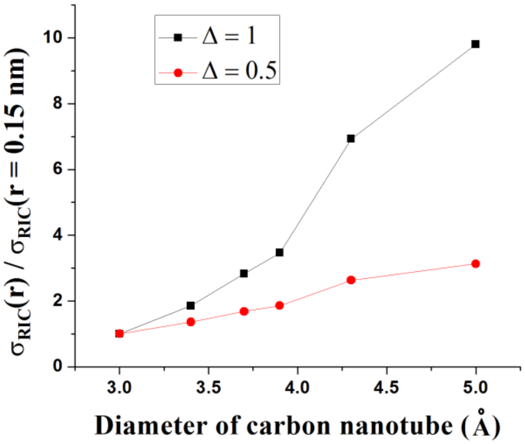

Figure 6.3: Comparison of calculated relative radiation induced conductivity for different diameters of carbon nanotubes.

6.7 Zinc oxide nanoparticle radiation sensor

As another example, we compare RIC for different sizes of ZnO nanoparticles. ZnO is a semiconducting and piezoelectric material which has been fabricated in several different geometries such as nanocombs, nanorings, nanohelixes, nanobelts, nanowires and nanocages. Such great variety of nanostructures have led to application of ZnO in nanosensors, nanocantilevers and field effect transistors [112]. ZnO has been also used in radiation sensors [113], [114]. For ZnO nanoparticles, $E_g^{\text{bulk}} = 3.2$ eV, $m_e = 0.26$, $m_h = 0.59$ and $\epsilon = 8.5$[109]. The band gap varies between ~ 4.7 to 3.2 eV for respective particle radius of 1 to 5 nm. These values are used in equations 7.2 and 7.3 to calculate the relative values of RIC.

6.7.1 Results

Figure **6.4** shows the dependence of RIC to size of ZnO nanoparticles at constant dose rate. Depending on the value of Δ, change of the radius of ZnO nanoparticle from 1 to 5 nm increases the value of RIC for 10% to 20%.

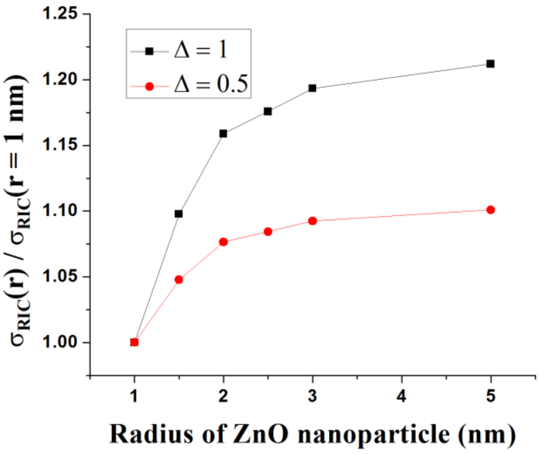

Figure 6.4: Comparison of calculated relative radiation induced conductivity for different radii of ZnO nanoparticles.

6.8 Discussion

When an insulating or a semiconducting substance is irradiated with ionizing radiations, the electrical conductivity is increased. This is due to the increase in the number of charge carriers under radiation. Under radiation, an electron is excited into conduction levels, where it can either recombine with a hole or becomes temporarily trapped. The trapped electron will be later thermally released into conduction levels again. This electron is finally captured by a bound state and will recombine with a hole. The length of time that an electron remains in the conduction level is inversely proportional to the number of traps. The photon energy of X-ray radiation is much larger than the bandgap (E^*) of the sensing material. On the average, ~ $3E^*$ is required to produce one free pair of carriers [64].

Photoconductivity is a phenomenon related to absorption of electromagnetic radiations. Such radiations can be from ultraviolet, visible or infrared part of spectrum, for instance. In general, photoconductivity is a special type of RIC. In fact, RIC can occur due to both electromagnetic and non-electromagnetic radiations and as such is a more general term in comparison with photoconductivity.

We employed the standard theory of radiation induced conductivity (RIC) and we showed that in nanomaterials, RIC depends on the size of the particle. This is due to the fact that RIC is a function of the band gap, which itself depends on the particle size in nanomaterials. In particular, we calculated RIC for CNTs and ZnO nanoparticles. For CNTs, RIC increases dramatically when CNTs with larger diameters are used. This is due to the fact that the band gap of CNT highly depends on its geometry [111].

Chapter 7
Conclusion

7.1 Conclusions and contributions

The goals of this research were design, fabrication and characterization of novel radiation sensors based on biomaterials and nanomaterials. BR was used for real time measurement of kilovoltage and megavoltage X-ray beams. Furthermore, the potential application of nanomaterials in radiation sensing was studied.

The major contributions and conclusions emerging from this research are listed below.

- This research investigates the design, fabrication and characterization of a sensor based on BR for the purpose of detecting X-ray radiations. BR thin film coated and dried on ITO electrodes is used to monitor X-ray radiation exposure through changes in radiation induced electric current. The performance of the sensor is evaluated for different dose rates, energies and field sizes. The experiments under megavoltage X-ray beam show that the output electric current of the sensor increases as the dose rate or energy increases. The sensor also detects a higher signal when the field size increases. It also measures a linear response in terms of integrated electric charge to the change of radiation dosage. The response of the sensor is in real time and repeatable. As compared to other X-ray sensors, the BR sensor is easy to fabricate, operate and can be miniaturized. It is also cost effective and can be mass produced.
- In addition to megavoltage X-ray beam, BR sensor was tested under X-ray beams of 80–150 kVp tube potentials, and for dose rates of 50, 100 and 150 cGy/min. A slight reduction in the radiation induced current was observed as the energy of the radiation was increased. Under kilovoltage X-y beam, BR sensor has a relatively linear response to dose and dose rate and provides repeatable results. Moreover, using BR sensor, keV X-ray beams are measured in real time.

- The photon mass attenuation coefficients, the effective atomic numbers and electron densities of BR and its comprising amino acids was calculated for the photon energies 1 keV–100 GeV.
- The theory of radiation induced conductivity (RIC) was applied to nanomaterials and dependence of RIC to the size of the nanostructures was calculated. In carbon nanotubes (CNTs), RIC increases dramatically when CNTs with larger diameters are used. For $\Delta = 1$, RIC increases ~ 10 times if the radius of CNT is increased by 2 Å (from 3 Å to 5 Å) . The change in the radius of ZnO nanoparticle from 1 to 5 nm increases the value of RIC for 10% to 20% (depending on the temperature). This result shows that in general, carbon nanotubes and ZnO nanoparticles of higher radius may exhibit higher values of radiation induced current under irradiation.

The advantages of using biomaterials in fabrication of a radiation sensor are as follows:

- Biomaterials have effective atomic number close to that of tissues. A tissue equivalent radiation sensing material can be used in routine quality assurance and quality control in both diagnostic and therapeutic X-ray machines.
- Functional biomaterials can be easily coated on conductive substrates.
- BR has proved to have relatively good signal to noise ratio for radiation induced current under megavoltage and kilovoltage X-rays.

The advantages of using nanomaterials in fabrication of a radiation sensor are as follows:

- Nanomaterials can be used in bottom-up fabrication techniques.
- There are several techniques of coating and alignment of high aspect ratio nanostructures which can be used for coating conductive and non-conductive substrates. Not all of these techniques require clean room facility or high vacuum systems.

- High aspect ratio nanostructures such as nanotubes and nanowires extensively increase the surface area of the coated region.
- The radiation induced conductivity is tunable according the geometry of the nanostructure.

Table 7.1: Significant advantages of the fabricated sensors.

	Real time/ no post processing	Miniaturizable/ miniaturized	Long life time	No bias voltage	No high voltage source
Carbon nanotube	✓	✓	✓		✓
Bismuth sulfide sensor	✓	✓	✓		✓
BR sensor	✓	✓	✓	✓	✓

7.2 Recommendation for future studies

- The X-ray sources are not the only radiation sources available at hospitals and cancer centers. The fabricated sensors can be tested under other radiation sources such as electron beam.
- Radiation oncology is not the only application where radiation sensors and dosimeters are required. The sensors and method of fabrication can be adjusted to requirements of applications in other industries such as space and security.
- The fabricated sensors can be potentially miniaturized.

- An array of sensors and dosimeters can be fabricated. This will add to the application of the radiation sensor and enables the user to have spatial distribution data for the measured quantity.
- The sensors can be modified to become implantable. For this purpose, a wireless transmitter and a biocompatable packaging have to be considered in design of the sensor.

Appendix A

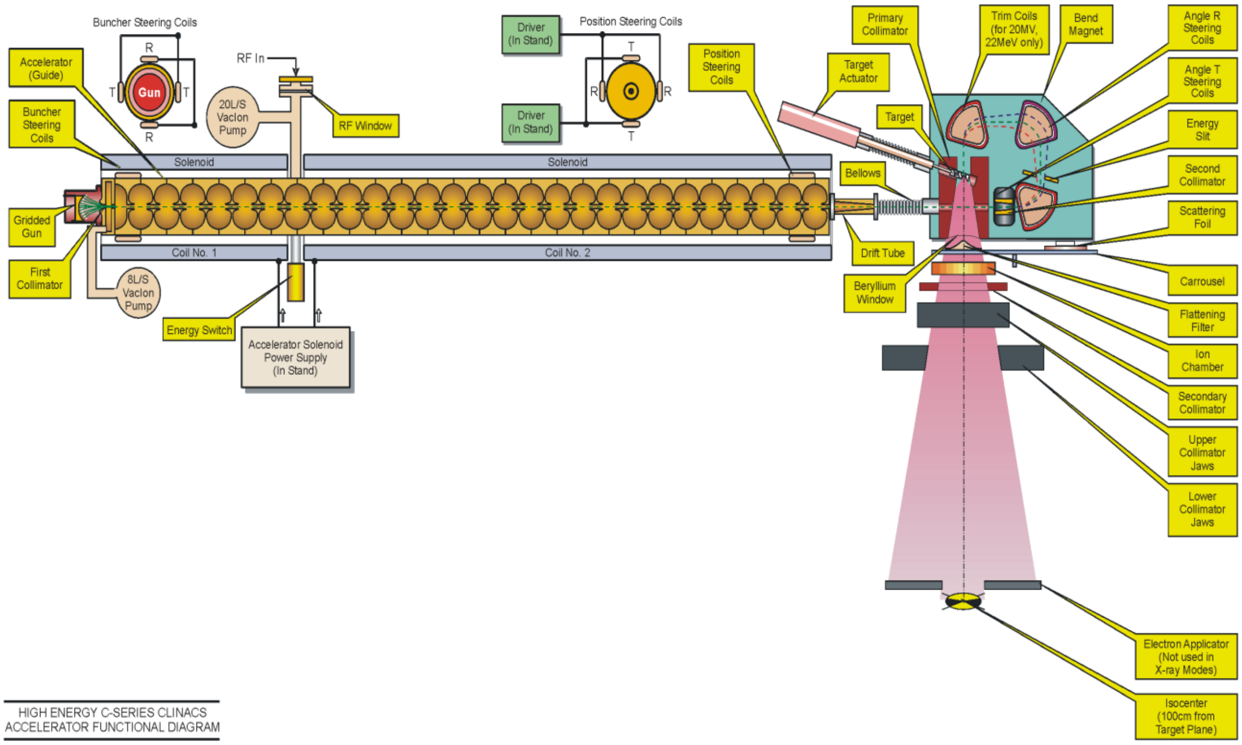

Schematic of a Varian linear accelerator

Appendix B

Calculated data for bacteriorhodopsin and its comprising amino acids

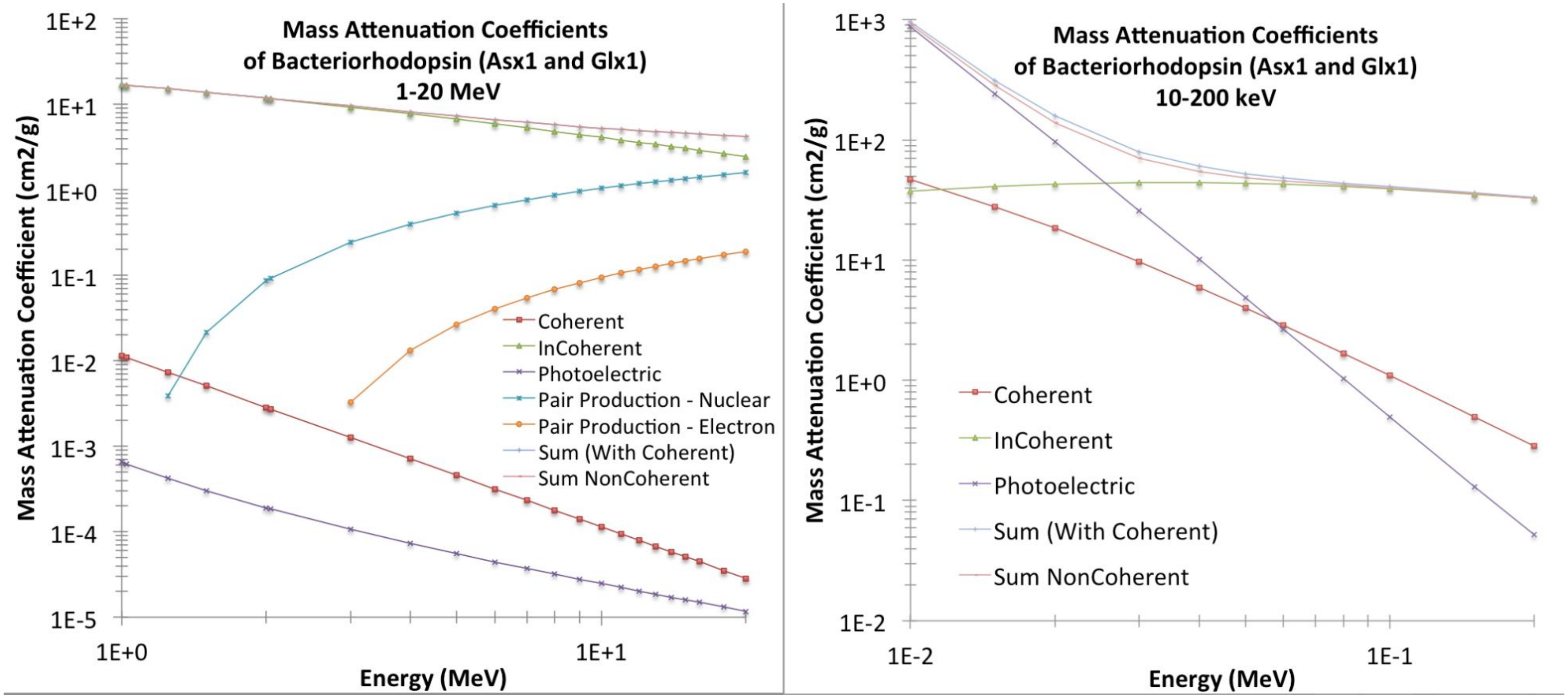

Figure 1. Mass attenuation coefficient of bacteriorhodopsin for 10-200 keV and 1-20 MeV photons.

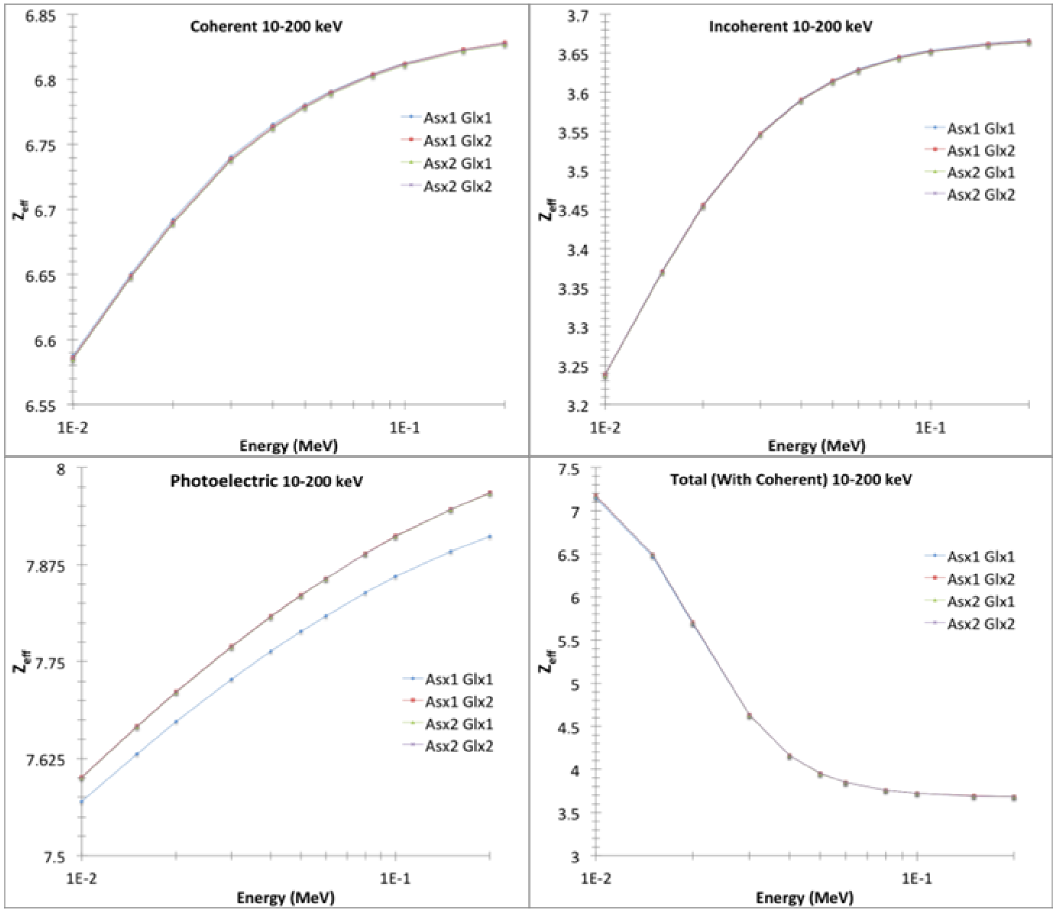

Figure 2. Effective atomic number of bacteriorhodopsin for 10-200 keV photons.

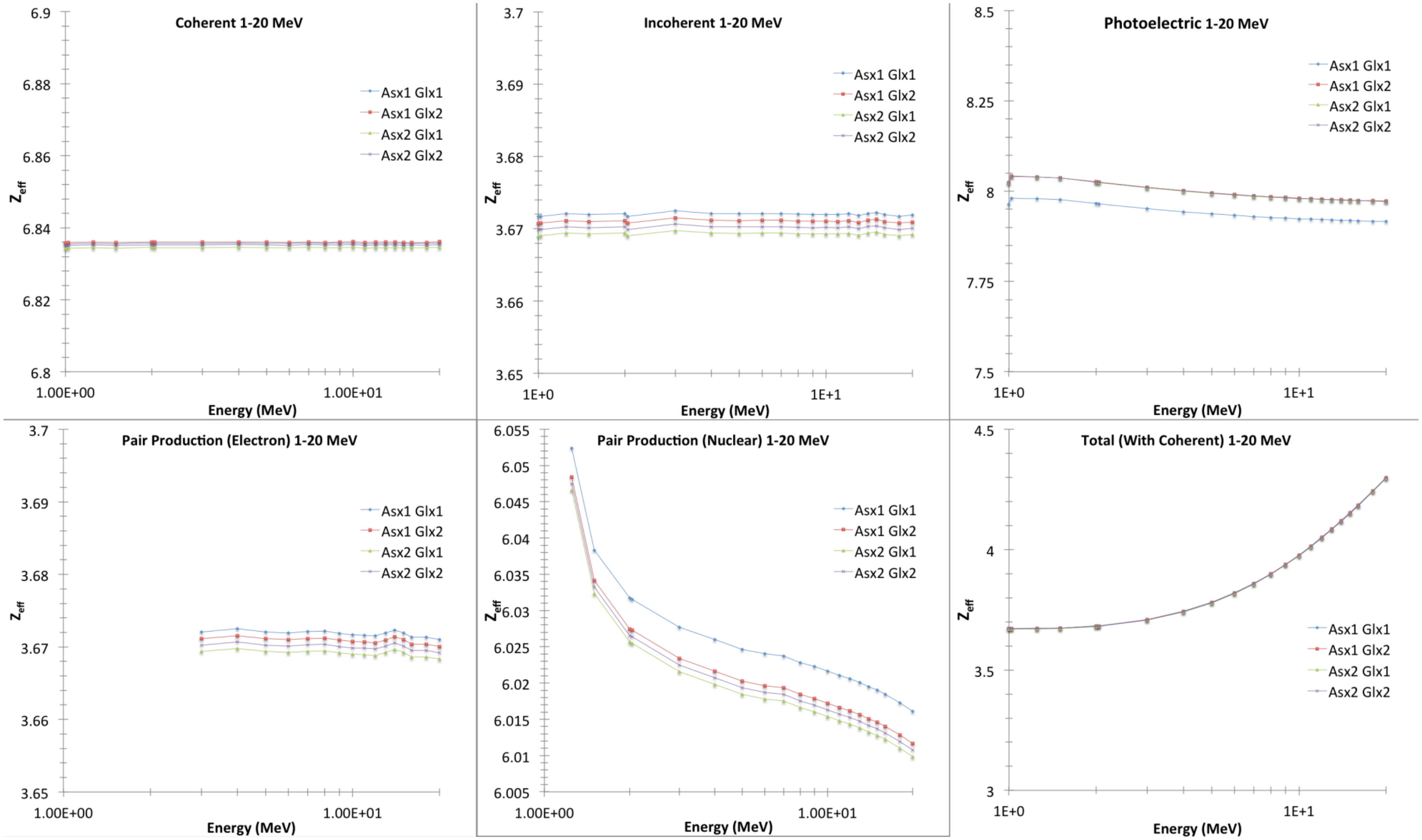

Figure 3. Effective atomic number of bacteriorhodopsin for 1-20 MeV photons.

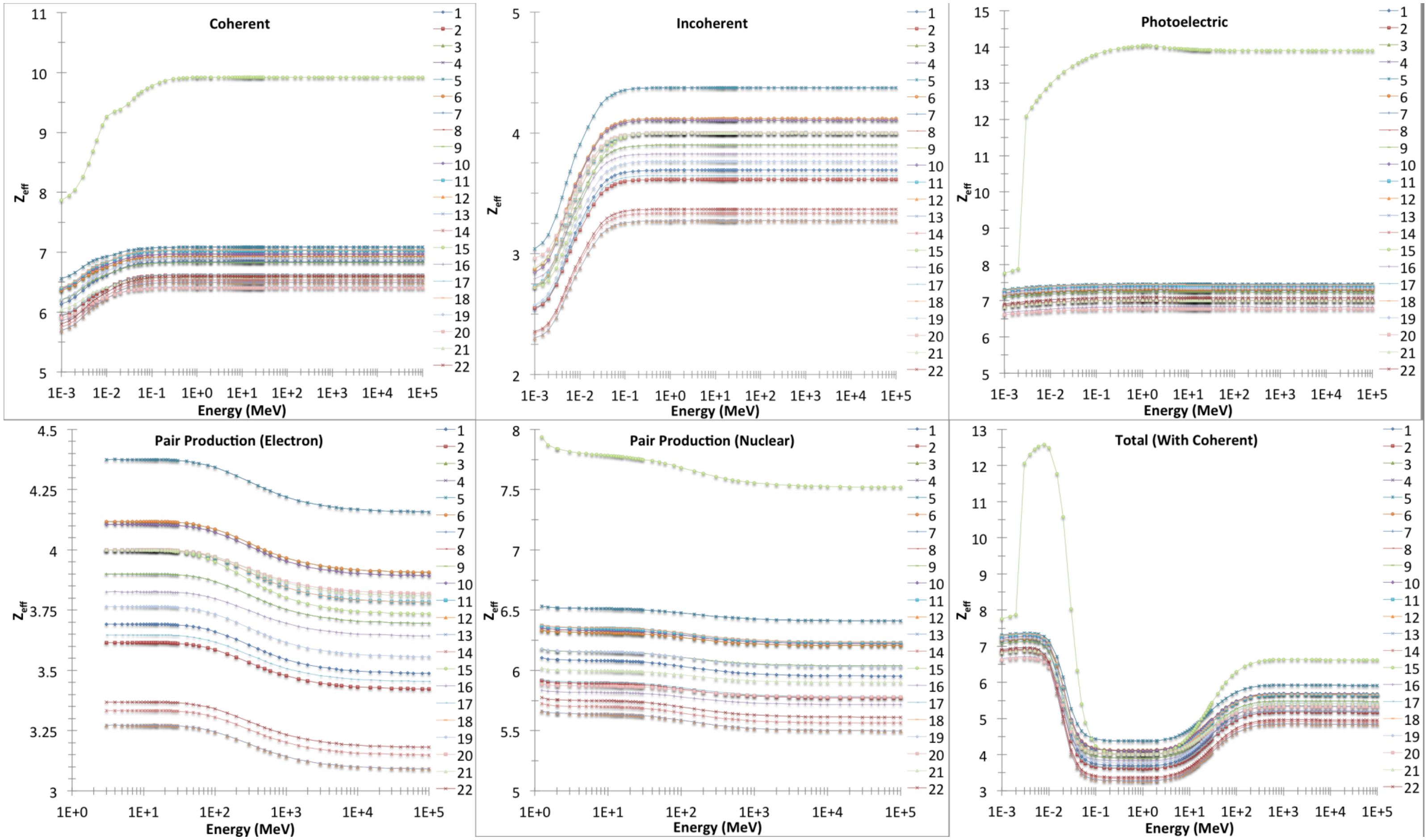

Figure 4. Effective atomic number of amino acids of bacteriorhodopsin for partial and total interactions.

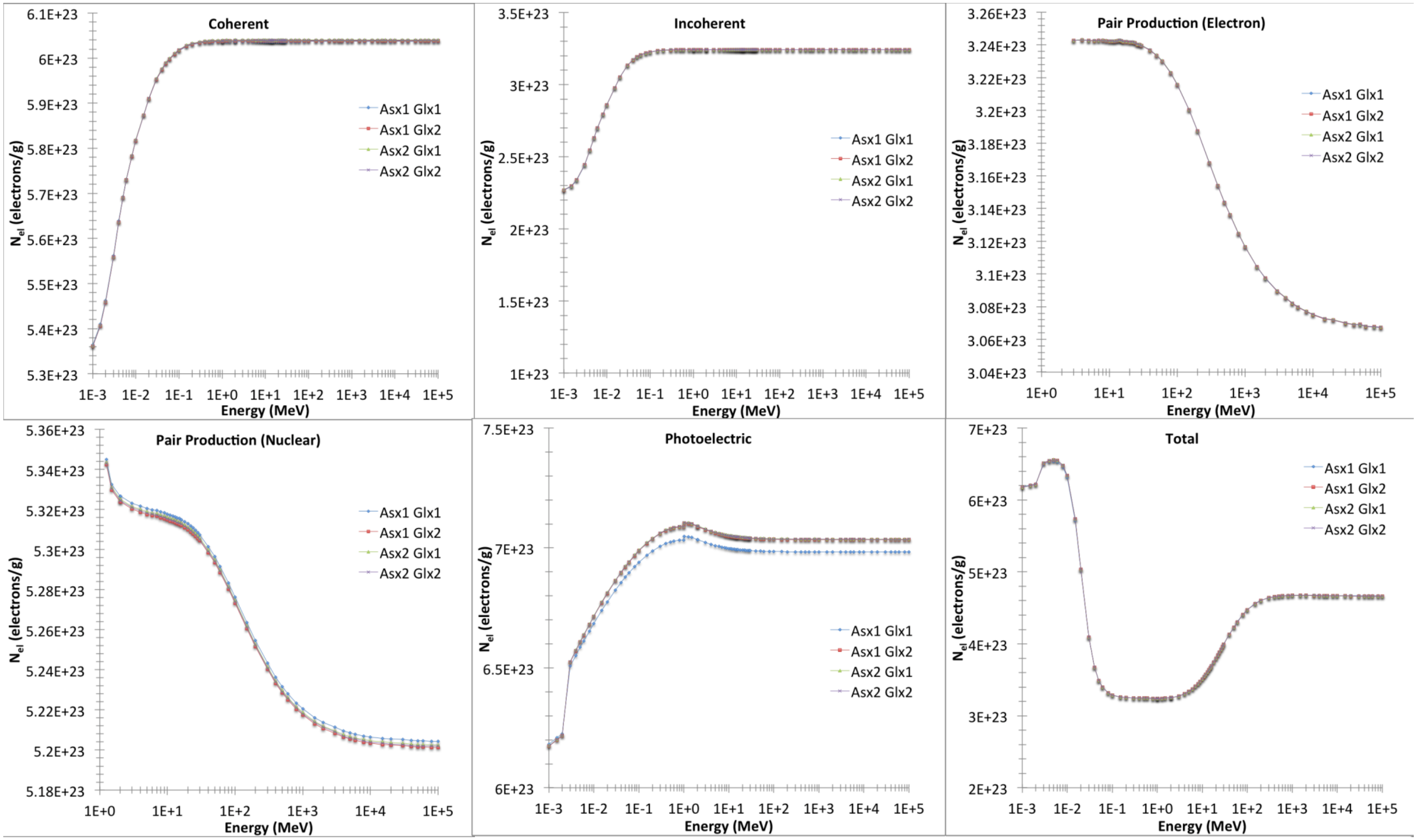

Figure 5. Effective electron density of bacteriorhodopsin for partial and total interactions.

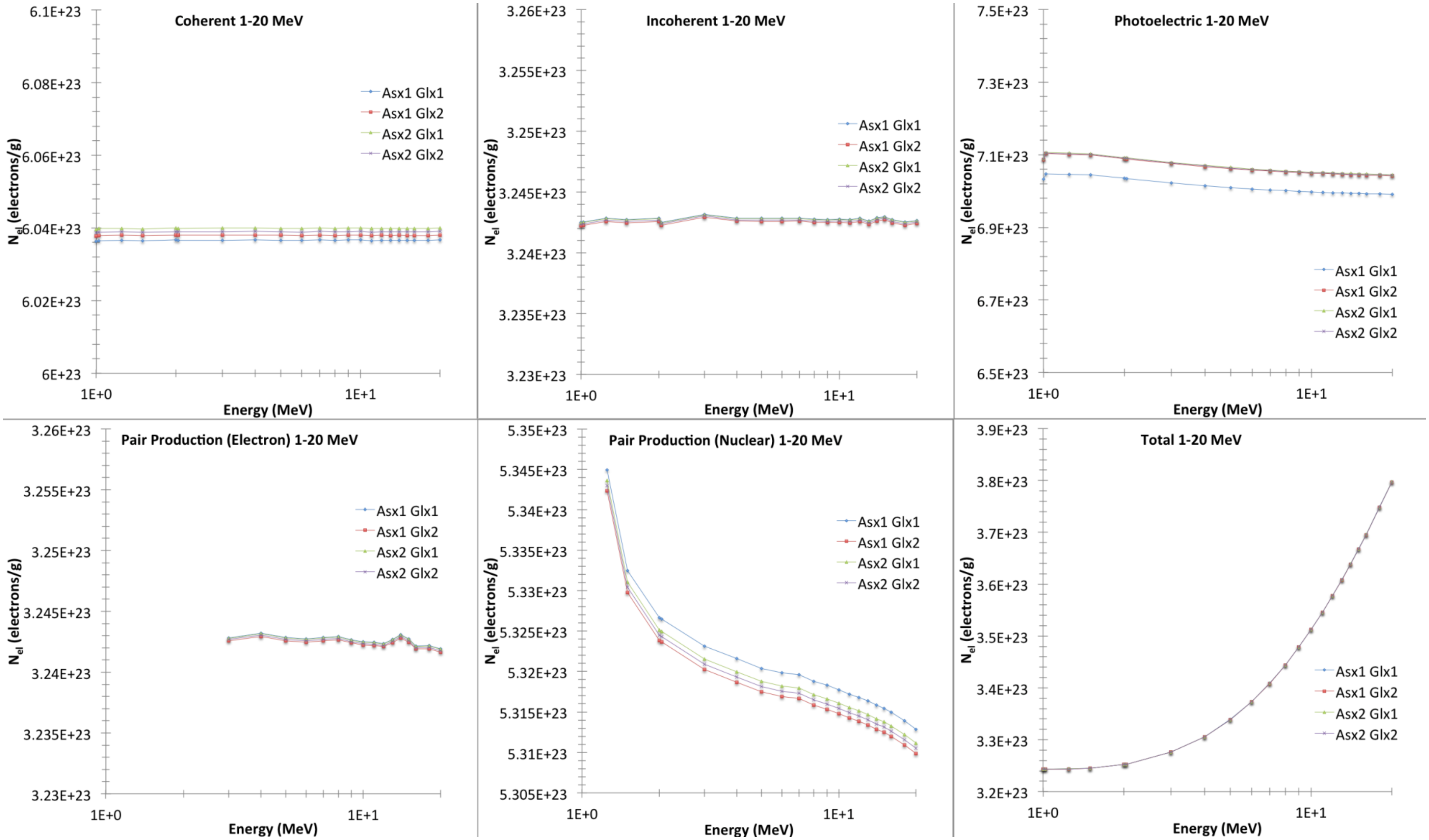

Figure 6. Effective electron density of bacteriorhodopsin for 1-20 MeV photons.

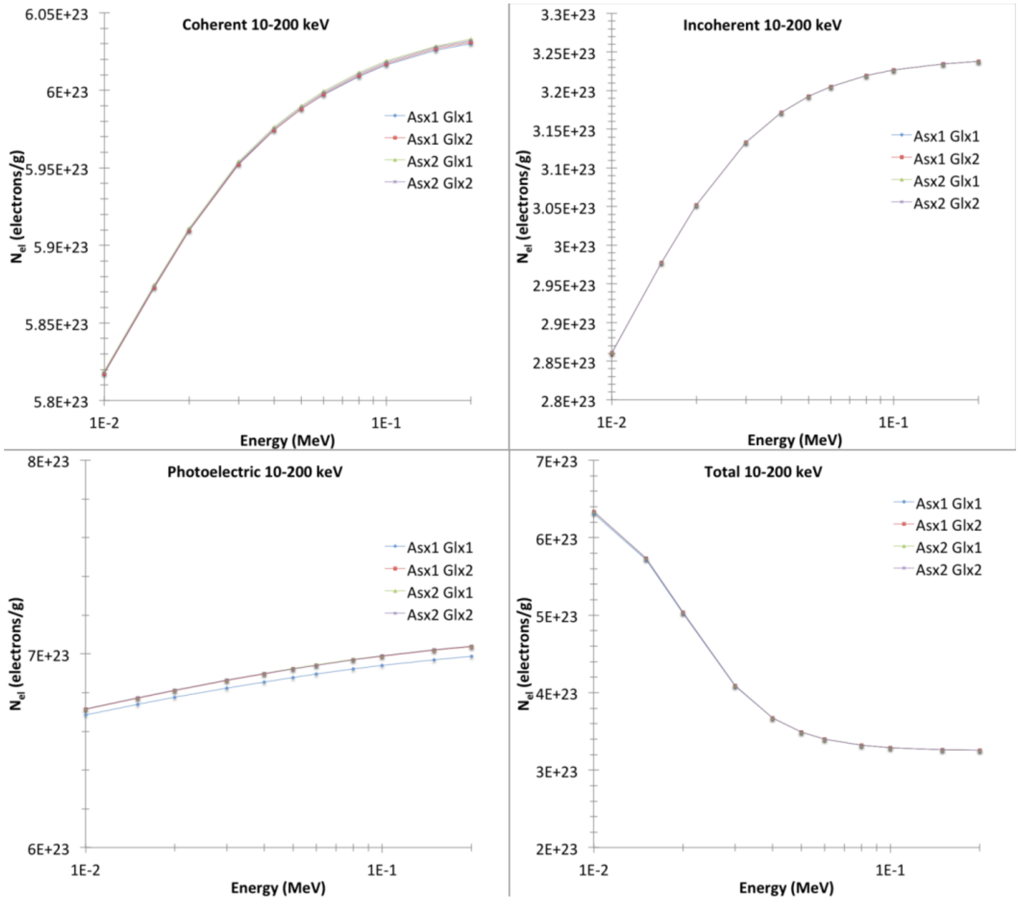

Figure 7. Effective electron density of bacteriorhodopsin for 10-200 keV photons.

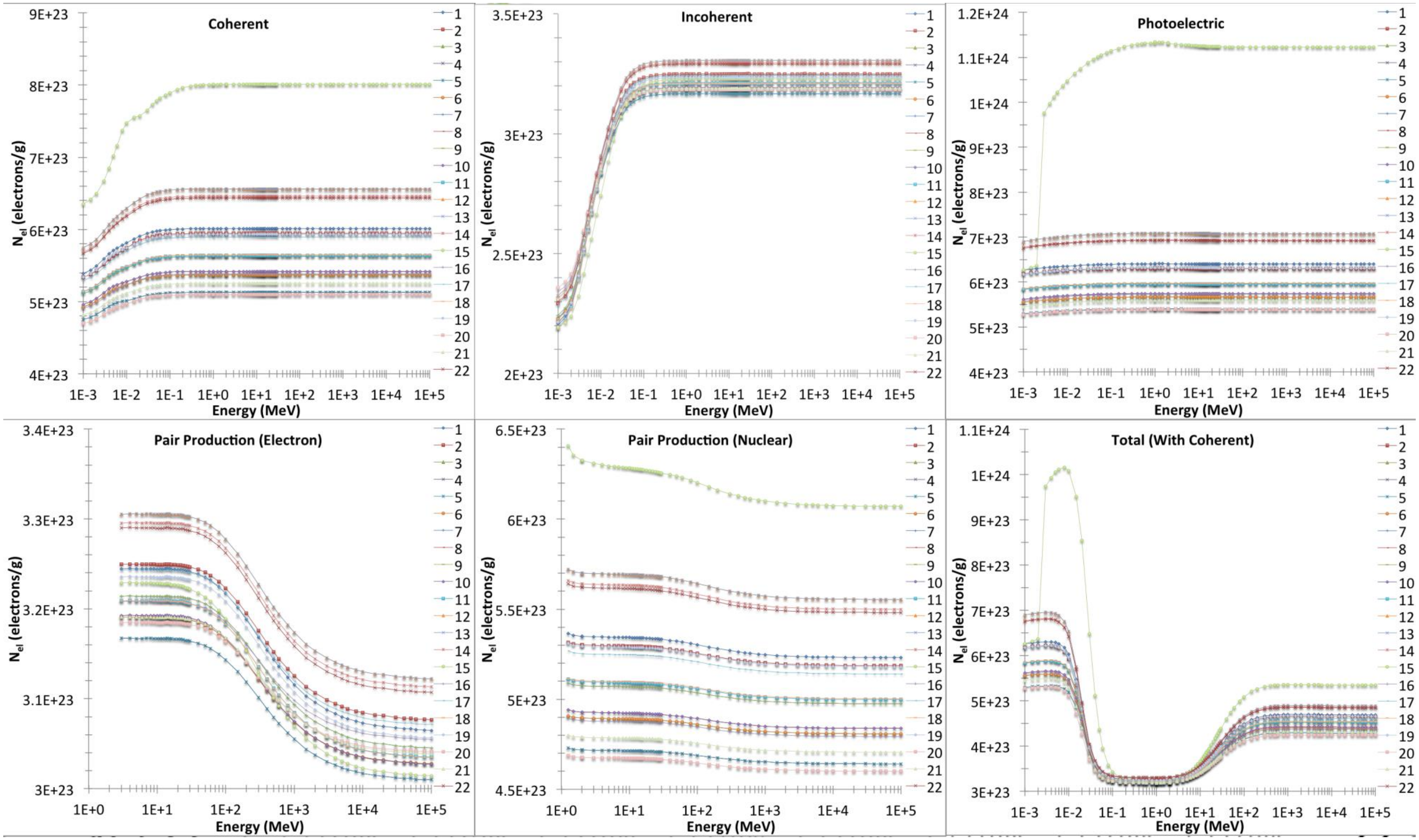

Figure 8. Effective electron density of amino acids of bacteriorhodopsin for partial and total interactions.

Bibliography

[1] F. H. Attix, *Introduction to Radiological Physics and Radiation Dosimetry*. Wiley-VCH, 1991, p. 628.

[2] H. Ebel, “X-ray tube spectra,” *X-Ray Spectrometry*, vol. 28, no. 4, pp. 255 – 266.

[3] F. M. K. PhD, *The Physics of Radiation Therapy*. Lippincott Williams & Wilkins, 2009, p. 531.

[4] L. Stanton, S. D. Brattelli, J. L. Day, R. E. Stanton, and T. Villafana, “Measurements of diagnostic x-ray backscatter by a novel ion chamber method.,” *Medical physics*, vol. 9, no. 1, pp. 121–30.

[5] N. Saito and I. H. Suzuki, “Absolute soft X-ray measurements using an ion chamber,” *Journal of Synchrotron Radiation*, vol. 5, no. 3. International Union of Crystallography, pp. 869–871, 01-May-1998.

[6] C. M. Ma and A. E. Nahum, “Calculations of ion chamber displacement effect corrections for medium-energy x-ray dosimetry.,” *Physics in medicine and biology*, vol. 40, no. 1, pp. 45–62, Jan. 1995.

[7] I. J. Das and S. F. Akber, “Ion recombination and polarity effect of ionization chambers in kilovoltage x-ray exposure measurements.,” *Medical physics*, vol. 25, no. 9, pp. 1751–7, Sep. 1998.

[8] S. N. Ahmed, *Physics and Engineering of Radiation Detection*. Academic Press, 2007, p. 800.

[9] Y. S. Horowitz, *Thermoluminescence & Thermoluminescent Dosimtry*. CRC Press, 1984, p. 200.

[10] B. E. Bjärngard, K. R. Kase, B. I. Rudén, P. J. Biggs, A. L. Boyer, and K. A. Johansson, “Postal intercomparison of absorbed dose for high energy x rays with thermoluminescence dosimeters.,” *Medical physics*, vol. 7, no. 5, pp. 560–5.

[11] L. Duggan, C. Hood, H. Warren-Forward, M. Haque, and T. Kron, “Variations in dose response with x-ray energy of LiF:Mg,Cu,P thermoluminescence dosimeters: implications for clinical dosimetry.,” *Physics in medicine and biology*, vol. 49, no. 17, pp. 3831–45, Sep. 2004.

[12] Z. Cai, X. Pan, D. Hunting, P. Cloutier, R. Lemay, and L. Sanche, “Dosimetry of ultrasoft x-rays (1.5 keV Al K) using radiochromatic films and colour scanners,” *Physics in Medicine and Biology*, vol. 48, no. 24, pp. 4111–4124, Dec. 2003.

[13] S. Devic, “Radiochromic film dosimetry: past, present, and future.,” *Physica medica : PM : an international journal devoted to the applications of physics to medicine and biology : official journal of the Italian Association of Biomedical Physics (AIFB)*, vol. 27, no. 3, pp. 122–34, Jul. 2011.

[14] A. Niroomand-Rad, C. R. Blackwell, B. M. Coursey, K. P. Gall, J. M. Galvin, W. L. McLaughlin, A. S. Meigooni, R. Nath, J. E. Rodgers, and C. G. Soares, "Radiochromic film dosimetry: Recommendations of AAPM Radiation Therapy Committee Task Group 55," *Medical Physics*, vol. 25, no. 11, p. 2093, Nov. 1998.

[15] M. W. Bower and D. E. Hintenlang, "The characterization of a commercial MOSFET dosimeter system for use in diagnostic x ray.," *Health physics*, vol. 75, no. 2, pp. 197–204, Aug. 1998.

[16] C. R. Edwards, S. Green, J. E. Palethorpe, and P. J. Mountford, "The response of a MOSFET, p-type semiconductor and LiF TLD to quasi-monoenergetic x-rays.," *Physics in medicine and biology*, vol. 42, no. 12, pp. 2383–91, Dec. 1997.

[17] C. Ehringfeld, S. Schmid, K. Poljanc, C. Kirisits, H. Aiginger, and D. Georg, "Application of commercial MOSFET detectors for in vivo dosimetry in the therapeutic x-ray range from 80 kV to 250 kV.," *Physics in medicine and biology*, vol. 50, no. 2, pp. 289–303, Jan. 2005.

[18] N. Jornet, P. Carrasco, D. Jurado, A. Ruiz, T. Eudaldo, and M. Ribas, "Comparison study of MOSFET detectors and diodes for entrance in vivo dosimetry in 18 MV x-ray beams.," *Medical physics*, vol. 31, no. 9, pp. 2534–42, Sep. 2004.

[19] G. I. Kaplan, A. B. Rosenfeld, B. J. Allen, J. T. Booth, M. G. Carolan, and A. Holmes-Siedle, "Improved spatial resolution by MOSFET dosimetry of an x-ray microbeam.," *Medical physics*, vol. 27, no. 1, pp. 239–44, Jan. 2000.

[20] J. R. Maldonado, "X-Ray Damage Considerations in MOSFET Devices," *Journal of The Electrochemical Society*, vol. 133, no. 3, p. 628, Mar. 1986.

[21] M. Ahmadi and J. T. W. Yeow, "Fabrication and characterization of a radiation sensor based on bacteriorhodopsin.," *Biosensors & bioelectronics*, vol. 26, no. 5, pp. 2171–6, Jan. 2011.

[22] M. Ahmadi, E. K. Osei, and J. T. W. Yeow, "Bacteriorhodopsin for superficial X-ray sensing," *Sensors and Actuators B: Chemical*, vol. 166–167, no. null, pp. 177–183, May 2012.

[23] M. Ahmadi, N. Lunscher, and J. T. W. Yeow, "Effective atomic numbers and electron densities of bacteriorhodopsin and its comprising amino acids in the energy range 1keV–100GeV," *Nuclear Instruments and Methods in Physics Research Section B: Beam Interactions with Materials and Atoms*, vol. 300, no. null, pp. 30–34, Apr. 2013.

[24] M. Ahmadi and J. T. W. Yeow, "Theoretical calculation of Radiation Induced Conductivity in nanomaterials," in *2011 11th IEEE International Conference on Nanotechnology*, 2011, pp. 1737–1740.

[25] N. Vsevolodov, *Biomolecular Electronics: An Introduction via Photosensitive Proteins (Bioengineering of Materials)*. Birkhäuser, 2011, p. 296.

[26] D. Oesterhelt and W. Stoeckenius, “Rhodopsin-like Protein from the Purple Membrane of Halobacterium halobium,” *Nature*, vol. 233, no. 39, pp. 149–152, Sep. 1971.

[27] D. Oesterhelt and W. Stoeckenius, “Functions of a new photoreceptor membrane.,” *Proceedings of the National Academy of Sciences of the United States of America*, vol. 70, no. 10, pp. 2853–7, Oct. 1973.

[28] N. Hampp, “Bacteriorhodopsin as a Photochromic Retinal Protein for Optical Memories.,” *Chemical reviews*, vol. 100, no. 5, pp. 1755–1776, May 2000.

[29] U. Haupts, J. Tittor, and D. Oesterhelt, “Closing in on bacteriorhodopsin: progress in understanding the molecule.,” *Annual review of biophysics and biomolecular structure*, vol. 28, pp. 367–99, Jan. 1999.

[30] F. T. Hong, “Interfacial photochemistry of retinal proteins,” *Progress in Surface Science*, vol. 62, no. 1–6, pp. 1–237, Sep. 1999.

[31] A. Danon, M. Brith-Lindner, and S. R. Caplan, “Biogenesis of the purple membrane of Halobacterium halobium.,” *Biophysics of structure and mechanism*, vol. 3, no. 1, pp. 1–17, Apr. 1977.

[32] R. Hartmann, H. D. Sickinger, and D. Oesterhelt, “Anaerobic growth of halobacteria.,” *Proceedings of the National Academy of Sciences of the United States of America*, vol. 77, no. 7, pp. 3821–5, Jul. 1980.

[33] Y. Shen, C. R. Safinya, K. S. Liang, A. F. Ruppert, and K. J. Rothschild, “Stabilization of the membrane protein bacteriorhodopsin to 140 °C in two-dimensional films,” *Nature*, vol. 366, no. 6450, pp. 48–50, Nov. 1993.

[34] J. Cladera, M. L. Galiseo, M. Sabes, P. L. Mateo, and E. Padros, “The role of retinal in the thermal stability of the purple membrane,” *European Journal of Biochemistry*, vol. 207, no. 2, pp. 581–585, Jul. 1992.

[35] K. Douglas, G. Devaud, and N. A. Clark, “Transfer of biologically derived nanometer-scale patterns to smooth substrates.,” *Science (New York, N.Y.)*, vol. 257, no. 5070, pp. 642–4, Jul. 1992.

[36] K. Douglas, N. A. Clark, and K. J. Rothschild, “Biomolecular/solid-state nanoheterostructures,” *Applied Physics Letters*, vol. 56, no. 7, p. 692, Feb. 1990.

[37] J.-A. He, L. Samuelson, L. Li, J. Kumar, and S. K. Tripathy, “Photoelectric Properties of Oriented Bacteriorhodopsin/Polycation Multilayers by Electrostatic Layer-by-Layer Assembly,” *The Journal of Physical Chemistry B*, vol. 102, no. 36, pp. 7067–7072, 1998.

[38] E. J. Calvo, F. Battaglini, C. Danilowicz, A. Wolosiuk, and M. Otero, “Layer-by-layer electrostatic deposition of biomolecules on surfaces for molecular recognition, redox mediation and signal generation.,” *Faraday discussions*, no. 116, pp. 47–65; discussion 67–75, Jan. 2000.

[39] J.-A. He, L. Samuelson, L. Li, J. Kumar, S. K. Tripathy, and B. J. He, “Bacteriorhodopsin Thin-Film Assemblies—Immobilization, Properties, and Applications,” *Advanced Materials*, vol. 11, no. 6, pp. 435–446, Apr. 1999.

[40] K. Edman, P. Nollert, A. Royant, H. Belrhali, E. Pebay-Peyroula, J. Hajdu, R. Neutze, and E. M. Landau, “High-resolution X-ray structure of an early intermediate in the bacteriorhodopsin photocycle.,” *Nature*, vol. 401, no. 6755, pp. 822–6, Oct. 1999.

[41] A. M. Ferreira and D. Bashford, “Model for proton transport coupled to protein conformational change: application to proton pumping in the bacteriorhodopsin photocycle.,” *Journal of the American Chemical Society*, vol. 128, no. 51, pp. 16778–90, Dec. 2006.

[42] I. Ron, I. Pecht, M. Sheves, and D. Cahen, “Proteins as solid-state electronic conductors.,” *Accounts of Chemical Research*, vol. 43, no. 7, pp. 945–953, 2010.

[43] Y. Jin, N. Friedman, M. Sheves, T. He, and D. Cahen, “Bacteriorhodopsin (bR) as an electronic conduction medium: current transport through bR-containing monolayers.,” *Proceedings of the National Academy of Sciences of the United States of America*, vol. 103, no. 23, pp. 8601–6, Jun. 2006.

[44] T. W. Kelley, E. Granstrom, and C. D. Frisbie, “Conducting Probe Atomic Force Microscopy: A Characterization Tool for Molecular Electronics,” *Advanced Materials*, vol. 11, no. 3, pp. 261–264, Mar. 1999.

[45] I. Casuso, L. Fumagalli, J. Samitier, E. Padrós, L. Reggiani, V. Akimov, and G. Gomila, “Electron transport through supported biomembranes at the nanoscale by conductive atomic force microscopy.,” *Nanotechnology*, vol. 18, no. 46, p. 465503, Dec. 2007.

[46] Y. D. Jin, N. Friedman, M. Sheves, and D. Cahen, “Bacteriorhodopsin-Monolayer-Based Planar Metal–Insulator–Metal Junctions via Biomimetic Vesicle Fusion: Preparation, Characterization, and Bio-optoelectronic Characteristics,” *Advanced Functional Materials*, vol. 17, no. 8, pp. 1417–1428, May 2007.

[47] E. Alfinito and L. Reggiani, “Charge transport in bacteriorhodopsin monolayers: The contribution of conformational change to current-voltage characteristics,” *EPL (Europhysics Letters)*, vol. 85, no. 6, p. 68002, Mar. 2009.

[48] R. R. Birge, “Protein-based optical computing and memories,” *Computer*, vol. 25, no. 11, pp. 56–67, Nov. 1992.

[49] V. Thavasi, T. Lazarova, S. Filipek, M. Kolinski, E. Querol, A. Kumar, S. Ramakrishna, E. Padrós, and V. Renugopalakrishnan, “Study on the feasibility of bacteriorhodopsin as bio-photosensitizer in excitonic solar cell: a first report.,” *Journal of nanoscience and nanotechnology*, vol. 9, no. 3, pp. 1679–87, Mar. 2009.

[50] S. R. Caplan, G. Fischer, and S. Roy, “Photovoltaic behavior of bacteriorhodopsin-loaded cation-exchange membranes,” *Journal of Membrane Science*, vol. 16, no. null, pp. 391–405, Jan. 1983.

[51] T. Miyasaka, K. Koyama, and I. Itoh, “Quantum conversion and image detection by a bacteriorhodopsin-based artificial photoreceptor.,” *Science (New York, N.Y.)*, vol. 255, no. 5042, pp. 342–4, Jan. 1992.

[52] C. Guillén and J. Herrero, “Comparison study of ITO thin films deposited by sputtering at room temperature onto polymer and glass substrates,” *Thin Solid Films*, vol. 480–481, no. null, pp. 129–132, Jun. 2005.

[53] V. Manjunathaguru and T. K. Umesh, “Effective atomic numbers and electron densities of some biologically important compounds containing H, C, N and O in the energy range 145–1330 keV,” *Journal of Physics B: Atomic, Molecular and Optical Physics*, vol. 39, no. 18, pp. 3969–3981, Sep. 2006.

[54] V. Manjunathaguru and T. K. Umesh, “Total interaction cross sections and effective atomic numbers of some biologically important compounds containing H, C, N and O in the energy range 6.4–136 keV,” *Journal of Physics B: Atomic, Molecular and Optical Physics*, vol. 40, no. 18, pp. 3707–3718, Sep. 2007.

[55] S. Prasanna Kumar, V. Manjunathaguru, and T. K. Umesh, “Effective atomic numbers of some H-, C-, N- and O-based composite materials derived from differential incoherent scattering cross-sections,” *Pramana*, vol. 74, no. 4, pp. 555–562, Apr. 2010.

[56] S. R. Manohara, S. M. Hanagodimath, K. S. Thind, and L. Gerward, “On the effective atomic number and electron density: A comprehensive set of formulas for all types of materials and energies above 1keV,” *Nuclear Instruments and Methods in Physics Research Section B: Beam Interactions with Materials and Atoms*, vol. 266, no. 18, pp. 3906–3912, Sep. 2008.

[57] S. R. Manohara, S. M. Hanagodimath, and L. Gerward, “The effective atomic numbers of some biomolecules calculated by two methods: a comparative study.,” *Medical physics*, vol. 36, no. 1, pp. 137–41, Jan. 2009.

[58] S. R. Manohara and S. M. Hanagodimath, “Effective atomic numbers for photon energy absorption of essential amino acids in the energy range 1keV to 20MeV,” *Nuclear Instruments and Methods in Physics Research Section B: Beam Interactions with Materials and Atoms*, vol. 264, no. 1, pp. 9–14, Nov. 2007.

[59] L. Gerward, N. Guilbert, K. Bjørn Jensen, and H. Levring, “X-ray absorption in matter. Reengineering XCOM,” *Radiation Physics and Chemistry*, vol. 60, no. 1–2, pp. 23–24, Jan. 2001.

[60] L. Gerward, N. Guilbert, K. B. Jensen, and H. Levring, “WinXCom—a program for calculating X-ray attenuation coefficients,” *Radiation Physics and Chemistry*, vol. 71, no. 3–4, pp. 653–654, Oct. 2004.

[61] S. Gowda, S. Krishnaveni, and R. Gowda, “Studies on effective atomic numbers and electron densities in amino acids and sugars in the energy range 30–1333keV,” *Nuclear Instruments and Methods in Physics Research Section B: Beam Interactions with Materials and Atoms*, vol. 239, no. 4, pp. 361–369, Oct. 2005.

[62] H. G. Khorana, G. E. Gerber, W. C. Herlihy, C. P. Gray, R. J. Anderegg, K. Nihei, and K. Biemann, “Amino acid sequence of bacteriorhodopsin.,” *Proceedings of the National Academy of Sciences*, vol. 76, no. 10, pp. 5046–5050, Oct. 1979.

[63] M. L. Taylor, R. L. Smith, F. Dossing, and R. D. Franich, “Robust calculation of effective atomic numbers: the Auto-Z(eff) software.,” *Medical physics*, vol. 39, no. 4, pp. 1769–78, Apr. 2012.

[64] J. F. Fowler, “Radiation-induced Conductivity in the Solid State, and Some Applications,” *Physics in Medicine and Biology*, vol. 3, no. 4, pp. 395–410, Apr. 1959.

[65] L. Weaver, J. K. Shultis, and R. E. Faw, “Analytic solutions of a model for radiation-induced conductivity in insulators,” *Journal of Applied Physics*, vol. 48, no. 7, p. 2762, Jul. 1977.

[66] D. Porschke, “Electrostatics and electrodynamics of bacteriorhodopsin.,” *Biophysical journal*, vol. 71, no. 6, pp. 3381–91, Dec. 1996.

[67] D. Porschke, “Macrodipoles Unusual electric properties of biological macromolecules,” *Biophysical Chemistry*, vol. 66, no. 2–3, pp. 241–257, Jun. 1997.

[68] Y. Kimura, M. Fujiwara, and A. Ikegami, “Anisotropic electric properties of purple membrane and their change during the photoreaction cycle.,” *Biophysical journal*, vol. 45, no. 3, pp. 615–25, Mar. 1984.

[69] W. W. Wang, “Time and frequency response characteristics of bacteriorhodopsin-based photodetectors,” *Optical Engineering*, vol. 45, no. 8, p. 084001, Aug. 2006.

[70] W. W. Wang, G. K. Knopf, and A. S. Bassi, “Photoelectric properties of a detector based on dried bacteriorhodopsin film.,” *Biosensors & bioelectronics*, vol. 21, no. 7, pp. 1309–19, Jan. 2006.

[71] A. Iwasaki, “10MV X-ray central-axis dose calculation in thorax-like phantoms (water/cork) using the differential primary and scatter method,” *Radiation Physics and Chemistry*, vol. 65, no. 1, pp. 11–26, Aug. 2002.

[72] I. Bakarudin and M. A. Slifkin, “A study of light-induced conductivity in bacteriorhodopsin,” *Journal of Biological Physics*, vol. 18, no. 3, pp. 203–216, 1991.

[73] M. A. Slifkin, H. Garty, W. V Sherman, M. F. Vincent, and S. R. Caplan, “Light-induced conductivity changes in purple membrane suspensions.,” *Biophysics of structure and mechanism*, vol. 5, no. 4, pp. 313–20, Aug. 1979.

[74] B. Gähwiler, I. Zschokke-Gränacher, E. Baldinger, and H. Lüthy, “Conductivity induced by x-rays in DNA films.,” *Physics in medicine and biology*, vol. 15, no. 4, pp. 701–4, Oct. 1970.

[75] W. U. Laub, T. W. Kaulich, and F. Nüsslin, “Energy and dose rate dependence of a diamond detector in the dosimetry of 4-25 MV photon beams.,” *Medical physics*, vol. 24, no. 4, pp. 535–6, Apr. 1997.

[76] P. W. Hoban, M. Heydarian, W. A. Beckham, and A. H. Beddoe, “Dose rate dependence of a PTW diamond detector in the dosimetry of a 6 MV photon beam.,” *Physics in medicine and biology*, vol. 39, no. 8, pp. 1219–29, Aug. 1994.

[77] J. Ma, J. T. W. Yeow, J. C. L. Chow, and R. B. Barnett, “A carbon fiber-based radiation sensor for dosimetric measurement in radiotherapy,” *Carbon*, vol. 46, no. 14, pp. 1869–1873, Nov. 2008.

[78] M. Engelhard, B. Hess, M. Chance, and B. Chance, “X-ray absorption studies on bacteriorhodopsin,” *FEBS Letters*, vol. 222, no. 2, pp. 275–278, Oct. 1987.

[79] F. Sepulcre, A. Cordomí, M. G. Proietti, J. J. Perez, J. García, E. Querol, and E. Padrós, “X-ray absorption and molecular dynamics study of cation binding sites in the purple membrane.,” *Proteins*, vol. 67, no. 2, pp. 360–74, May 2007.

[80] P. A. Evans, A. J. Moloney, and P. J. Mountford, “Performance assessment of the Gulmay D3300 kilovoltage X-ray therapy unit.,” *The British journal of radiology*, vol. 74, no. 882, pp. 537–47, Jun. 2001.

[81] S. A. H. Scottish Executive, “Report into unintended overexposure of Lisa Norris at Beatson, Glasgow.” Scottish Executive, Edinburgh, 27-Oct-2006.

[82] S. R. Manohara and S. M. Hanagodimath, “Studies on effective atomic numbers and electron densities of essential amino acids in the energy range 1keV–100GeV,” *Nuclear Instruments and Methods in Physics Research Section B: Beam Interactions with Materials and Atoms*, vol. 258, no. 2, pp. 321–328, May 2007.

[83] B. D. Milbrath, A. J. Peurrung, M. Bliss, and W. J. Weber, “Radiation detector materials: An overview,” *Journal of Materials Research*, vol. 23, no. 10, pp. 2561–2581, Jan. 2011.

[84] Oliveira,I.B, “Purification and growth of PbI 2 crystals: dependence of the radiation response on the PbI 2 crystal purity,” *Nuclear Science, IEEE Transactions on*, vol. 49, no. 4, pp. 1968 – 1973.

[85] Onodera,T, “Spectroscopic Performance of Pixellated Thallium Bromide Detectors,” *Nuclear Science, IEEE Transactions on*, vol. 52, no. 5, pp. 1999 – 2002.

[86] Meng,L.J, “Spectroscopic Performance of Thick HgI$_2$Detectors,” *Nuclear Science, IEEE Transactions on*, vol. 53, no. 3, pp. 1706 – 1712.

[87] Matsumoto,M, “Bismuth tri-iodide crystal for nuclear radiation detectors,” *Nuclear Science, IEEE Transactions on*, vol. 49, no. 5, pp. 2517 – 2520.

[88] Nason,D, “The growth and crystallography of bismuth tri-iodide crystals grown by vapor transport,” *Journal of Crystal Growth*, vol. 156, no. 3, pp. 221 – 226.

[89] Rincon M.E., Sanchez M., George P.J., Sanchez A., and Nair P.K., “Comparison of the Properties of Bismuth Sulfide Thin Films Prepared by Thermal Evaporation and Chemical Bath Deposition,” *Journal of Solid State Chemistry*, vol. 136, no. 2, p. 8, 1998.

[90] D. Becerra, M. T. S. Nair, and P. K. Nair, “Analysis of a Bismuth Sulfide/Silicon Junction for Building Thin Film Solar Cells,” *Journal of The Electrochemical Society*, vol. 158, no. 7, p. H741, Jul. 2011.

[91] L. M. Peter, K. G. U. Wijayantha, D. J. Riley, and J. P. Waggett, “Band-edge tuning in self-assembled layers of Bi2S3 nanoparticles used to photosensitize nanocrystalline TiO2,” *Journal of Physical Chemistry B*, vol. 107, no. 33, pp. 8378–8381, 2010.

[92] K. A. Z. S. Abuthahir and R. Jagannathan, “Reverse-loop impedance profile in Bi2S3 quantum dots,” *Materials Chemistry and Physics*, vol. 121, no. 1–2, pp. 184–192, May 2010.

[93] R. Chen, M. H. So, C.-M. Che, and H. Sun, “Controlled synthesis of high crystalline bismuth sulfide nanorods: using bismuth citrate as a precursor,” *Journal of Materials Chemistry*, vol. 15, no. 42, p. 4540, Oct. 2005.

[94] S.-H. Yu, J. Yang, Y.-S. Wu, Z.-H. Han, Y. Xie, and Y.-T. Qian, “Hydrothermal preparation and characterization of rod-like ultrafine powders of bismuth sulfide,” *Materials Research Bulletin*, vol. 33, no. 11, pp. 1661–1666, Nov. 1998.

[95] Q. Li, M. Shao, J. Wu, G. Yu, and Y. Qian, “Synthesis of nano-fibrillar bismuth sulfide by a surfactant-assisted approach,” *Inorganic Chemistry Communications*, vol. 5, no. 11, pp. 933–936, Oct. 2002.

[96] M. Black, Y.-M. Lin, S. Cronin, O. Rabin, and M. Dresselhaus, “Infrared absorption in bismuth nanowires resulting from quantum confinement,” *Physical Review B*, vol. 65, no. 19, p. 195417, May 2002.

[97] O. Rabin, J. Manuel Perez, J. Grimm, G. Wojtkiewicz, and R. Weissleder, “An X-ray computed tomography imaging agent based on long-circulating bismuth sulphide nanoparticles.,” *Nature materials*, vol. 5, no. 2, pp. 118–22, Feb. 2006.

[98] M. T. S. Nair and P. K. Nair, “Photoconductive bismuth sulphide thin films by chemical deposition,” *Semiconductor Science and Technology*, vol. 5, no. 12, pp. 1225–1230, Dec. 1990.

[99] M. G. Kanatzidis, T. J. McCarthy, T. A. Tanzer, L.-H. Chen, T. Hogan, C. R. Kannewurf, and L. Iordanidis, “Ternary Bismuth Chalcogenides for Thermoelectric Applications. Synthesis and Charge Transport Properties of New Compounds in the K-BI-S System.,” *MRS Proceedings*, vol. 410, p. 37, Feb. 2011.

[100] B. Chen and C. Uher, “Transport Properties of Bi2S3 and the Ternary Bismuth Sulfides KBi6.33S10 and K2Bi8S13,” vol. 4756, no. 5, pp. 1655–1658, 1997.

[101] J. R. Dennison, J. Gillespie, J. Hodges, R. C. Hoffmann, J. Abbott, S. Hart, A. W. Hunt, F. D. McDaniel, and B. L. Doyle, “Temperature Dependence of Radiation Induced Conductivity in Insulators,” in *AIP Conference Proceedings*, 2009, vol. 1099, no. 1, pp. 203–208.

[102] Q. Kang, J. T. W. Yeow, and R. Barnett, “The use of semiconducting single-walled carbon nanotube films to measure X-ray dose,” *Carbon*, vol. 50, no. 6, pp. 2197–2201, May 2012.

[103] A. M. Smith and S. Nie, “Semiconductor nanocrystals: structure, properties, and band gap engineering.,” *Accounts of chemical research*, vol. 43, no. 2, pp. 190–200, Feb. 2010.

[104] G. Cao, *Nanostructures & Nanomaterials: Synthesis, Properties & Applications*. Imperial College Press, 2004, p. 433.

[105] C. G. Clayton, B. C. Haywood, and J. F. J. Fowler, “Conductivity induced by Radiation in Polycrystalline Cadmium Sulphide and Polyethylene,” *Nature*, vol. 183, no. 4668, pp. 1112–1113, Apr. 1959.

[106] D. Ph, F. P. Inst, and J. F. Fowler, “Radiation-induced Conductivity in the Solid State, and Some Applications,” *Physics in Medicine and Biology*, vol. 3, no. 4, pp. 395–410, Apr. 1959.

[107] A. Rose, “Space-Charge-Limited Currents in Solids,” *Physical Review*, vol. 97, no. 6, pp. 1538–1544, Mar. 1955.

[108] A. Rose, “Recombination Processes in Insulators and Semiconductors,” *Physical Review*, vol. 97, no. 2, pp. 322–333, Jan. 1955.

[109] N. S. Pesika, Z. Hu, K. J. Stebe, and P. C. Searson, “Quenching of Growth of ZnO Nanoparticles by Adsorption of Octanethiol,” *The Journal of Physical Chemistry B*, vol. 106, no. 28, pp. 6985–6990, 2002.

[110] D. J. Riley, J. P. Waggett, and K. G. U. Wijayantha, “Colloidal bismuth sulfide nanoparticles: a photoelectrochemical study of the relationship between bandgap and particle size,” *Journal of Materials Chemistry*, vol. 14, no. 4, pp. 704–708, 2004.

[111] C.-J. Park, Y.-H. Kim, and K. Chang, “Band-gap modification by radial deformation in carbon nanotubes,” *Physical Review B*, vol. 60, no. 15, pp. 10656–10659, 1999.

[112] Z. L. Wang, “Zinc oxide nanostructures: growth, properties and applications,” *Journal of Physics: Condensed Matter*, vol. 16, no. 25, pp. R829–R858, Jun. 2004.

[113] S. Narita, Y. Nishibori, H. Naito, H. Ito, H. Endo, T. Chiba, Y. Sakemi, M. Itoh, and H. Yoshida, “Development of radiation sensor based on Pt/ZnO Schottky diode,” in *2011 IEEE Nuclear Science Symposium Conference Record*, 2011, pp. 1726–1729.

[114] K. Arshak, O. Korostynska, E. Jafer, A. Arshak, D. Morris, and E. Gill, “Gamma Radiation Sensing Using ZnO and SnO2 Thick Film Interdigitated Capacitors,” in *2006 29th International Spring Seminar on Electronics Technology*, 2006, pp. 483–488.